Analysis of fluid motion in cryogenic propulsion upper stage tanks during launcher ascent phase

MSc Thesis

Ioannis Tsavlidis

Analysis of fluid motion in cryogenic propulsion upper stage tanks during launcher ascent phase

MSc Thesis

by

Ioannis Tsavlidis

to obtain the degree of

Master of Science
in Aerospace Engineering

at the Delft University of Technology,
to be defended publicly on Tuesday March 20, 2018 at 14:00 PM.

Student number:	4519647	
Thesis Committee:	Prof. dr. Stefan Hickel,	TU Delft supervisor
	Dr. A. Gangoli Rao,	TU Delft
	ir. Barry T.C. Zandbergen,	TU Delft
	MSc. Oliver Feindt,	ArianeGroup supervisor

TU Delft

Acknowledgments

It is now time to write these final words which mark the end of an era; the end of my course as a student and the commencement of a new exciting chapter in my life. The last two and a half years were undoubtedly exciting, full of new challenges, including limitless stressful, yet beneficial moments. Following a full study course, with academic courses in the Netherlands, an internship experience in Greece, and an MSc thesis project in Germany, has already equipped me with a set of new technical and most importantly personal skills like patience, adaptability and confidence.

I feel indebted to thank Alexander S. Onassis Public Benefit Foundation for granting me a scholarship for my studies. Without its support, it would have been impossible for me to achieve what I have up to now achieved. It is encouraging to see such initiatives which promote science, and which the Foundation supports for more that 4 decades after Aristotle Onassis' will.

I would also like to thank Prof. dr. Stefan Hickel, Chair of Aerodynamics, who has been my supervisor at TU Delft, and who provided me with important feedback and support throughout my project. The same gratitude I owe to MSc Oliver Feindt who was my daily supervisor at ArianeGroup. If it was not for his support I would not have been able to tackle the challenges of the project. Thanks to his advice, we managed to extract the best possible outcome out of this effort. It was an honor working with him. My sincere thanks to Dr. A.G. Rao and ir. B.T.C. Zandbergen for assessing my work and being part of the graduation committee.

To continue, I would love to thank Dr. Tim Arndt for his vital technical advice during the project, and for his valuable tips regarding the next steps of my engineering career. Dr. Arndt as well as Oliver, Arnold, Nicole, Valentin, Giuseppe, Daniel, Antoine, Fibian, Niklas and all the colleagues, welcomed me in the department, in the best possible way. Special thanks should be attributed to Valentin Wegner, who shared his office with me, for all the help, valuable discussions and the future plans we made. Last but not least, I would like to thank Dr. Martin Konopka and Mr. Dennis Haake of the CFD department, who provided me with all the necessary data for my thesis and they were always willing to help me overcome any obstacles.

I need to express my thankfulness to fellow student Juan Regueiro Cueva who was one of the first people I met in the faculty and with whom I partnered in most of our academic group projects. Alongside that, I would also like to thank my fellow students Cristina, Sagarika, Hugo, Bruno, Jonathan, Kaushik, Jaydeep and Dionisis for all the great times we had together and their support in several assignments and courses. I wish all the best for all of them.

My sincere friend Michalis Poikilidis thank you for your support throughout our studies. It was a pleasure meeting you in Schiedam, The Netherlands.

Heartfelt thanks and gratitude to my life partner and companion, Maria, who made everything seem easier with her presence in my life.

All of my friends and family back in Greece hold a vital role in this accomplishment. My parents, Evanggelia and Stylianos, despite not being here with me, will hopefully be more than proud of my effort.

Ioannis Tsavlidis
Bremen, February 2018

Abstract

The graduation project was conducted at the upper stage liquid propulsion department of ArianeGroup at the facilities of Airbus DS, Bremen. Based on a series of past flights of Ariane 5 launcher, the aim is to analyze the fluid motion and the pressure fluctuations in the cryogenic propulsion upper stage Liquid Hydrogen (LH_2) and Liquid Oxygen (LO_x) tanks during the ascent phase. Pressure fluctuations (drops or rises) during the ascent phase are undesirable due to the need for relief or re-pressurization of the fuel tanks. Tank relief is obtained through relief valves, while re-pressurization is done using on-board gaseous Helium; both cases increase the failure probability of the system and/or the total weight of the launcher. The objective of the project is to find out why these pressure fluctuations occur, what are the parameters that affect the pressure evolution and at what extend the liquid fuel motion (sloshing) is responsible for this behavior. According to the literature several parameters affect the pressure evolution during sloshing. These parameters are further investigated through flight data analysis. The approach also involves CFD simulations of the kinematic behavior of the liquid fuel focusing on the sloshing angle. Finally, a statistical model is built attempting to predict the pressure change inside the tanks. Higher sloshing angles match with higher pressure rise inside the LO_x tank. The magnitude of the pressure rise appears to be directly connected to the kinematic profile of the launcher as well as to the ullage volume of the tank. The maximum predicted ullage pressure is below the tank's sizing pressure limit. Regarding the LH_2 tank, no strong correlation of flight parameters to the pressure change is identified; no sufficient statistical model is built. The CFD simulation shows that relatively higher sloshing angle magnitude and duration exists near the pressure drop periods and that strong breaking waves are likely to be formed in the case of a sudden pressure drop behavior. The LH_2 tank is more prone to the formation of breaking/splashing waves. The effect of vibrations, which is not included in the CFD study, is also important for the explanation of the pressure drop magnitude.

Contents

Nomenclature

Latin Symbols

$\hat{y}_{p,upper}$	Prediction upper limit	% or bar
$\hat{y}_p$	Predicted value	% or bar
$Accel_{-x-y-z-yz}$	The total acceleration components magnitude change during the rise/drop	m/s^2
Bo	Bond number	
C_{GHe}	Helium concentration estimate	
CFD	Computational Fluid Dynamics	
CoG	Center of Gravity	
d_1	Time period before the pressure rise in the LO_x tank	s
d_2	Time period before the pressure drop in the LH_2 tank	s
d_3	Time period before the pressure stabilization in both tanks	s
EAP	Solid rocket boosters. French: Etage d'Accélération à Poudre	
EPC	Main cryogenic stage. French: Etage Principal Cryotechnique	
ESC	Cryogenic upper stage. French: Etage Supérior Cryotechnique	
F	Liquid fraction function	
$F001, 002, ..., 061$	Flight numbering	
f_n	Natural frequency	Hz
f_o	Excitation frequency	Hz
g, g_{grav}	Acceleration of gravity	m/s^2
g_{par}	Acceleration of a fluid particle	m/s^2
GH_2	Gaseous hydrogen	
GHe	Gaseous helium	
GN_2	Gaseous nitrogen	
GO_x	Gaseous oxygen	
h	Tank fill height	m
H_0	Launch initiation time	
H_1	Solid rocket boosters flame out time	
H_2	Main cryogenic stage engine shutdown time	
H_3	Cryogenic upper stage shutdown time	

h_A	Fluid height at tank's center	m
h_C	Fluid height at the probe location	m
$k-\epsilon$	k-epsilon two equation turbulence model	
L	Characteristic length	m
LH_2	Liquid hydrogen	
LN_2	Liquid nitrogen	
LO_x	Liquid oxygen	
MAE	Mean Absolute Error	
MLR	Multiple Linear Regression	
MS	Mean Squares	
P	Pressure	bar
P_{init}	Initial pressure at ground pressurization phase	bar
p_{init}	The initial ullage pressure at H_o	bar
P_{max}	Maximum target pressure at ground pressurization phase	bar
P_{sat}	Saturation pressure	bar
PSD	Power Spectral Density	
R	Correlation coefficient	
R	Tank radius	m or in
RAE	Relative Absolute Error	
$RMSE$	Root Mean Square Error	
$Roll_{-x-y-z}$	The total roll rates components magnitude change during the rise/drop	rad/s
$RRSE$	Root Relative Squared Error	
RSS	Sum of Squared Residuals	
SS	Sum Squares	
T	Temperature	K
t_{drop}	Pressure drop time	s
T_{init}	The initial ullage temperature	K
t_l	Lift-off time	s
T_{max}	The maximum ullage temperature	K
$t_{p_{max}}$	The time after launch at which the pressure drop occurs - LH_2 tank	s
$t_{p_{min}}$	The time after launch at which the pressure rise occurs - LO_x tank	s
$t_{press,tot}$	Total pressurization time	l
t_{press}	Pressurization start time	s
$t_{recover}$	Pressure recovery time	s

t_{rise}	Pressure rise time	s
T_{sat}	Saturation temperature	K
U_{Ullage}	Ullage volume	l
X	Design table of MLR	
X_0	Maximum excitation magnitude of oscillation	in
x_a	Maximum excitation magnitude of oscillation	m
x_i	Predictors. i=1..n	
x_p	Predictor matrix	

Greek Symbols

β_i	-Parameters determined by Miles for the phase diagram of dimensionless forcing amplitude vs frequency of cylindrical tanks -Multiple linear regression coefficients	
Δp	Pressure change magnitude	% or bar
ΔT_{drop}	The total ullage temperature drop recorded during flight	K
λ	Empirical constant for the calculation of f_n	
μ	Dynamic viscosity	kg/ms
ν	Kinematic viscosity	m^2/s
ϕ	Sloshing angle	deg
ρ	Density	kg/m^3
σ	Surface tension	N/m
σ^2	Error mean square	
a_A	Amplitude of vibrations	m/s^2
K_1,K_2	Empirical parameters determined by Stofan for the phase diagram of dimensionless forcing amplitude vs frequency of spherical tanks	

List of Figures

List of Tables

"We are what we repeatedly do. Excellence, then, is not an act, but a habit."

-Aristotle, Philosopher, 384–322 BC

1 Introduction

In the present chapter a description of the project context is made. The reader is introduced to the aspects of launcher operation, focusing on the upper stage compartment and the fuel tanks, the launch phases and the physical phenomena that take place inside the tanks and are of major importance for the present study.

1.1. Project context

There have been almost 3 decades (22^{nd} of January 1990) since the first flight of Ariane 4, an Ariane family launcher which served the aerospace industry until 2003. By today, its successor, Ariane 5 has managed to complete 82 consecutive successful flights, the latest one being VA240 on the 12^{th} of December 2017 [Arianespace, 2017] . The Ariane family will continue with its new member, Ariane 6, which is planned to have its first launch in 2020 [ESA, 2017].

The graduation project was held at the upper stage liquid propulsion department of ArianeGroup at the facilities of Airbus DS, Bremen. During past flights of Ariane 5, a fluctuating pressure behavior has been noted in the upper stage cryogenic tanks. To be more specific, the pressure inside the cryogenic propulsion upper stage Liquid Hydrogen (LH_2) and Liquid Oxygen (LO_x) tanks, does not remain constant during the ascent phase. Contrariwise, it has been observed that sudden rises or drops are taking place. Such behavior is undesirable as tank re-pressurization or relief is required in order the pressure not to exceed the minimum and the maximum structural limits. Tank relief is obtained through relief valves, while re-pressurization is done using on-board Helium; both cases increase the failure probability of the system and/or the total weight of the launcher.

Based on a series of past flights of Ariane 5 launcher, the aim is to analyze the fluid motion and the pressure fluctuations in the cryogenic propulsion upper stage tanks during the ascent phase. The objective of the project is to find out why these pressure fluctuations occur, what are the parameters that affect the pressure evolution and at what extent the liquid fuel motion (sloshing) is responsible for this behavior. This will be done by way of analyzing flight data and by performing CFD simulations of the LO_x and LH_2 tanks. The area of interest includes the ground pressurization phase and extends up to approximately $200\,s$ after launch. Managing to develop an understanding of the pressure behavior will pave the way for a better explanation on why such phenomena occur and will provide insight to future designs on how to avoid this challenging behavior. Furthermore, with the knowledge gained during this project it will be attempted to predict the magnitude of pressure fluctuations through a statistical approach.

1.2. Background on launchers

Launchers' main purpose is to launch and safely guide to a final orbit the payload that is being carried at the upper part inside the fairing. To gain a better understanding on launcher operation, a brief explanation of its components and mission phases is attempted, as shown in Figures 1.2.1 and 1.2.2.

The cryogenic main core stage (French: Etage Principal Cryotechnique - EPC) has a diameter of $5.4\,m$ and a total height of $23.8\,m$ (without the engine). Its total dry mass is $14.7\,t$ while inside its aluminum alloy tanks it carries approximately $170\,t$ of liquid hydrogen and liquid oxygen. Its engine can generate thrust up to $960\,kN$ at sea level and $1390\,kN$ in vacuum. The EPC is not the main thrust generator of the launcher as the produced thrust accounts only for 10% of the total one. The EPC is ignited at $H_0 + 1\,s$ and its total combustion time is $540\,s$.

The solid rocket boosters compartment (French: Etage d'Accélération à Poudre - EAP) consists of two boosters with a diameter of $3.05\,m$ and a total height of $31.6\,m$. Each booster carries $240\,t$ of solid propellant and if combined can generate $7000\,kN$ of thrust in vacuum. The solid propellant is a mix of aluminum (fuel), ammonium perchlorate (oxidizer) and polybutadiene (binder). The EAP ignites approximately $7\,s$ after the EPC ignition; it is when the lift-off begins. The total ignition time of the boosters is $130\,s$. Before they flame out, they have already contributed 90% to the total launcher thrust, and they are jettisoned away from the main stage. The booster separation takes place at the mean altitude of $70\,km$ and while the launcher is traveling with approximately $2\,km/s$.

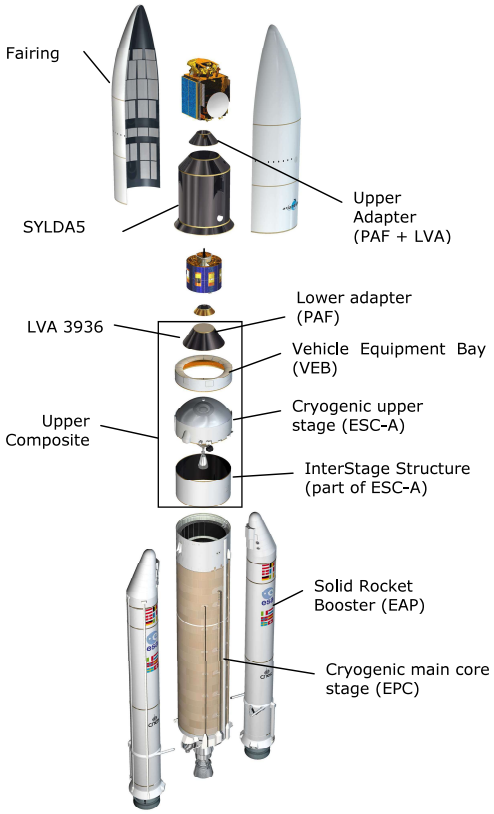

Figure 1.2.1: Schematic of launcher along with its major components. [Arianespace, 2016]

Moving upwards to the launcher structure, there comes the cryogenic upper stage (French: Etage Supérior Cryotechnique - ESC). The diameter of the ESC is the same as the one of EPC whilst its height is $4.711\,m$. It has a total dry mass of $4.5\,t$ and it is loaded with $14.9\,t$ of liquid propellants (LO_x and LH_2). The ESC is ignited a few seconds after the separation from the main stage. Its total combustion time is $945\,s$ and generates thrust of $67\,kN$.

The payload, mainly satellites, is located on top of the launcher and it is covered by a $17\,m$ tall fairing, weighing $2.7\,t$. The fairing has a conical shape and is incorporated for aerodynamic purposes and to protect the payload and the launcher from the intense phenomena that take place while still inside the atmosphere (i.e. aerodynamic heat, friction etc.). The fairing is separated from the launcher approximately $220\,s$ after lift-off, while the launcher is located at the altitude of $124\,km$ and traveling with a speed of $2.4\,km/s$.

Graphical representation of a typical launch profile along with the major milestones can be observed in Figure 1.2.2. The chronological point after the launch countdown is H_0. Then, H_1 is defined as the point of main boosters flame out and jettison while H_2 as the point of the

main stage separation. The main events of launch are listed in Table 1.2.1 along with their corresponding time of occurrence.

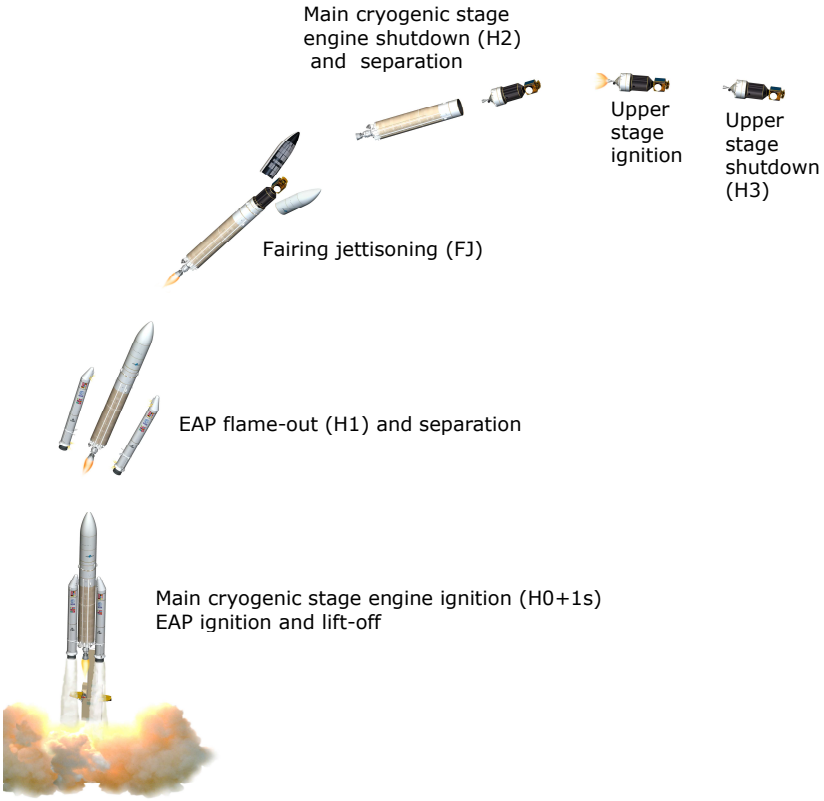

Figure 1.2.2: Ariane 5 typical mission profile. [Arianespace, 2016]

Table 1.2.1: Main events of launch along with the corresponding time of occurrence with respect to H_0. Montsarrat [2017]

Main events of launch	
$H_0 - 6'30''$	Termination of tanks topping up
$H_0 - 4'$	Pressurization of the EPC tanks
$H_0 - 3'10'$	Pressurization of the ESC-A tanks
$H_0 - 1'55'$	Termination of ESC-A ground pressurization
$H_0 - 3''$	Helium pressurization activated
$H_0 + 1''$	Main engine ignition
$H_0 + 7''$	Ignition of EAP and lift-off
$H_0 + 47''$	Maximum in dynamic pressure
$H_0 + 2'22''$	Solid rocket boosters (EAP) dropped - H_1
$H_0 + 3'43''$	Fairing jettisoned
$H_0 + 8'55''$	EPC separation - H_2
$H_0 + 28'15''$	Upper stage separation

1.3. Cryogenic tanks

The subject of the present study is the behavior of pressure in the upper stage cryogenic tanks. There are two cryogenic tanks containing launcher propellant, Liquid Hydrogen (LH_2) and Liquid Oxygen (LO_x). The representation of the tanks can be observed in Figure 1.3.1. On top is located the LH_2 tank, in a way enclosing the LO_x tank, with liquid hydrogen being the fuel and liquid oxygen being the oxidizer.

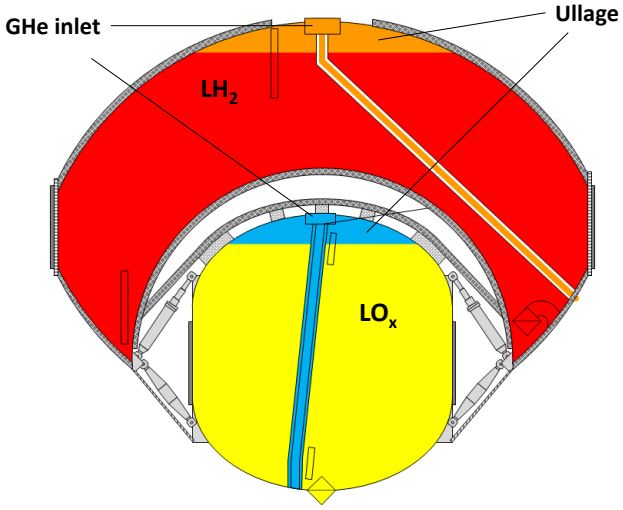

Figure 1.3.1: LH_2 (in red) and LO_x (in yellow) cryogenic tanks 2D sketch. Montsarrat [2017]

Tanks are filled and pressurized while still on the ground. The typical evolution of pressure during the ground pressurization phase is presented in Figure 1.3.2. It can be seen that both tanks are pressurized before launch to a maximum desired pressure P_{max}.

The LH_2 tank is pressurized by gaseous helium (GHe) up to the desired pressure level only once. Immediately after pressurization end, a slight pressure drop is noticed (small spike) and right again the pressure rises to a slightly higher level. The later pressure rise that is noticed can be attributed to the liquid hydrogen evaporation near the gas-liquid interface. This is mainly caused due to the high temperature difference between the two components (GHe is warmer than LH_2) and the external heat flux that affects the tank.

In the case of the LO_x tank, the pressure evolution is relatively different. The LO_x tank is pressurized to a lower desired pressure, however one pressurization cycle is not sufficient to maintain the pressure level. Three pressurization cycles are required in total in order to reach the desired pressure level. For this purpose the pressurization process starts earlier than in the LH_2 case. The first two pressurization processes are done using GHe stored at the ground while the third pressurization is done using GHe from the on-board helium tanks. Especially in the first two pressurization attempts a gradual pressure drop can be noted in the relaxation period. This can be again attributed to the phase change mechanism, however this time, condensation is the main driver of this phenomenon.

Analytical elaboration on the pressure and phase change mechanism will follow up next in Section 1.4

As already stated, during launcher ascent phase, pressure evolution in the upper stage tanks is not showing a constant behavior. More specifically in the case of LO_x tank sudden pressure rise is noticed soon after launch while in the case of LH_2 sudden pressure drops take place. This is not a fixed pressure behavior and it varies from flight to flight. The pressure evolution of 5 flights is demonstrated in Figure 1.3.3.

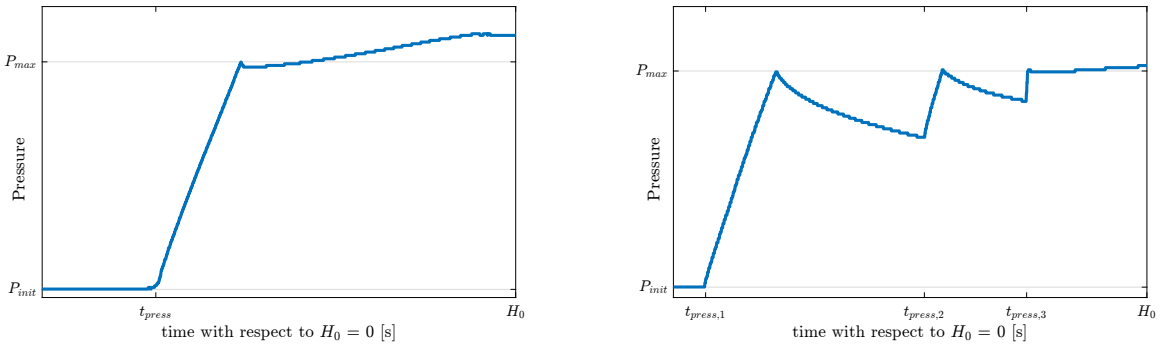

(a) LH_2 tank (b) LO_x tank

Figure 1.3.2: Cryogenic tanks pressure evolution during ground pressurization phase.

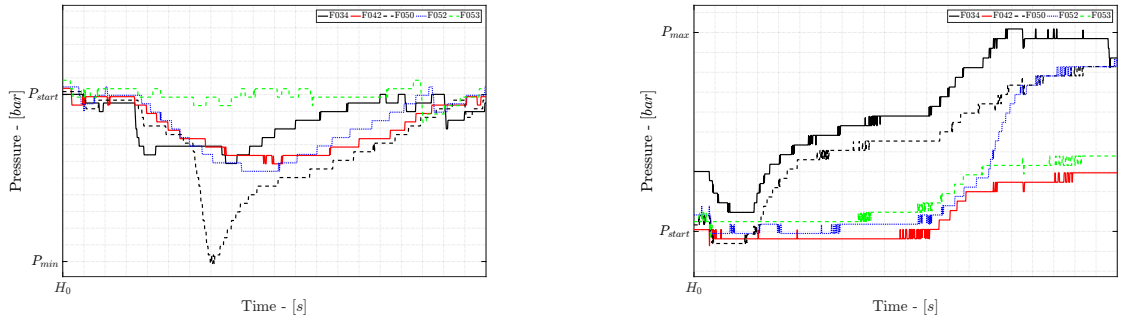

(a) LH_2 tank (b) LO_x tank

Figure 1.3.3: Cryogenic tanks pressure evolution during ascent phase for different flights.

It can be seen that pressure behavior differs from flight to flight. There are flights without any significant pressure change in both the cryogenic tanks (e.g. flight F053), while there are others that demonstrate sudden pressure drop or rise (e.g. flight F050) . In total, 61 flights of Ariane 5 are analyzed in order to investigate the fluctuating pressure behavior. These 5 flights demonstrated in Figure 1.3.3 are just an example of the different types of pressure evolution that may exist. Both the ground pressurization and the ascent phase may affect pressure behavior and as a result both phases are included in the scope of the present thesis.

1.4. Pressure change

The ullage pressure change mechanism has already been identified by many studies [Arndt, 2011; Ludwig and Dreyer, 2012; Liu et al., 2016, 2017]. Pressure change is driven by the evaporation of the liquid component and the condensation of the gaseous component inside the tanks. Heat transfer between the warmer ullage/tank walls and the cooler liquid can result in the phase change from liquid to gas and viceversa.

The fuel tanks of the upper stage compartment are filled with cryogenic oxygen and hydrogen. The term cryogenics refers to materials that are at very low temperature. At atmospheric pressure, oxygen and hydrogen need to be at very low temperature in order to retain liquidity. Oxygen, in order to be in its liquid phase at atmospheric pressure $p \sim 1\,bar$, needs to maintain its temperature below $T \sim 90\,K$ [Hoge, 1950] while hydrogen should maintain its temperature even lower, below $T \sim 20\,K$ [Hoge and Arnold, 1951]. The saturation curves of the two substances are demonstrated in Figure 1.4.1. A combination of temperature and pressure below the curve will result in the liquid phase of each substance respectively. Pressure change will stop once equilibrium in evaporation and condensation rates is reached.

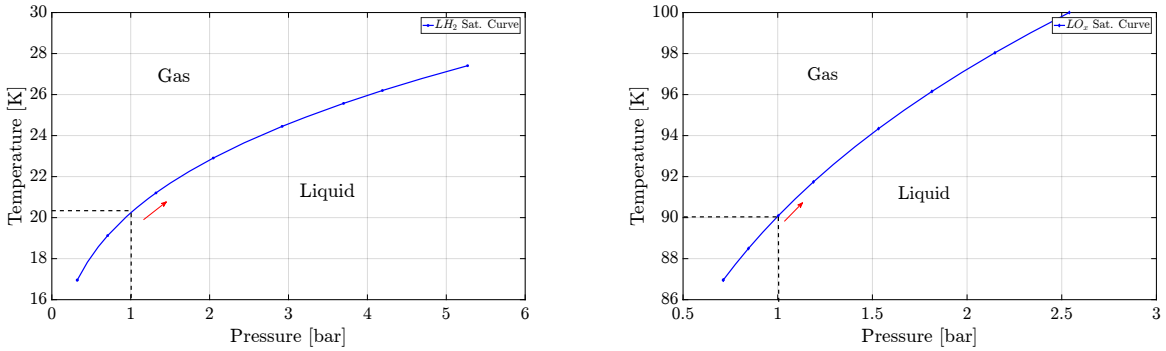

(a) Hydrogen (b) Oxygen

Figure 1.4.1: Hydrogen and oxygen saturation curves

During the initial tank loading with propellants, tank pressure is equal to atmospheric. The propellants need to be below the above mentioned temperatures in order to be in their liquid phase.

The filling of the tanks is done in multiple steps. Initially the tank is filled to the top while it is still open. Evaporation constantly occurs and the pressure is relieved through the opening. As a result, the liquid level decreases and more filling processes should follow until a stable pressure level is reached. However, the liquid is still at the saturation temperature and boiling. After that, the tanks are sealed before the pressurization process can be initiated. This means that there will also be gaseous phase of the propellant inside the tank ullage. The tanks are now pressurized by gaseous helium. The pressurant gas is at higher temperature, around $110\,K$. Filling the tanks with GHe will mean the increase of the ullage pressure as well as the partial pressure (locally) of the gaseous propellants.

For the LH_2 tank, an increase in the partial pressure of the GH_2 will alter the saturation temperature (T_{sat}) to a higher level. This means that the gaseous hydrogen that was at that moment below the new saturation temperature, will condensate leading to a small pressure drop. This is indeed obvious in Figure 1.3.2 (a) right after reaching P_{max}. However, in the same figure, it is evident that pressure quickly rises again without any further pressurization by GHe. The high temperature difference between GHe and LH_2 will result in significant heat transfer between these substances. Additionally, external heat flux (due to the higher ambient temperature) will also affect LH_2 through the tank walls. As a result of the two aforementioned phenomena, the temperature near the wall and the free-surface (liquid-gas

interface) will rise, reaching the new T_{sat}, leading to the evaporation (phase change) of the LH_2. This will balance the initial condensation pressure drop effect, and then dominate, leading to a gradual pressure rise.

In the case of LO_x it is noticed that multiple pressurization cycles are necessary due to the gradual pressure loss that is observed right after the pressurization end. In the LO_x tank the pressure change mechanism differs from the one that was described in the previous paragraph. At this time, temperature difference is of lower significance as at atmospheric pressure conditions, oxygen's T_{sat} lies closer to the pressurant gas temperature. Additionally, due to the higher temperature, lower heat flux from the outside enters the tank. As a result, condensation of GO_x in the ullage dominates the evaporation due to the partial pressure increase of GO_x during pressurization. Consequently, a gradual pressure drop is noted. Reaching the third pressurization cycle, now the pressure loss is less, and the ullage pressure stabilizes over a specific level. At this moment, after three pressurization cycles, GHe concentration in the ullage is high, with only a few GO_x left as it earlier condensed. Evaporation and condensation rates are now balanced, leading to a stable ullage pressure.

The difference between the tank is mainly because of the difference in the heat fluxes that was already pointed out and because of the difference in the density of the gaseous propellants. The density of GO_x is much higher than the one of GHe. As a result, during pressurization the mixing is probably not perfect, because GO_x is significantly heavier and it is pushed to the bottom. Thus, it experiences a higher partial pressure increase than the GH_2 which has a notably lower density. These are the two major reasons for the pressure drop due to condensation during the pressurization relaxation phase.

Tank pressurization by gas injection (in this case GHe) is referred to as active pressurization, and there are already plenty of studies in this field. However, tank pressure can also rise without any other further addition of pressurant gas, as already described above. This phenomenon mainly happens due to heat transfer from the pressurant gas or the environment to the cryogenic liquid. In the literature this phenomenon is referred to as self-pressurization. Both are regarded as important phenomena that take place during launcher ground pressurization and ascent phase.

The tank temperature profile as well is of major importance, and should be at this point introduced in order to aid the reader's further understanding. As it can be easily understood, mixing of two substances of different temperature will result in the heat transfer between those. The external heat flux will also affect the heat transfer inside the tank. As a consequence, the temperature profile will vary with tank height, forming numerous temperature zones. It is expected that higher temperature will be present near the dome of the tank where the pressurant gas is injected, while lower temperature will be present near the bottom. Higher temperature will also be present at the near wall region due to the external heat flux. The resulting temperature profile is referred to as thermal stratification. An example of such profile can be observed in Figure 1.4.2 for the liquid fraction of the tank. For height $h = 0$ temperature is the lowest while it increases with increasing height (i.e. approaching the liquid-gas interface). The CFD results of Liu et al. [2017] are also visually presented in Figure 1.4.3 for the whole tank (i.e. liquid + ullage) for different ambient temperatures.

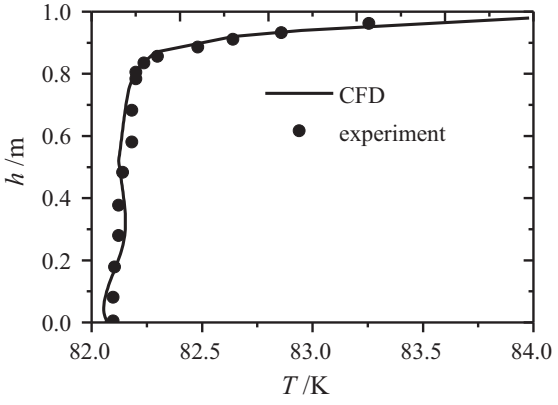

Figure 1.4.2: Temperature distribution over height for the liquid fraction of cryogenic tanks based on experiments of Arndt et al. [2009] and Kumar et al. [2007]. Demonstration of CFD agreement of the model developed by Liu et al. [2017].

It can be understood that temperature profile is of major importance as the phase change and in turn the pressure change mechanism is driven by the heat transfer between the gas-liquid and tank walls-liquid components.

It is during the ascent phase, that the phenomenon of sloshing occurs (i.e. fluidic motion development of liquids enclosed into non-stationary containers). Liquid sloshing results in the mixture of fluid from the lower tank levels with fluid that is located on top. Sloshing can also favor the creation of waves and/or the launch of liquid droplets higher, near the ullage dome. As a consequence, the previously stratified temperature profile breaks. This is referred to as thermal destratification and it is believed that is the main reason for pressure fluctuations during launcher ascent phase when the sloshing phenomenon occurs.

Thermal destratification will alter the saturation conditions. When cold liquid from the bulk is moved to the top near the surface (due to sloshing) saturation pressure decreases. Therefore, the gaseous component near the surface condenses. Secondary but also important reason in the case of wave formation in the tanks, is that liquid reaching a higher region of the ullage will force it to cool down. Cooling inherently leads to pressure drop.

Splashing can also cause evaporation and a pressure increase when liquid splashes against a warm wall. The same happens when the liquid reaches regions of low partial pressure of the gaseous propellant.

It should be made clear that condensation and evaporation depend on the partial pressure of GH_2/GO_x in the ullage. When the partial pressure is higher than the saturation pressure, condensation will dominate but if the partial pressure is lower, then evaporation will take place. The saturation pressure is dependent on the liquid temperature at the surface.

It is therefore believed that studying the cryogenic tanks throughout the ground pressurization as well as the ascent phase, can lead to valuable conclusions regarding the cause of the pressure drop/rise phenomena. It is up to now understood that active pressurization, self pressurization and sloshing motion can be of major importance and further investigation of these processes is attempted through the literature review.

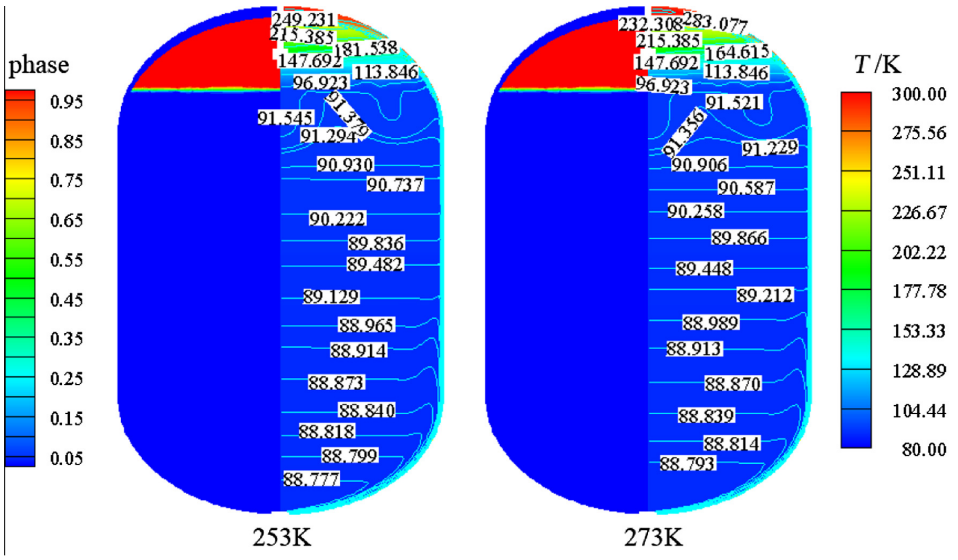

Figure 1.4.3: Numerical results of Liu et al. [2017] on thermal stratification of a LO_x tank for different ambient temperatures.

1.5. Research framework

The project is focused on the ascent phase of the Ariane 5 launcher. In total, 61 past flights of the launcher are investigated.The objective of the research project, as it was set up during the initial steps, is to provide understanding on why the pressure fluctuations occur, to find out at what extent sloshing motion is responsible for those, to identify connection with other flight parameters and to attempt a prediction of the min/max pressure change magnitude. This is achieved by analyzing the available flight data of previous flights, implementing a statistical approach on the available data and running CFD simulations of the liquid sloshing motion inside the tanks.

A schematic of the research project is presented in Figure 1.5.1 where the steps, the expected results and the outcome are presented. The faded text corresponds to goals that were not initially included in the framework. Due to several limitations that are explained later on, these goals have not been reached.

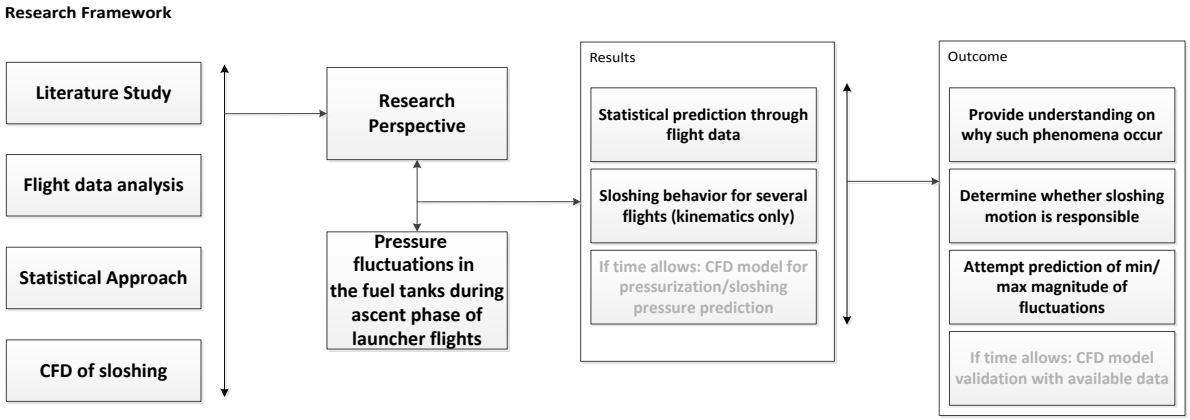

Figure 1.5.1: The research framework as it was set-up during the initial steps of the project

"I am indebted to my father for living, but to my teacher for living well."

-Alexander the Great, King of Macedon, 356–323 BC

2

Theoretical Background

Before the preparation of the present report, an extensive literature study has been conducted, aiming to the identification of the major parameters that affect the pressure behavior inside the cryogenic tanks. In the present chapter, the literature review is again briefly presented. In addition, the theoretical background of the applied methodology is also explained.

2.1. Brief literature review

There are already several experimental and numerical studies concerning the pressure behavior in cryogenic tanks. Through these studies it is attempted to gain a better understanding on the phenomenon itself, and identify the parameters that drive the noticed pressure fluctuations.

The tank pressure behavior is studied with respect to active pressurization (i.e. pressurization by means of gas injection), self pressurization (i.e. pressurization due to heat transfer from the environment) and pressure change due to sloshing.

Active pressurization

Initial steps of experimental research on cryogenic tanks pressurization can be traced back to Nein and Head [1962]; Nein and Thompson [1966]. Their research concluded that extensive mass transfer takes place between the cryogenic liquid and the pressurant gas. The major heat transfer path is through the liquid-gas interface while heat transfer through tank walls is of minor significance. Additionally, by varying the inlet temperature, they showed that for higher temperature, the phase change mechanism is dominated by evaporation.

Lacovic [1970] concluded that more pressurant gas is required for higher ullage volumes and Van Dresar and Stochl [1993] indicated that the mass transfer mechanism is not constant, but changes several times from condensation to evaporation and vice-versa.

In more recent studies, Ludwig and Dreyer [2012]; Ludwig et al. [2013]; Ludwig and Dreyer [2014] held experiments and developed a numerical model for an LN_2 tank pressurized by GN_2 and GHe, in order to investigate the pressurant gas requirements. The concluded that the pressure drop after the pressurization (relaxation phase) is directly related to the final tank pressure, the pressurant gas type and its temperature. It was in their study, where they highlighted the thermally stratified tank profile. Higher temperature is present near the tank dome but the temperature becomes lower while approaching the tank's bulk. Heat transfer through the liquid-gas interface (dominant) and the tank walls, alters the liquid temperature at the nearby regions. The pressurization time is also pointed out as having effect on the phase change, as faster pressurization leads to less condensation (i.e. less pressure drop).

Among many numerical studies on the field, the one of Kim et al. [2012] is of great interest. They developed a mathematical model for the transient thermal analysis of a cryogenic LO_x tank using GHe during the pressurization phase (neglecting external heat flux). They confirm that pressurization completion is followed by ullage temperature and ullage pressure drop. The pressure drop magnitude is independent to the pressurization level however higher tank pressurization results in higher evaporation rate within the tank. The effect of the ullage volume is significant, as higher ullage volumes lead to smaller pressure drops.

Later, Wang et al. [2015] developed a multicomponent model for the prediction of thermal distribution and pressure evolution in GHe pressurized cryogenic LO_x and LH_2 vessels. They concluded that the phase change mechanism differs between the two tanks as for the LO_x condensation is dominant while evaporation is higher for the case of the LH_2 tank.

Finally, Liu et al. [2017] built and validated a numerical model based on the experiments of Kumar et al. [2007]; Arndt [2011] (Figure 1.4.2). Their study highlighted that intense boiling takes place during the LO_x open-tank filling process which is later reduced as time goes by. They also showed that the condensation is dominant (GO_x of ullage condenses) after the pressurization process end and that the effect of the external heat flux can be neglected. Additionally, their model nicely captured the temperature stratification as shown in Figure 1.4.3.

Self pressurization

Self pressurization is an important aspect of cryogenic tanks. This phenomenon refers to the heat transfer between the ambient and the tank system, as well as the heat transfer from the ullage to the liquid through the interface and the tank walls.

Initially, Aydelott [1967, 1969] conducted research related to the self pressurization of spherical cryogenic LH_2 tanks. In his studies, he investigated the effect of heat transfer rate, heat flux distribution, ullage volume and tank size on the pressure behavior. He concluded that pressure change depends on the ratio of the total heat to the tank volume. Additionally, heating configuration plays an important role, as uniformly or top-heated tanks showed higher evaporation rates. Increased heat flux also leads to a higher evaporation rate within the tank. All these are important parameters having in mind the different size and location of our LH_2 and LO_x tanks.

Other researchers like Hasan et al. [1991]; Van Dresar et al. [1992] investigate the effect of heat flux magnitude and fill level percentage on the pressure of cryogenic LH_2 tanks. The indicated the importance of the wetted-wall area on the results, as it affects the amount and the way that ambient heat leaks inside the system. For the spherical tank they used in their experience, higher pressure rise was observed for higher heat flux and fill levels. Later on, Lin and Hasan [1992], highlighted the effect of liquid thermal expansion which in turn leads to higher pressure rise for higher fill levels.

In more recent study, Seo and Jeong [2010] made an experimental and a numerical investigation of self pressurization of an LN_2 tank. Among their conclusions they stated that the larger the liquid fraction the larger the pressure rise would be. Additionally, higher heat leak will lead to a higher initial evaporation rate as well as to a longer transient period (i.e. more time will be required to reach the maximum pressure).

Finally, Liu et al. [2016] developed a CFD model for the prediction of the upper stage LO_x tank pressure evolution combining active and self pressurization processes. It appeared that the aerodynamic heat influences thermal stratification and pressure evolution. Their model showed a notable pressure drop during the self pressurization phase for LO_x which is delayed when the aerodynamic heat term is incorporated into the model (sign of increased evaporation rate).

Sloshing

During the ascent phase the acceleration and the roll rate profile of the launcher varies with respect to time in every direction. When a liquid is enclosed into a non stationary container, a fluidic motion is developed known as sloshing. Stable or unstable sloshing can be noted inside the containers. Unstable sloshing is characterized by breaking waves and/or the ejection of liquid into the ullage; it can be considered responsible for the thermal destratification of the system and the pressure drop/rise.

An experimental setup of 1750 l tank with LH_2 was used by Moran et al. [1994] to investigate pressure behavior under the effect of sloshing. Among others, they focused on the effects of ullage volume and sloshing amplitude on the pressure evolution. Using helium as a pressurant gas showed a slight increase of pressure during sloshing for all cases. On the other hand, when they used gaseous hydrogen as a pressurant, unstable sloshing led to a sudden pressure collapse while stable sloshing led to a gradual pressure drop. For the cases of stable sloshing (with GH_2), lower ullage volumes lead to higher pressure drop while not distinctive trend could be observed for the unstable conditions. It is clear that the concentration of GHe (non-condensable gas) in the ullage dictates the amount of condensation, significantly affecting the pressure behavior during sloshing.

An extensive effort in the field of cryogenic sloshing was done by Arndt [2011] during his PhD research. Cooperation with other researchers from ZARM institute (Center of Applied Space Technology and Microgravity) of University of Bremen, led to a series of publications [Arndt et al., 2008; Arndt and Dreyer, 2008; Arndt et al., 2009]. He focused on the effect of sloshing on the pressure and temperature behavior of a cryogenic LN_2 tank. He investigated three different types of pressurization (self pressurization, GN_2 pressurization and GHe pressurization) to see the impact they have on the results. He concluded that for the same starting pressure, GN_2 pressurization yields higher pressure drops during sloshing than self-pressurization. The higher the starting pressure the higher the magnitude of pressure drop. He also observed that for the two aforementioned cases (i.e. self and GN_2 pressurization) pressure reaches a minimum after sloshing initiation and then stabilizes as the liquid becomes homogeneous in terms of temperature. On the other hand, pressure behavior while pressurizing by GHe showed that it is highly dependent on the helium concentration into the ullage. High helium concentration leads to no pressure drop at all. Instead, pressure rises immediately after sloshing event initiation. For lower helium concentrations, pressure initially drops but starts to rise again after a certain point.

Ludwig et al. [2013] also studied liquid sloshing in an LN_2 cylindrical tank. Based on a previous model [Das and Hopfinger, 2009] they attempted to expand it in order to calculate temperature and pressure evolution. They found that for the same sloshing amplitude, experiments with higher sloshing frequency led to higher pressure drops. More specifically they found that pressure drop magnitude will increase the closer we get to the natural frequency of the system, while for higher frequencies, it will decrease again. After some point, liquid mixing results to a homogeneous temperature profile, thus pressure collapse stops and pressure retains a stable behavior. Long time ago, the effect of the excitation near the natural frequency for spherical tanks was also investigated by Stofan et al. [1962]; Sumner [1966]. It was shown that specific excitation frequency-amplitude combinations can result in unstable sloshing inside the tank and in turn to higher pressure change magnitude.

The study of Joseph et al. [2014] involved the numerical analysis to capture the two-phase, multi-species slosh phenomenon and predict pressure drop in an LO_x tank. They concluded that higher maximum sloshing angle can lead to higher pressure drops while high helium concentration in the ullage can lead to lower pressure drops. Due to the higher thermal capacity of helium (compared to GO_x), more helium in the ullage would mean less temperature change and hence lower pressure fall. Additionally, since helium is non-condensable, higher helium concentration in the ullage will also mean lower condensation rate during ullage cooling. These phenomena can be related to the lower pressure drop. Using gaseous helium as pressurant proves to minimize the effect of sloshing over pressure drop as was also observed

by Moses and Nein [1962]; Nein and Thompson [1966]. In the same study of Joseph et al. [2014] there is also reference to the higher liquid-gas interface area that sloshing might cause due to waves and droplets formation. Additional area leads to the increase of the heat transfer rate resulting in increased evaporation/condensation. Furthermore, liquid properties can also affect sloshing behavior as density and viscosity can favor or disfavor the damping of the phenomenon.

Furthermore, Van Foreest [2010]; Van Foreest et al. [2011]; Van Foreest [2014] also conducted his PhD research on cryogenic sloshing phenomena. He developed a model of cryogenic sloshing including heat and mass transfer. He concluded that temperature stratification during tank pressurization is the main reason for pressure fluctuations during sloshing. The pressure drop effect is mainly due to condensation which can be explained by the destruction of the thermal gradient near the liquid-gas interface, causing the near surface liquid temperature to drop. Tank walls play an important role in the heat transfer from the hotter ullage to the colder liquid as well. An important conclusion of his work is that he highlighted the limitation of Flow3D in predicting pressure during sloshing. More specifically he proved (in cooperation with FlowScience) that the volume-of-fluid method and single average temperature in a cell is insufficient for the accurate prediction of temperature development in two-fluid systems while sloshing.

A comparison of several CFD codes for the modeling of liquid sloshing into tanks have been assessed by Cariou and Casella [1999]. It should be stated that despite there is no direct conclusion on which code should be used in order to accurately simulate sloshing, there is clear indication that the Volume of Fluid (VOF) methodology dominates among the tested cases. Furthermore, there is not clear indication whether the effect of turbulence should be neglected or not (in order to save computational time), as both laminar and turbulent codes produce decent results. Finally, incompressible approaches outnumber the compressible ones, as well as viscous effects are clearly incorporated in the majority of the codes.

An extensive study was performed by Godderidge et al. [2006] where they initially verified and validated a series of CFD approaches on lateral sloshing and later [Godderidge et al., 2009] they proposed a numerical model for the simulation of sloshing. In their studies, they indicated the importance of turbulence in sloshing modeling, and they used the $k-\epsilon$ turbulent model for their approach. In their studies they also highlighted the effect of surface tension. The significance of this effect can be derived through the dimensionless Bond number which is the ratio of gravitational to surface tension forces.

The volume of fluid (VOF) method is incorporated in the majority of the CFD studies obtained through the literature review [Godderidge et al., 2006, 2009; Singal et al., 2014; Joshi et al., 2017; Cariou and Casella, 1999]. The VOF method was firstly introduced by Hirt and Nichols [1981]. It should be mentioned that, Dr. C. W. (Tony) Hirt, being one of the pioneers of the VOF method, also founded FlowScience Inc, the creator of the FLOW-3D software which is going to be used for the present study.

2.2. CFD governing equations

The Volume of Fluid (VOF) method is an Eulerian finite difference numerical method that is used to track the free boundaries (i.e. free surface) of a liquid. It was firstly introduced by Hirt and Nichols [1981].

The VOF method is based on a function F which defines the ratio of the fluid fraction inside a specific mesh element. Function F equals to 1, if the mesh element is completely filled by the liquid while F equals to 0, if the liquid is completely absent for the specific mesh element. Intermediate values are used to describe a fluid/void combination for each specific mesh element, meaning that a free surface is present within the cell. The free-surface orientation can be determined through the rate of change of F. The 3-dimensional time dependence of the liquid fraction is described by

$$\frac{\partial F}{\partial t} + u\frac{\partial F}{\partial x} + v\frac{\partial F}{\partial y} + w\frac{\partial F}{\partial z} = 0 \tag{2.2.1}$$

In the present approach, for the simulation of the fluid motion inside the cryogenic propulsion tanks, an incompressible fluid is assumed. The incompressible Navier-Stokes equations are presented in its 3-dimensional form in order to be in line with the current project. In their original publication of the method, Hirt and Nichols [1981] presented a 2-dimensional application, however they clearly stated that their method is capable of solving 3-dimensional problems as well. Equations (2.2.2) to (2.2.4) represent the momentum equations (density normalized to unity) and Equation (2.2.5) the incompressibility condition, for a cartesian co-ordinate system.

$$\frac{\partial u}{\partial t} + u\frac{\partial u}{\partial x} + v\frac{\partial u}{\partial y} + w\frac{\partial u}{\partial z} = -\frac{\partial p}{\partial x} + g_x + \nu[\frac{\partial^2 u}{\partial x^2} + \frac{\partial^2 u}{\partial y^2} + \frac{\partial^2 u}{\partial z^2}] \tag{2.2.2}$$

$$\frac{\partial v}{\partial t} + u\frac{\partial v}{\partial x} + v\frac{\partial v}{\partial y} + w\frac{\partial v}{\partial z} = -\frac{\partial p}{\partial y} + g_y + \nu[\frac{\partial^2 v}{\partial x^2} + \frac{\partial^2 v}{\partial y^2} + \frac{\partial^2 v}{\partial z^2}] \tag{2.2.3}$$

$$\frac{\partial w}{\partial t} + u\frac{\partial w}{\partial x} + v\frac{\partial w}{\partial y} + w\frac{\partial w}{\partial z} = -\frac{\partial p}{\partial z} + g_z + \nu[\frac{\partial^2 w}{\partial x^2} + \frac{\partial^2 w}{\partial y^2} + \frac{\partial^2 w}{\partial z^2}] \tag{2.2.4}$$

$$\frac{\partial u}{\partial x} + \frac{\partial v}{\partial y} + \frac{\partial w}{\partial z} = 0 \tag{2.2.5}$$

In the above equations, u, v and w are the velocity components, g_x, g_y and g_z are the acceleration components and ν is the kinematic viscosity.

The current project deals with the sloshing motion of liquid inside a moving container. The acceleration of a fluid element with respect to a non-inertial frame of reference can be derived by the Equation (2.2.6). The notation that is used is taken from the derivation of the acceleration of a particle in a rotating reference frame of Etkin [1982].

$$\vec{g}_{par} = g_{grav} + \frac{\delta^2 \vec{r_o}'}{\delta t^2} + \frac{\delta^2 \vec{r}}{\delta t^2} + \frac{\delta \vec{\omega}}{\delta t} \times \vec{r} + 2\vec{\omega} \times \frac{\delta \vec{r}}{\delta t} + \vec{\omega} \times (\vec{\omega} \times \vec{r}) \tag{2.2.6}$$

In Equation (2.2.6), g_{grav} is the gravitational acceleration. The reader can consult Figure 2.2.1 for the representation of the co-ordinate systems and the particle P. The reference frame $O'x'y'z'$ is fixed. The translational acceleration $\frac{\delta^2 \vec{r_o}'}{\delta t^2}$ and the rotational speed $\vec{\omega}$ of the rotating reference frame $Oxyz$, are the required user inputs for the calculation of the fluid

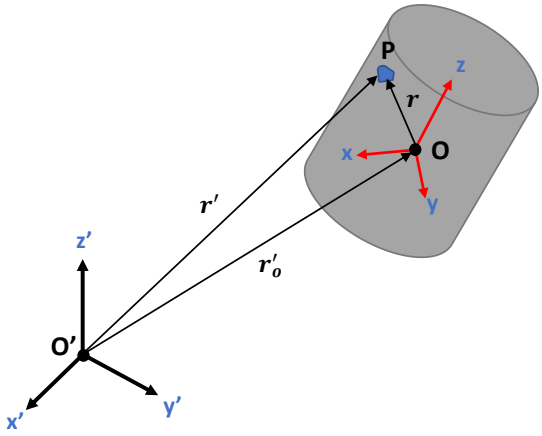

Figure 2.2.1: Fixed and rotating frame of reference representation. Notation based on Etkin [1982].

particle's acceleration. The rotating reference system $Oxyz$ is attached to the launcher center of gravity which is also a required user input.

Another important consideration is that the surface tension can be ignored as the gravitational forces dominate the surface tension ones (i.e. the launcher experiences very high accelerations (see Figure 3.2.3)). This can be expressed by a Bond number greatly higher than one.

$$Bo = \frac{\rho g L}{\sigma} \gg 1 \tag{2.2.7}$$

In cases where the second fluid (in this case the gas) has much smaller density than that of the liquid, a simplified model of the VOF method is suggested by FlowScience [Hirt and Barkhudarov, 2013] . This approach manages to save computational time as the second fluid is neglected and is now represented by a void region.

The properties of the void region are uniform and the void itself acts as if it was one single cell. For the purpose of liquid sloshing this approach looks promising as the low density gas is not expected to have major impact on the liquid motion.

In the present approach, no thermodynamic calculations are involved in the simulation, so it is beneficial to model the ullage volume as a single cell called *void* or *bubble* with a constant pressure.

2.3. Frequency analysis

The frequency and amplitude of the vibrations can play an important role on the response i.e. the sloshing behavior. According to the research of Stofan et al. [1962]; Sumner [1966]; Moran et al. [1994]; Ludwig et al. [2013], if the excitation of the tank is close to the natural frequency of the system, then it is likely that more intense pressure changes will take place. This is related to the unstable sloshing that is developed inside the tank system.

As presented in the research of Moran et al. [1994], the natural frequency, f_n, of a system of a partially filled spherical tank can be estimated by Equation (2.3.1). This relationship was earlier found by Sumner [1966].

$$f_n = \frac{1}{2\pi}\sqrt{\frac{\lambda g}{R}} \tag{2.3.1}$$

In the above equation, g is the acceleration of gravity, R is the tank radius and λ is an empirical constant based on the fill height and the tank radius as shown in Table 2.3.1

Table 2.3.1: Estimation of λ based on fill height h and tank radius R

$\frac{h}{2R}$	$\sqrt{\lambda}$
0.1	1.0573
0.2	1.0938
0.3	1.1370
0.4	1.1893
0.5	1.2540
0.6	1.3376
0.8	1.4528
0.9	1.9770

According to the research of Ludwig et al. [2013], the boundaries of planar and non-planar sloshing can be defined by Equation (2.3.2). In this equation, f_o is the excitation frequency, x_a is the excitation amplitude and β_i for $i = 1, 2, 3$ is specific parameters determined by Miles [1984], which give the boundaries of the sloshing modes for a circular cylindrical tank.

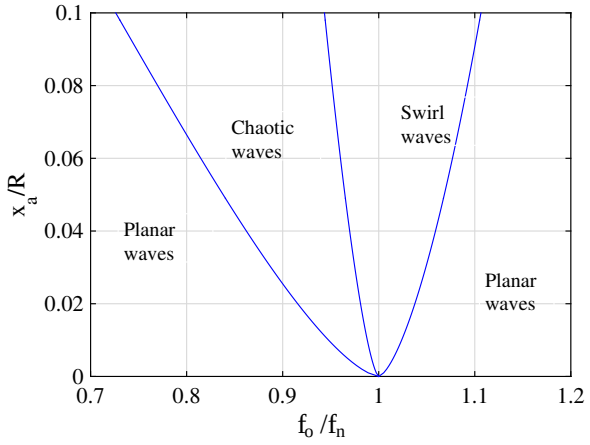

Figure 2.3.1: Diagram of dimensionless forcing amplitude as a function of frequency ratio as derived from Equation (2.3.2) of Miles for circular cylindrical tanks. [Montsarrat, 2017]

$$[\frac{f_o}{f_n}]_i = [(1.684\frac{x_a}{R})^{2/3}\beta_i + 1]^{1/2} \tag{2.3.2}$$

Later, Moran et al. [1994] used Equation (2.3.3), which was earlier developed by Stofan et al. [1962] through an experimental and analytical approach on spherical tanks. In this equation, K_1 and K_2 are empirical constants (Figure 2.3.2), X_0 is the excitation amplitude in inches and R is the tank radius in inches.

$$(\frac{f_o}{f_n})^2 = K_1 + K_2(\frac{X_0}{2R})^{2/3} \tag{2.3.3}$$

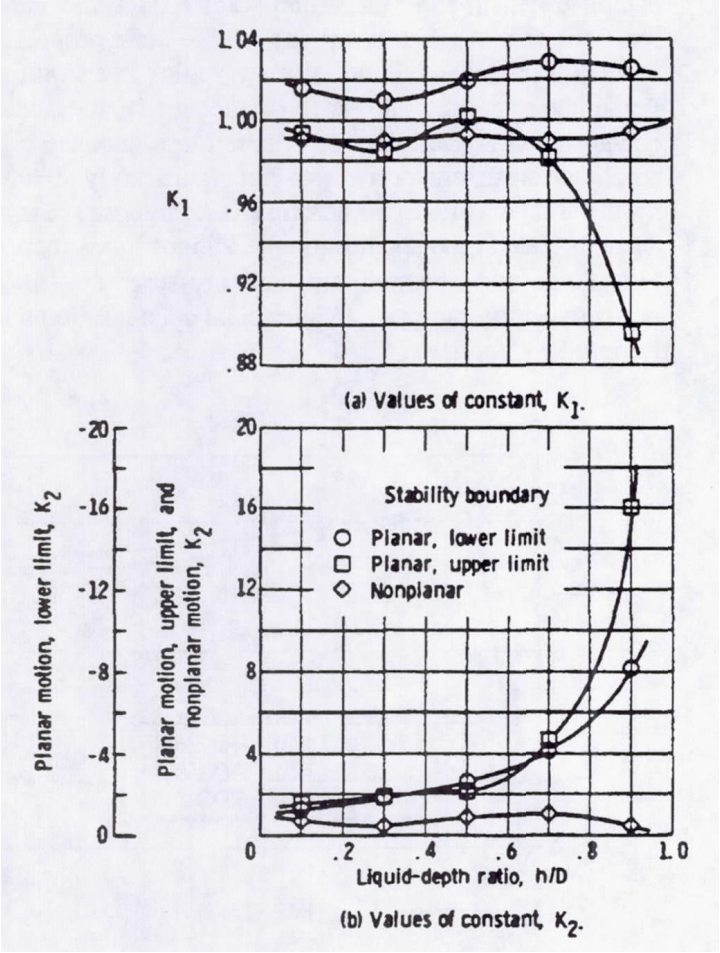

Figure 2.3.2: Empirical coefficients K_1 and K_2 for the calculation of lower/upper limits of planar/non-planar motion Stofan et al. [1962]

Given the fact that the LH_2 tank is not purely spherical, this method can only be used as a rough estimation of the impact of vibration on sloshing. The natural frequency of the system highly depends on the acceleration profile. The natural frequency of the LH_2 is already calculated by the designer for different acceleration magnitudes. The natural frequency of the tank fits well on Equation (2.3.1) for $\sqrt{\lambda} = 2.07$.

Applying equation Equation (2.3.2), the graph of Figure 2.3.1 can be drawn (for cylindrical tanks). The combination of excitation frequency and amplitude can give an idea on whether the response could lie in the area of planar or non-planar waves. A non-planar wave (or chaotic wave) might possibly lead to breaking waves and droplet jettison which in turn increases the change of higher magnitude pressure fluctuations.

However, for spherical tanks, Equation (2.3.3) should be used to obtain the lower/upper limits of the planar/non-planar motion, as shown in Figure 2.3.3. The notation is taken from Moran et al. [1994].

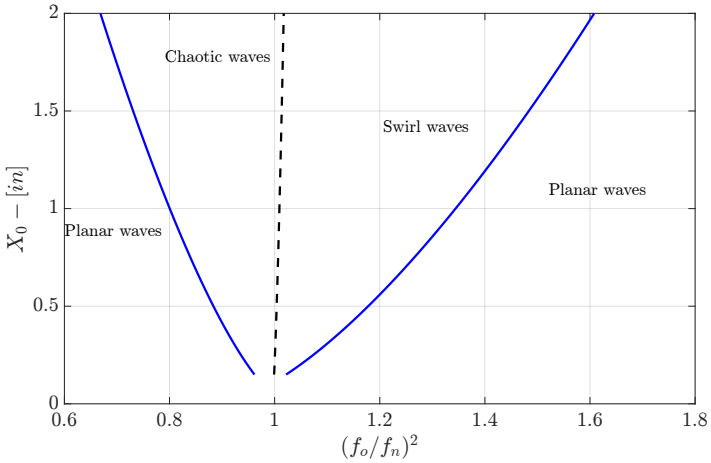

Figure 2.3.3: Lower/Upper limits of planar motion (straight blue) and non-planar limits (dashed black) as derived by Stofan et al. [1962] for spherical tanks (units in inches).

Performing a Fourier analysis on the recorded vibration and plotting the Power Spectral Density (PSD) in terms of a spectrogram, can show which frequencies are dominant during the launcher ascent phase and could possibly lead to valuable conclusion regarding the pressure change magnitude.

2.4. Multiple Linear Regression

Linear regression is a statistical method utilized as a prediction method for a dependent parameter, say Y (the response), from one or a set of more than one independent parameters, say X_1, X_2,...,X_n (the predictors). The prediction is based on a linear model that is built from the predictors and is of the form

$$Y = \beta_0 + \beta_1 X_1 + \beta_2 X_2 + ... + \beta_n X_n + \epsilon \tag{2.4.1}$$

When the model involves more than one independent variables, it is referred as Multiple Linear Regression (MLR). In Equation (2.4.1), the factors $\beta_1, \beta_2, ..., \beta_n$ are the estimates and depict the expected change of the response by the modification of one at a time, predictor. The factor β_0, is the intercept, which is the average value of the response when all the predictors are equal to zero.

The goal of the MLR process is to minimize the prediction error (ϵ) or if expressed mathematically, minimize the sum of squared residuals RSS

$$RSS = \sum_{i=1}^{n} (y_i - \hat{y})^2 = \sum_{i=1}^{n} (y_i - \hat{\beta_0} + \hat{\beta_1} X_{i,1} + \hat{\beta_2} X_{i,2} + ... + \hat{\beta_n} X_{i,n})^2 \tag{2.4.2}$$

The result of multiple linear regression is a table containing the $\hat{\beta}$ coefficients which are the ones that minimize the RSS. The MLR also provide results of the standard error and the t-statistic of each coefficient (Table 2.4.1).

Table 2.4.1: Multiple linear regression results matrix

Param.	Coeff.	Std. Error	t-stat	p-value
X_1	β_1	std err 1	t-stat 1	p-val 1
X_2	β_2	std err 2	t-stat 2	p-val 2
⋮	⋮	⋮	⋮	⋮
X_n	β_n	std err n	t-stat n	p-val n
Intercept	β_0	std err 0	t-stat 0	p-val 0

Additionally, the correlation coefficient of actual versus the predicted values can be used as a measure of accuracy. Higher correlation coefficient will imply better accuracy of the model.

In models with enormous amount of independent variables it is often wise to identify the ones which have the greater impact of the response. Using a model with all the available independent variables might result in poor prediction on the response. A direct approach would be to test all the possible variable combinations in order to reach to a minimum RSS. To avoid that, there are methods of identifying the most important parameters, such as the forward or backward selection methods. In the case of a small amount of predictors, backward selection is an easy way to conclude to the most crucial parameters.

Backward selection is implemented by initially using all the available parameters, say n, into the MLR model. After the initial fit, the variable with the weaker significance (i.e. the one with the highest p-value), is removed and the model is implemented again. Similarly, the same is done with the new model now using the $n-1$ parameters. The process can continue until a threshold significance limit is reached. In this way, only the parameters that have a significant impact on the response variable are taken into account for the creation of the linear model.

Validation is necessary in order to assess the statistical model's performance with respect to its prediction capability. Since the available data is limited and based on the fact that the model should be tested into new, unused data, the $k-folds$ cross validation method is implemented.

According to the $k-folds$ method, the population is split into k equal sized random groups of data. Then, the $k-1$ groups are used for the training of the model i.e. the building of the linear model. The rest (1 group of 1 instance) is used for the model validation. This process is repeated k times and the k results are combined/averaged into a single metric (e.g. mean square error - mse) to correspond to the overall validation performance.

A special case of the $k-folds$ cross validation method is the leave-one-out cross validation method. In this case, k equals to the total number of instances. As a result, each time only one instance is used for the model testing while the rest of the data is used for the training of the model.

There are various software packages and tools to build a statistical model and to implement a cross-validation method (i.e. Matlab, R, python, WEKA). For the present study, WEKA package is used, which is an open source machine learning toolkit built by the University of Waikato, New Zealand [UniversityOfWaikato, 2017]. The results can be also easily verified with the use of the statistical toolkit of Matlab.

The measures that are used by WEKA for the performance assessment of the model are listed below. [Witten et al., 2005]

First of all, the correlation coefficient (R) denotes the relation between the actual response (y) and the predicted response ($\hat{y}$). The values of the correlation coefficient can lay between -1 (perfect negative correlation) and 1 (perfect positive correlation). Values close to 0, indicate a weak correlation between the quantities of interest. Examples of weak and strong correlation are illustrated in Figure 2.4.1.

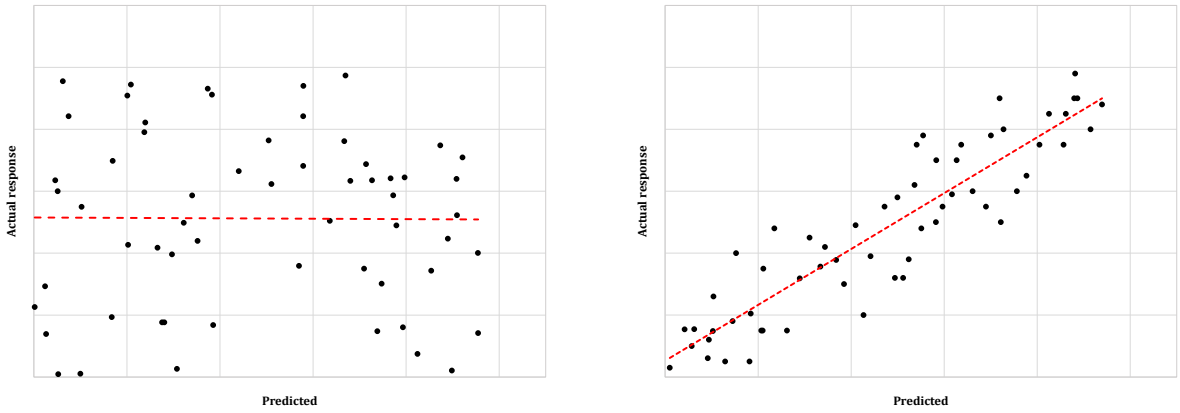

(a) No correlation - $R \sim 0$ (b) High positive correlation - $R \sim 1$

Figure 2.4.1: Weak and strong correlation examples

The mean absolute error (MAE) is a metric that expresses the absolute deviation of the prediction from the actual response and is expressed in the units of the response.

$$MAE = \frac{1}{n}\sum_{i=1}^{n}|\hat{y}_i - y_i| \tag{2.4.3}$$

The root mean square error (RMSE) is the square root of the means of the errors' squared. It is understood that the smaller the MAE and the RMSE are, the better the prediction performance is.

$$RMSE = \sqrt{\frac{1}{n}\sum_{i=1}^{n}(\hat{y}_i - y_i)^2} \tag{2.4.4}$$

The relative absolute error (RAE) and the root relative squared error (RRSE) are expressed in percentile units and they actually assess the performance of the model when compared to the deviation of the predictions from the mean of the response ($\bar{y}$).

$$RAE = \frac{\sum_{i=1}^{n}|\hat{y}_i - y_i|}{\sum_{i=1}^{n}|\bar{y} - y_i|} \tag{2.4.5}$$

$$RRSE = \sqrt{\frac{\sum_{i=1}^{n}(\hat{y}_i - y_i)^2}{\sum_{i=1}^{n}(\bar{y} - y_i)^2}} \tag{2.4.6}$$

"I know one thing, and that is, that I know nothing."

-Socrates, Philosopher, 470–399 BC

3

Methodology

In the present chapter, an analytical description of the approach is made. The methodology description includes the CFD simulations and the data analysis parts.

In total, 61 flights of Ariane 5 are investigated, however due to the practical limitations, only 7 of them are computationally simulated.

3.1. CFD approach

In total, 7 flights are simulated. Since it is believed that liquid sloshing can lead to pressure fluctuations inside pressurized vessels, the purpose of the simulation is to highlight any differences in the kinematic behavior of the liquids that might exist on different flights. The aim would be to see whether high sloshing angles exist at the time of pressure rise/drop. If not, then sloshing could be ruled out as the cause of pressure rise/drop and further investigation should be required.

A summary of the simulated flights is presented in table Table 3.1.1

Table 3.1.1: Identified simulation flights with pressure behavior description.

Flight	LH_2 tank pressure	LO_x tank pressure
F009	Strong sudden drop	not simulated
F034	Average sudden drop	Strong rise
F042	Average gradual drop	Average rise
F050	Strong sudden drop	Strong rise
F052	Average gradual drop	Strong rise (late occurrence)
F053	No drop	Average rise
F060	not simulated	Strong rise

3.1.1. Model description and inputs

As already mentioned, in the upper stage compartment of the Ariane 5 launcher there are two liquid tanks (fuel and oxidizer). The schematic of the tanks is shown in Figure 1.3.1. At the bottom there is the LO_x tank, surrounded by the LH_2 tank. The two tanks can be regarded as one body however there were approached separately for the purpose of the present study.

Two different tank models were built using the post-processing capabilities of Flow3D. The 3D tank models are presented in Figure 3.1.1. In the same figure, the reader can see the history probe locations, which correspond to the location where useful simulation information are recorded and automatically output at post-processing. For the current case, the fill level is an important parameter which is recorded at the history probes location and it is later used for the calculation of the sloshing angle. A top view the history probe locations is shown in Figure 3.1.1. This figure corresponds to the LOx tank. The probe layout is identical for the LH_2 tank however, the probe radius (i.e. distance from the center) is doubled in order to correspond to the larger tank size.

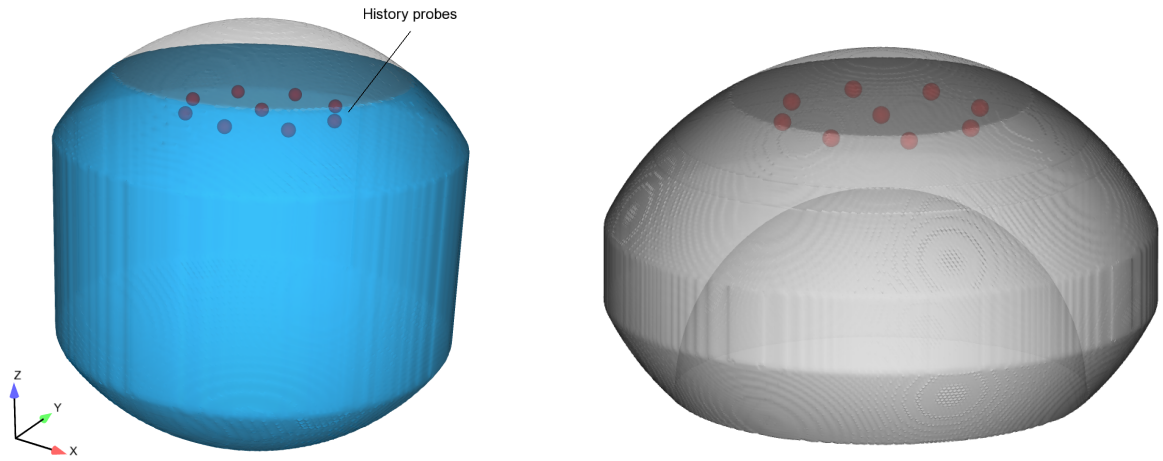

(a) 3D view of the LO_x tank.

(b) 3D view of the LH_2x tank.

Figure 3.1.1: The LO_x and the LH_2 tanks along with the corresponding location of the history probes used for the fill level recording.

Several assumptions are required in order to perform the CFD simulation. The simulation assumptions are highlighted below

- Only the kinematic behavior of the incompressible liquid is simulated, thus pressure and phase change are neglected
- Liquid properties (i.e. density, viscosity) are calculated based on the atmospheric saturation conditions.
- An 1-phase approach is performed. (Section 2.2)
- Surface tension is neglected due to the domination of gravitational forces. ($Bo \gg 1$)
- Internal tank equipment and damping system are not included in the geometry model.
- The fill level right before the launch is used as the simulation fill level.
- Tank compression and expansion is not taken into account during the simulation.

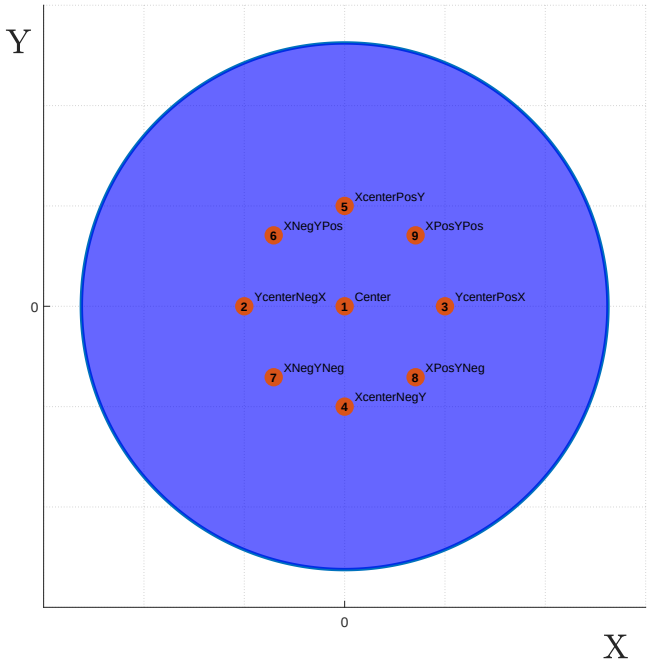

Figure 3.1.2: 2D top view of the LO_x tank (XY plane) including history probe location and labeling.

The kinematic profile of the launcher is used as an input for the CFD simulations. More specifically, the acceleration and the angular velocity of the launcher, as measured by the corresponding sensors, are used in order to simulate the fluid motion inside the tanks. A typical behavior of the kinematic profiles can be observed later on, in Figure 3.2.3 and Figure 3.2.4.

What should also be considered for the simulation is the importance of the center of gravity (CoG) of the launcher which is not constant. As the launcher ascends into the atmosphere, its CoG changes due to the continuous and massive fuel consumption that takes place. The CoG should move up higher over the launcher with time as more fuel is burned. It is also important to note that the launcher's CoG also changes with different payloads and tank fill conditions which makes it clear that it would slightly differ from flight to flight. A typical evolution of the launcher's CoG in z-direction is shown in Figure 3.3(a). The CoG does not significantly change in x- and y- direction, thus those changes were not considered for the simulation. To cope with the significant CoG change along the height of the launcher, the simulation was split into several sub-simulations with the re-adjusted CoG setting.

Finally, different fill levels were taken into account as the tank loading requirements are not constant. More specifically, for the LO_x tank the fill level can vary up to approximately $0.2m$, depending on the flight. For the LH_2, the fill level is kept constant as there is no great deviation in the measured fill height for the investigated flights. The fill level of the LO_x tank is calculated based on the loaded fuel mass and the tank geometry, and is directly taken from the available flight data. Similarly, the fill level of the LH_2 tank is based on the loaded mass and the tank geometry, however a constant value (average) is used for all the 7 flights.

The properties of the liquids were considered at saturation atmospheric conditions and are listed in Table 3.1.2.

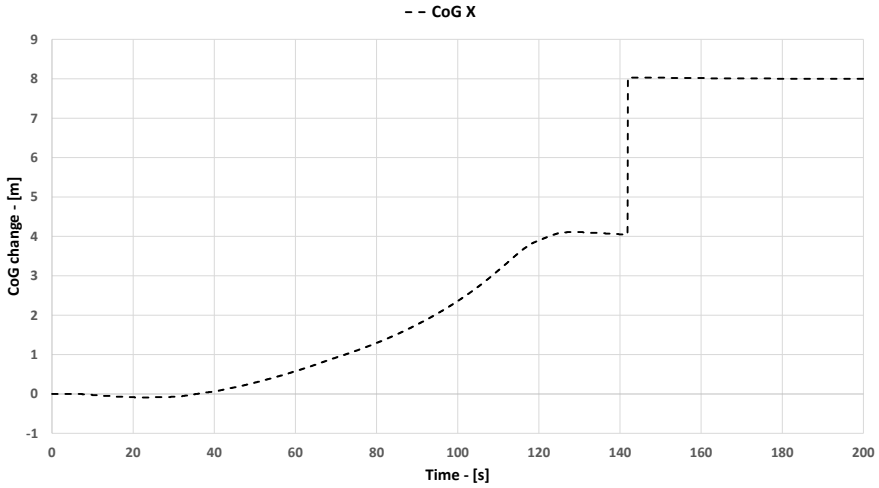

(a) Launcher CoG change in z-direction (height) during flight.

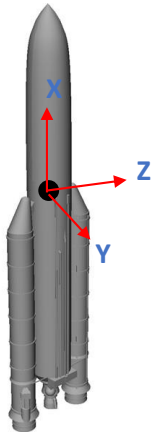

(b) Typical CoG location [3D CAD Browser, 2018]

Figure 3.1.3: CoG location and change during part of flight.

Table 3.1.2: CFD simulation liquid properties [Hanley et al., 1974; Van Itterbeek and Verbeke, 1960; J.Hord and H.M.Roder, 1981]

Quantity	LH_2 (20K 1bar)	LO_x (90K 1bar)
ρ $\frac{kg}{m^3}$	71.1	1140
μ $\frac{kg}{ms}$	1.34e-05	19.56e-05

3.1.2. Discretization and Simulation

The computational domain is 3-dimensional and a structured grid is used for the discretization of space. The grid consists of hexa-cells and has variable density. A finer grid is chosen near the free-surface which is of higher importance, while the grid becomes less dense near the tank bottom. To achieve this, 3 different mesh blocks are implemented. It is important to achieve gradual transition from the coarser to the finer grid in order to ensure high mesh quality. Additionally, the grid lines at the mesh block boarders should coincide in order to avoid excess computational time due to interpolation requirement at these regions. A 2-dimensional view of the grid of each tank is demonstrated in Figure 3.1.4.

In order to ensure that the measured quantity (in this case the sloshing angle) is independent to the mesh size i.e. does not significantly change with increasing cell number, a mesh independence study is performed. This will also ensure that accurate enough results will be reached in a reasonable computational time. The mesh independence study is based solely on the LO_x tank due to its smaller size, and does not span over the whole time period of interest but is limited to a smaller time period during the initial flight phase.

In total, 8 mesh density levels are produced. The finest one is used as the baseline. The liquid sloshing angle is used as a means of comparison. The mean deviation of each mesh level's angle from the finest one is calculated and plotted in Figure 3.1.5. The different mesh refinement levels are listed in Table 3.1.3 along with the minimum cell size, the total number of cells and the required computational time.

It can be seen that for meshes higher than 500 thousands cells, the mean angle deviation oscillates around 0.5 deg. It can be concluded that a mesh with a cell number of approx-

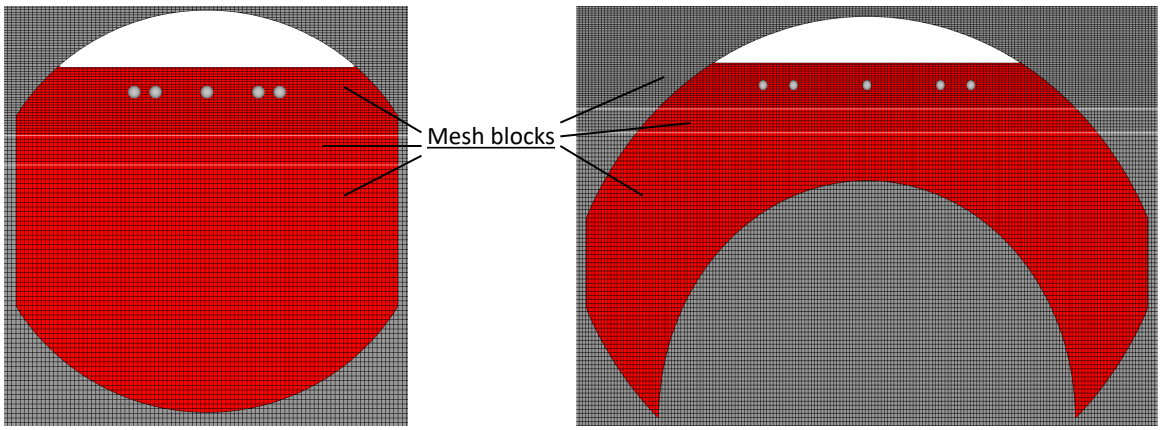

Figure 3.1.4: 2D side view of the grid lines of the LO_x and the LH_2 tanks.

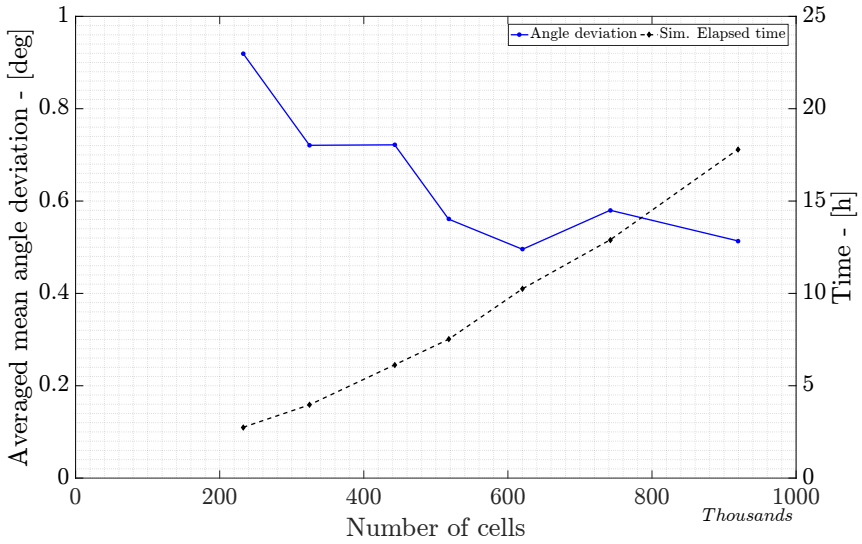

Figure 3.1.5: Mesh independence study of the LO_x tank

Table 3.1.3: Mesh refinement levels details

LO_x F050 mesh convergence study details								
	refinement levels							
	level 001	**level 002**	**level 003**	**level 004**	**level 005**	**level 006**	**level 007**	**level 008**
min. cell size [m]	~ 0.025							~0.013
# of cells	232584	324667	442828	517749	620284	741944	919385	1120227
elapsed time [h]	2.8	4.0	6.1	7.5	10.3	12.9	17.8	23.2

imately 620 thousands cells (refinement level 005) can lead to a relatively accurate result in a quite decent computational time of 10 hours, given the available hardware/software resources. The deviation of the sloshing angle for the chosen refinement level (level005) compared to the baseline mesh (level008) is demonstrated in Figure 3.1.6.

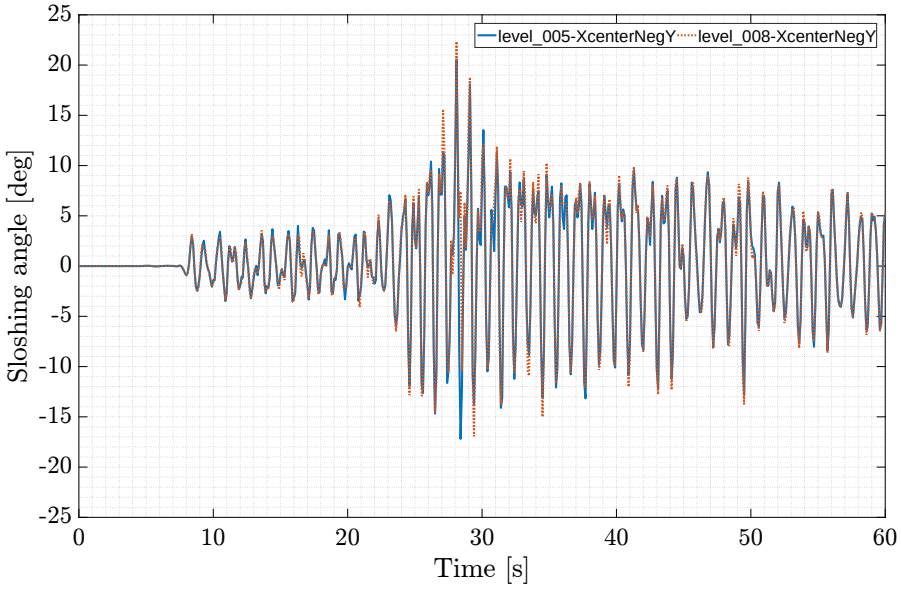

Figure 3.1.6: Sloshing angle evolution comparison of the chosen mesh density (level005) and the baseline mesh density (level008).

As it can be seen in Figure 3.1.6, the sloshing angle of level005 manages to decently follow the finer mesh level008, especially in the linear region (below $15deg$). Above this margin, chaotic/unstable sloshing occurs (i.e. breaking waves, splashing) and as a result a higher deviation of the two cases is noted. However, the results can still be regarded as satisfying as both cases manage to predict the high sloshing angles (angle magnitude higher than $20deg$) around the time period of $30s$.

For the LH_2 tank, the level005's minimum cell length could not be used as it led to a very high amount of mesh elements (exceeding 1.9 millions) and as a result massively increased the computational time. As a compromise, the less dense level004 is used in order to maintain the cell count below 1.55 millions and lead to a feasible computational time.

At this point, it should be noted that for both tanks a minimum cell size of approximately $0.02m$ is used. It is understood that this is still a relatively coarse mesh that might lead to some uncertainty in the results. However, the reader should keep in mind that the purpose of the simulation is not to accurately predict the exact sloshing angle inside the tank but to give a broader idea of the different sloshing angle magnitude that occurs in the investigated flights; and how is this related to the pressure change inside the tanks.

Regarding discretization of time, the automatically adjustable timestep feature of Flow3D is used. Using this feature it is ensured that during sloshing the timestep is maintained between $0.001s$ and $0.003s$ at most of the times. Given the limitation that exist (see Section 3.1.4) a non-fixed convergence criterion is used. Again, the convergence criterion is automatically chosen by Flow3D software which strives for a reasonable computational time and in the current cases choose a relatively "loose" convergence criterion. A typical timestep and convergence history are demonstrated in Figure 3.1.7 and Figure 3.1.8 for both tanks.

Despite the "loose" convergence approach, the simulation time is quite high. More specifically, to simulate a full LO_x flight ($200\,s$) approximately 3 full days are required while for the case of the LH_2 tank ($150\,s$) more than 6.5 days are needed.

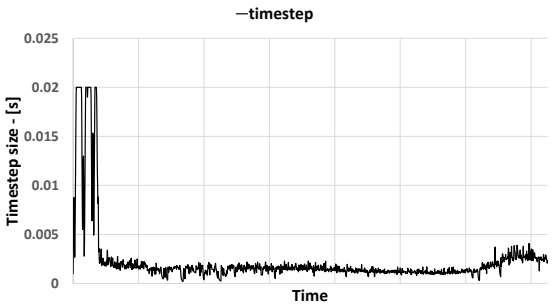

(a) Typical timestep evolution of the LH_2 tank simulation.

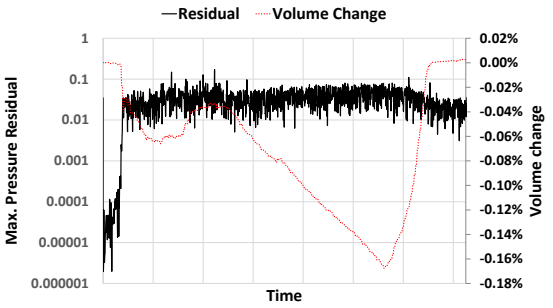

(b) Typical maximum pressure residual and volume error of the LH_2 tank simulation.

Figure 3.1.7: Typical LH_2 simulation diagnostics.

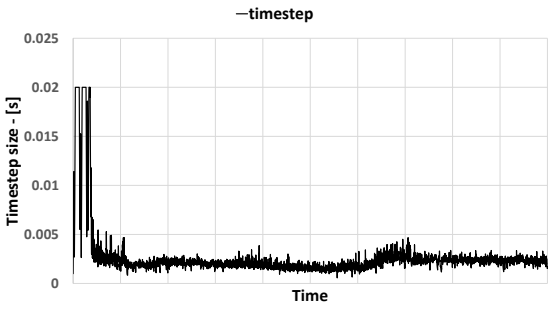

(a) Typical timestep evolution of the LO_x tank simulation.

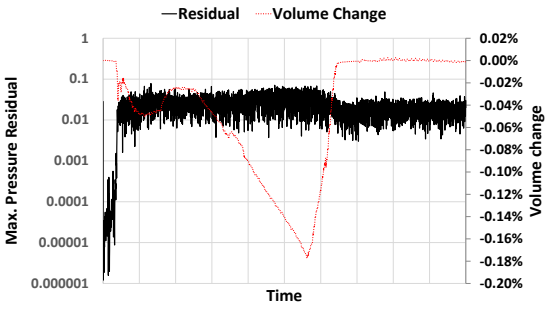

(b) Typical maximum pressure residual and volume error of the LO_x tank simulation.

Figure 3.1.8: Typical LO_x simulation diagnostics.

3.1.3. Sloshing angle

As already stated, the quantity of interest is the sloshing angle. The magnitude of the sloshing angle can indicate whether linear or unstable/chaotic sloshing can occur. The unstable sloshing, which occurs above $15\,deg$ [Montsarrat, 2017], can cause breaking waves and splashing. As a result, liquid droplets might be formed and reach the upper parts of the ullage or hit the tank walls, where the temperature is higher. This also implies that higher heat transfer is present since wave and droplet formation increase the surface area of the liquid. This can subsequently lead to evaporation or condensation depending on other parameters.

It has been already shown that sloshing and its magnitude can hold an important role in the pressure behavior inside a pressurized vessel. The sloshing magnitude can be directly related to the sloshing angle, which is defined in Figure 3.1.9.

For the present study, the sloshing angle is measured at the circumference of the tanks using the central history probe and the other 8 probes which are uniformly spread around the tank circumference. As a result, the sloshing angle can be calculated over the whole tank region and give a clear indication about the phenomenon. The sloshing angle can be simply calculated by using the fill heights at the locations of interest, as shown in Figure 3.1.9 and Equation (3.1.1).

$$\phi = arctan(\frac{h_C - h_A}{AB}) \tag{3.1.1}$$

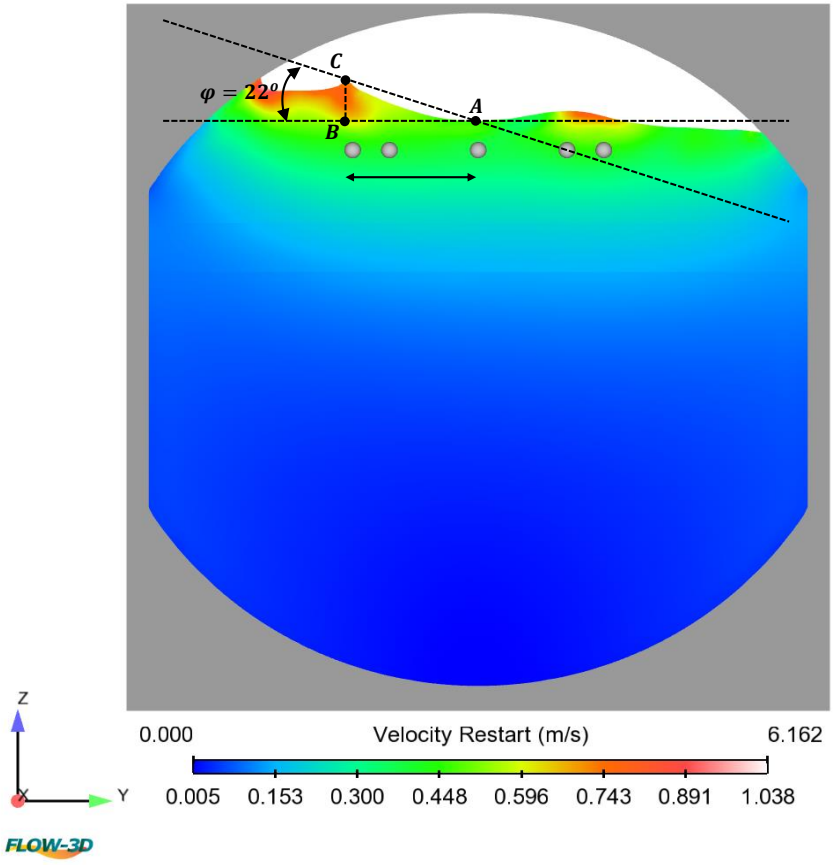

Figure 3.1.9: Sloshing angle definition and calculation

3.1.4. Limitations

Before assessing the results, it is important to take into account the practical limitations that existed during the project.

When dealing with simulations, one would normally strive for the maximum accuracy. Achieving a large number of cells, ensuring this way a sufficient minimum cell size, would be necessary for an accurate outcome. Additionally, since this is a transient simulation, restricting the time step and the convergence criterion to minimal values would be a requirement for satisfactory results.

However, what really confirms the accuracy of a simulation is the validation process, where the simulation outcome is compared to the actual one.

Such a comparison is only partially possible in our case, as only one level sensor is available per tank. Furthermore, the LO_x tank level sensor can not be used for validation purposes as it is centrally located, next to the Helium gas feeding tube which as already stated, is not included in the geometry model. As a result, only the LH_2 level sensor can provide valuable information regarding the simulation's accuracy.

Several phenomena that take place inside the tank, such as pressure and phase change, are neglected as it is chosen to limit the simulation to the kinematics only. This is a fact that also affects the accuracy of the outcome.

It was initially planned to extend the computational model beyond kinematics and include thermodynamic aspects as well i.e. heat transfer, phase change. However, this was not

possible as crucial hardware limitations existed.

The fact that only a single workstation was available for the project (4-core CPU @ 3.2 GHz) limited the computational capabilities. As a result, relatively coarse meshes were used for the simulation (min cell size approx. 0.02 m) aiming as well to a so called ”loose” convergence in order to minimize the required computational time. Despite the ”coarse” approach, high computational time was still required. That would be 3 days for a single simulation of LO_x and 6.5 days for a single simulation of LH_2. It is now understood that modeling the heat transfer and the other thermodynamic phenomena would require more sophisticated facilities and in turn would not be possible with the available equipment.

Furthermore, the thermodynamic approach of the phenomenon using Flow3D has already proved to be problematic due to software limitation, after the research of Van Foreest et al. [2011]; Van Foreest [2014], where they highlighted the deficiency of Flow3D in dealing with cryogenic sloshing including heat and mass transfer.

Despite the simplicity of the simulation, one can still extract valuable conclusions regarding the kinematic behavior of the liquid and relate it to the pressure fluctuations.

3.1.5. Validation

Due to the quite high number and importance of assumptions that were made in order to simulate the liquid sloshing motion, any validation attempt can not be realistic.

Neglecting the pressure and the phase change inside the tanks, the tanks' compression and expansion and the tanks' internal equipment, are some assumptions that affect the solution and in turn lead to a less realistic result. One should also take into account the insignificant but existing volume error that is caused due to ”loose” convergence approach.

To this limitation comes to add up the fact that only one fill level sensor is present in each tank. For the LO_x, this sensor is located in a central location, next to the GHe feeding tube that can be observed in Figure 1.3.1. The fact that the CFD model does not include this internal geometry, makes any attempt for validation impossible as the liquid's behavior should be completely different at this region.

For the case of the LH_2 tank, the fill level sensor is located close to one of the history probes that were used for the simulation. Again, it is hard to capture the exact evolution of the fill height due to the reasons that were mentioned above. However, the validation attempt showed that for this case, the CFD fill level behavior is identical to the one recorded by the sensor as seen in Figure 3.1.10.

It is believed that the deviation of the numerical approach after the $120\,s$, occurs due to the sudden acceleration drop and the already mentioned small volume error. However, this deviation is insignificant ($< 25\,mm$) and it occurs far from the period of interest which is early in flight.

It has been observed that this might be caused due to insufficient convergence near this region, as by tightening the convergence criterion this phenomenon was minimized. Unfortunately, this approach was not adopted, as it can significantly increase the computational time due to the limitations explained earlier in Section 3.1.4.

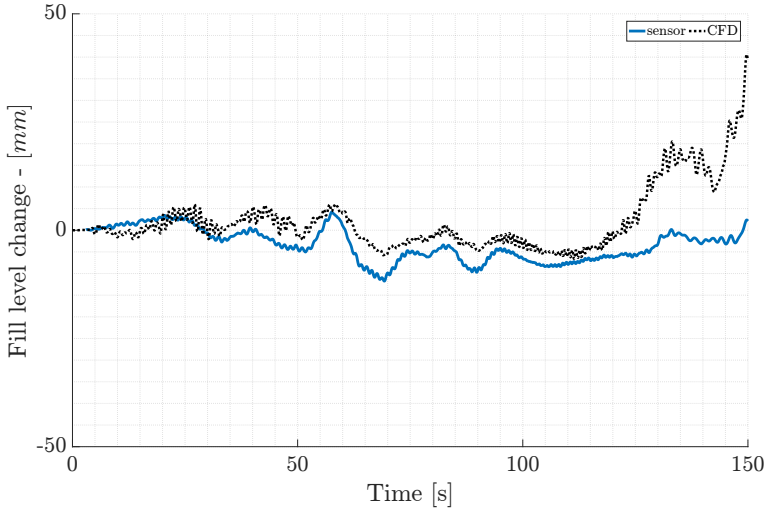

Figure 3.1.10: Fill level CFD results validation flight F053 - LH_2 tank

3.2. Data Analysis approach

In the present section, the approach of data analysis is presented. It is attempted to describe the steps that were followed related to data analysis. Information about the sensors that were used, the period of interest, the statistical and machine learning approach that was applied, is listed.

3.2.1. Selected parameters

The main source of data is the various sensors of the launcher. The majority of the data is available through the in-house data handling software ATLAS. Except from the flight sensors, some data is also collected from the available technical reports of Ariane 5. In total, 61 flights of Ariane 5 are investigated.

Through the conducted literature research, a set of parameters that hold an important role when it comes to liquid sloshing, have already been identified.

The study was focused on the ascent phase of the launcher where crucial parameters were investigated. Those are the pressure evolution, the acceleration and the roll rates of the launcher, the ullage volume and temperature and the vibrations (for LH_2 only). The concentration of helium at the ullage could be estimated by taking into account the ground phase pressurization time.

Pressure

Investigating the pressure behavior inside the tanks is of major importance in order to understand the possible reasons of the fluctuations. There are flights where no pressure change is recorded but there are also flights that show a strong drop or rise. The pressure rise/drop magnitude of the whole dataset is presented in Figure 3.2.1 for the LO_x and the LH_2 tank respectively.

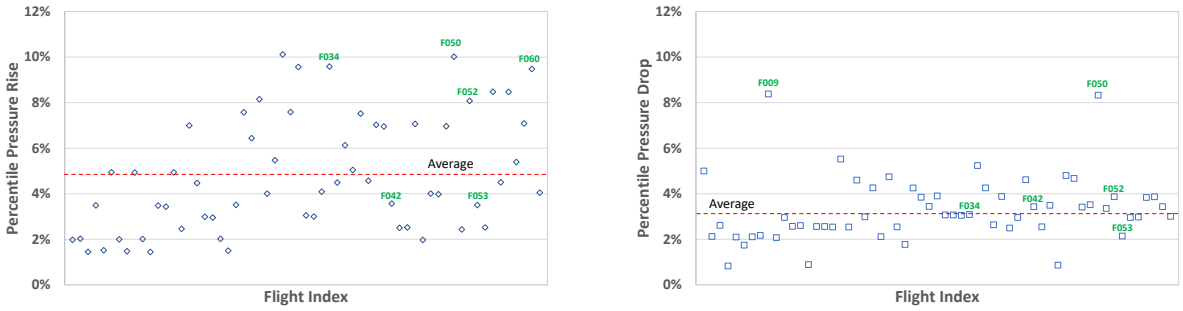

(a) Pressure rise magnitude of the LO_x tank.

(b) Pressure rise magnitude of the LH_2 tank.

Figure 3.2.1: Flight percentile pressure change magnitude.

The LO_x pressure appears to be more consistent. The highest pressure rise is around 10% of the initial pressure, and there are a couple of flights which demonstrated such a high pressure rise behavior. In the case of LH_2, the pressure drop magnitudes are "packed" around the average with the exception of 2 outliers, rising above 8% drop. The highlighted (in green) flights are those who were simulated and can be seen in Table 3.1.1 and Figure 1.3.3. The flight LH_2 F009 which is not shown, has an identical to F050 pressure behavior while the same holds for flight LO_x F060 which is similar to F034.

For the LO_x tank, normally there is a constant pressure period which extends up to the moment of the launch. This part is common to all of the flights. What is also similar to all flights is the gradual pressure rise located right after the maximum acceleration point, which is the point where the solid rocket boosters start to burn out. In some flights there is a small

pressure drop in the beginning. This is due to condensation that occurs early in flight. A possible explanation for this could be the increase of the partial pressure of the GO_x due to the sudden acceleration increase. Being heavier than the GHe, the GO_x will move closer to the free-surface (partial pressure increase) and will also experience a temperature drop as it comes closer to the cooler liquid. This situation favors the condensation phenomenon. In some flights, this pressure drop is not observable as when the pressure drops below the threshold, a quick readjustment is made by GHe injection. All the other pressure rises vary from flight to flight and it is believed that are influenced by the liquid sloshing.

The pressure behavior in the LH_2 tank is quite more stable. A small pressure drop might be noted in the beginning which is caused by the opening of the relief valve. Afterwards, mainly gradual pressure drops are noted and then the pressure rises again to the initial level. The pressure keeps rising continuously and the activation of the relief valve is necessary in order to maintain the pressure level below the upper threshold.

The definition of the pressure change magnitude is shown in Figure 3.2.2. For the LO_x tank, the pressure change is measured from the lowest pressure point up to the maximum one. For the LH_2 tank the pressure change magnitude is defined from the highest pressure point before the drop down to the lowest point after the drop. The pressure rise period that occurs after the drop is out of interest as we are mainly interested in the lowest possible level.

As mentioned in the introduction, it is important to restate, that both tanks initially experience a pressure drop (condensation), however this drop is less significant in the LO_x tank due to the lower amount of GO_x into the ullage.

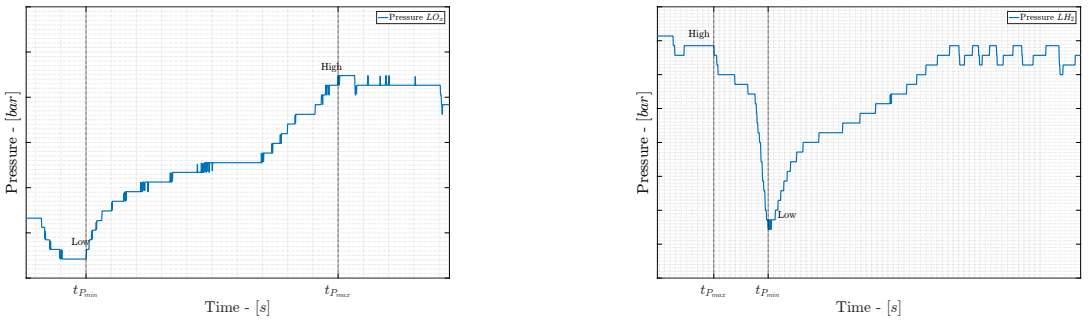

(a) Pressure rise calculation approach in LO_x ullage.

(b) Pressure drop calculation approach in LH_2 ullage.

Figure 3.2.2: Definition of the pressure change magnitude calculation in the two tanks.

The initial tank pressure (i.e. pressure at H_0) as well as the pressure right before the rise/drop and the time period at which it occurs are also parameters that could affect the pressure change magnitude, and thus are included in the study.

Acceleration and Roll rates

There are many parameters that might affect the magnitude of pressure change however it is believed that this is mainly caused by liquid sloshing. The kinematic profile of the launcher will directly affect the liquid's behavior inside the moving containers. As a result, the acceleration and the roll rate profile of the launcher is analyzed. The typical evolution of the acceleration and roll rates is shown in Figure 3.2.3 and Figure 3.2.4 for x,y,z axis.

The liquid sloshing can mainly be affected by sudden changes in the kinematics of the launcher. These sudden changes will be the criteria of assessing the effect of the acceleration and roll over the pressure change.

To evaluate the effect of the acceleration and roll, only their sudden magnitude change is taken into account. This is done with a simple MATLAB routine which initially finds the minimas/maximas of the kinematic profile and then accumulates only the steep changes into a

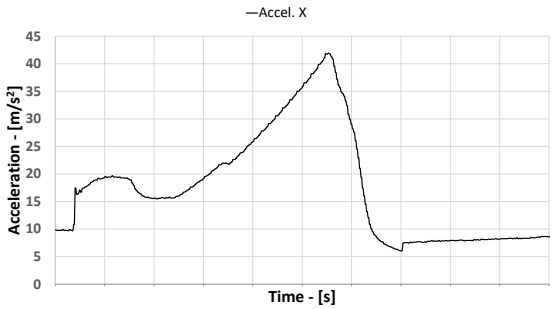

Figure 3.2.3: Typical acceleration profile of launcher in -x direction. [Arianespace, 2016]

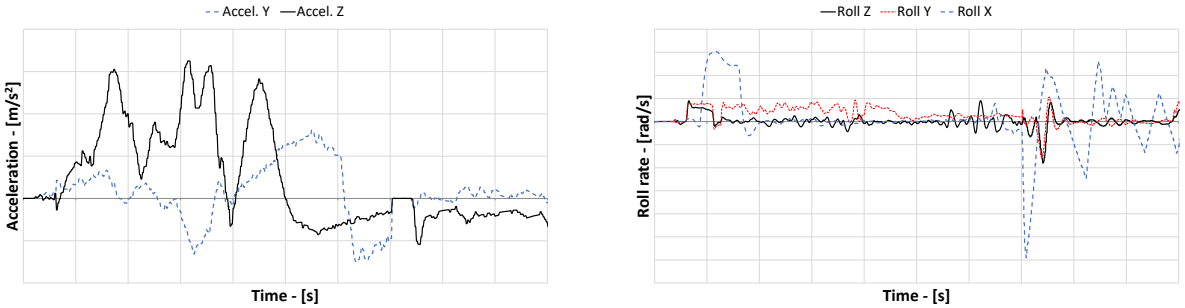

(a) Launchers typical translational accelerations of -y and -z axis

(b) Launchers typical roll rates of -x, -y and -z axis

Figure 3.2.4: Launchers typical kinematic profile including acceleration and roll rates.

single acceleration/roll change magnitude. An example of the identified minimas/maximas is shown in Figure 3.2.5 for both tanks. This method is applied for all the kinematic components and its combinations in order to find the ones that show the strongest correlation to the pressure change magnitude.

The overall (sudden) change magnitude of acceleration and roll is measured over a predefined time period. This time period is a function of the pressure rise point, the pressure stabilization point and the finite time periods d_1, d_2 and d_3 as shown in Figure 3.2.5. It is believed that the effect of sloshing over pressure is in a way delayed i.e. the pressure rise will occur a bit after the sloshing has began. Thus, the values of d_1, d_2 and d_3 should be determined through an optimization routine in order to find the time period, i.e. the area of interest, that shows the strongest correlation between the kinematics and the pressure change.

The optimization results for the LO_x and the LH_2 tanks are presented in Figure 3.2.6 and Figure 3.2.7 respectively. It is shown that for the LO_x tank strong correlation of the kinematic profile to the pressure rise exists ($R^2 > 0.55$) for $d_1 = d_3 \approx 20$ for the acceleration and $d_1 \approx 30$, $d_3 \approx 40$ for the roll rates.

The situation is not similar for the LH_2 tank as the optimization showed no clear region of strong correlation. The strongest correlation is slightly higher than $R^2 > 0.22$ which is indeed an indication that the pressure drop of the tank is not related to the kinematic profile of the launcher. The regions with the highest correlation coefficient are the $d_1 \approx 5$, $d_3 \approx 35$ for the acceleration and the $d_2 \approx 15$, $d_3 \approx 45$ for the roll rates.

A preliminary analysis showed that there is no strong correlation between the individual acceleration profiles of x,y and z. First of all, acceleration in -z is identical to all of the flights, so it should be excluded from the analysis. The individual accelerations on -x and -y also showed no strong correlation. However, combining the -x and -y acceleration magnitudes

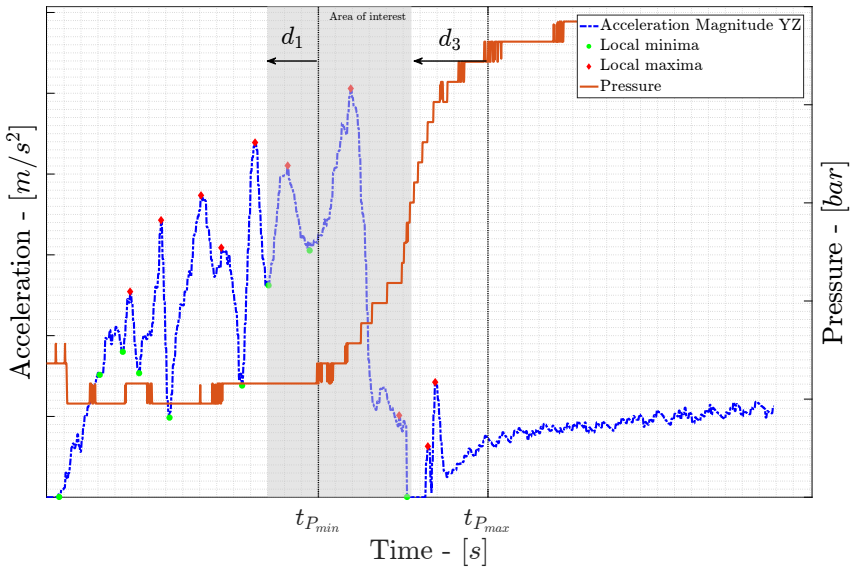

(a) LO_x tank approach.

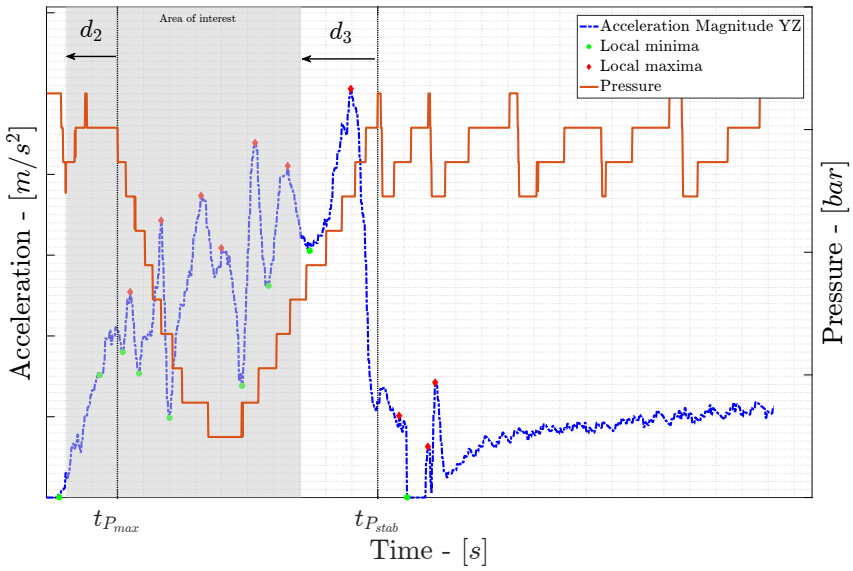

(b) LH_2 tank approach.

Figure 3.2.5: Definition of the area of interest for the calculation method of the acceleration fluctuations.

into a single one (i.e. -xy magnitude) and applying the above mentioned process, led to a strong correlation. An identical process is followed for the roll rates profile as well, in order to obtain the components having a great impact on the pressure change magnitude.

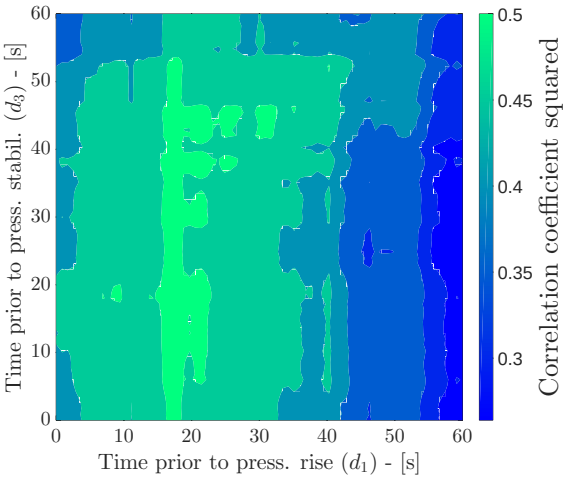

(a) Correlation of acceleration

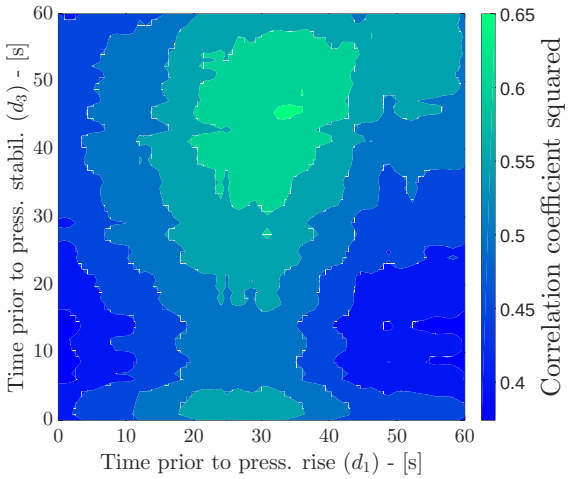

(b) Correlation of roll rates

Figure 3.2.6: Correlation strength with respect to the considered time period of the acceleration and roll rate profiles for the LO_x tank pressure rise magnitude.

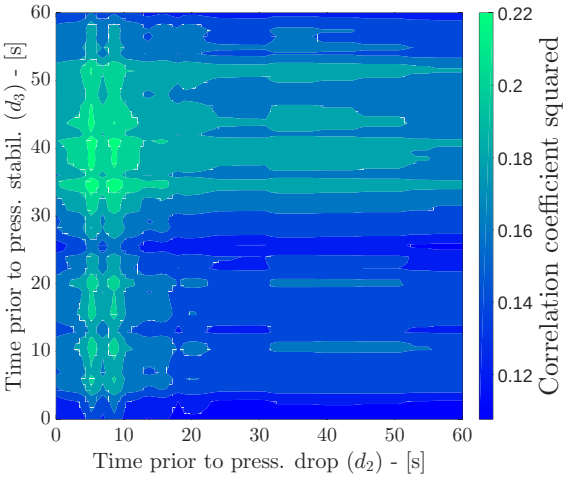

(a) Correlation of acceleration

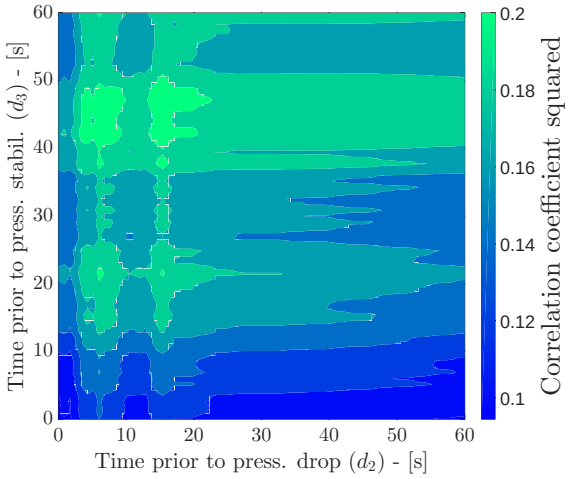

(b) Correlation of roll rates

Figure 3.2.7: Correlation strength with respect to the considered time period of the acceleration and roll rate profiles for the LH_2 tank pressure drop magnitude.

Ullage volume

The ullage volume is the amount of the tank's volume which is empty i.e. not filled by the propellants. As it was found by the literature, the ullage volume can affect the magnitude of pressure drop/rise during sloshing. Other parameters that are also related to the ullage volume is the helium concentration, the pressurization time and the ullage temperature; all of which are identified as having a possible effect on the pressure change.

For the LH_2 tank this quantity is almost constant, as the loaded amount of liquid hydrogen is almost identical to all the flights. The loaded mass of liquid oxygen changes depending on the payload, launch conditions and other parameters. The resulting ullage volume per loaded liquid oxygen mass is derived from the tank's and the liquid's volume.

Temperature

The temperature sensor of both tanks are located on top of the dome. Thus, it is quite difficult to have a clear overview of the temperature profile with respect to the tank height. Due to its location, the temperature sensor can only capture possible temperature drops as a result of fuel jettison onto the higher parts of the tank's ullage.

A typical temperature profile of the LO_x tank is demonstrated in Figure 3.2.8 for one high and one low pressure rise flight. Typically, the temperature will experience a small rise right after launch. This is caused by a small helium injection which takes place in the beginning of the flight. This is not consistent to all of the flights and will only be activated when the pressure, due to condensation, drops below a threshold. The impact on the temperature is immediate as the temperature sensor is located right at the helium inlet. This pressure drop happens due to the already explained increase of the partial pressure of GO_x

Such a flight is flight F053 where the notable temperature increase can be spotted right at the beginning of Figure 3.2.8 (a). The temperature then gradually decays due to the heat transfer within the system. There is no significant pressure rise in this flight; this might be an indication of low amplitude sloshing.

The situation is slightly different when looking at a flight with a higher pressure rise (Figure 3.2.8 (b)). Initially a pressure drop is noticed (sign of condensation), however in this case no helium injection takes place. Probably the pressure did not drop below the threshold so that the re-pressurization mechanism to be activated. Then, the pressure rises again which could be possibly be affected by sloshing, and so the temperature drops, to a lower level than the previous flight. Again, we should keep in mind that the effect of sloshing on the temperature can not be directly observed due to the sensor location (at the top of the tank).

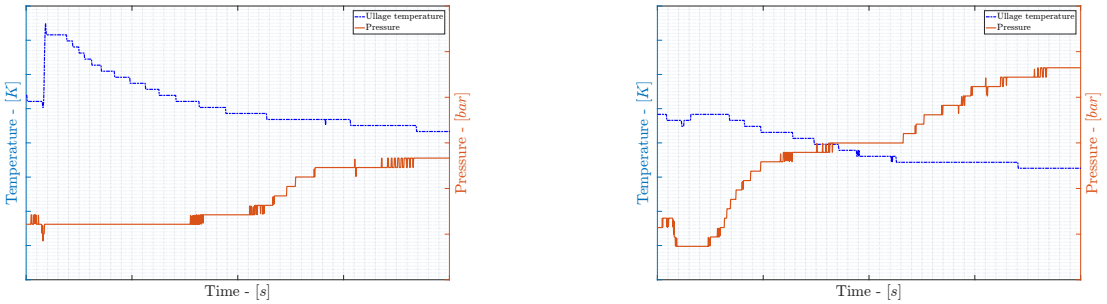

(a) Temperature and pressure of F053 - LO_x tank.

(b) Temperature and pressure of F050 - LO_x tank.

Figure 3.2.8: Typical pressure behavior of high/low pressure rise flights - LO_x tank.

In Figure 3.2.9, the typical LH_2 tank temperature profile of a high pressure drop and a no pressure drop flight is demonstrated. Looking at flight F053 (Figure 3.2.9 (a)), where no

pressure drop occurs, we can see that the temperature maintains a gradual rise throughout the launcher's ascent phase. As no pressure drop is noticed, it is believed that sloshing magnitude is relatively low. As a result, the temperature inside the ullage rises at a smooth rate due to the temperature difference between helium and hydrogen. The sudden small drop at the beginning happens because of a small de-pressurization that takes place right before the launch.

On the other hand, F009 (Figure 3.2.9 (b)) is a flight with a high pressure drop. It is believed that this high pressure drop is enhanced by the high amplitude sloshing/breaking waves that are present. As a result, the cool liquid reaches the higher parts of the tank and cools down the ullage. This approach can be directly depicted at the temperature behavior of flight F009. It can be seen that right before the pressure drop, the temperature experiences a sudden drop, indication that the liquid has reached the region of the temperature sensor.

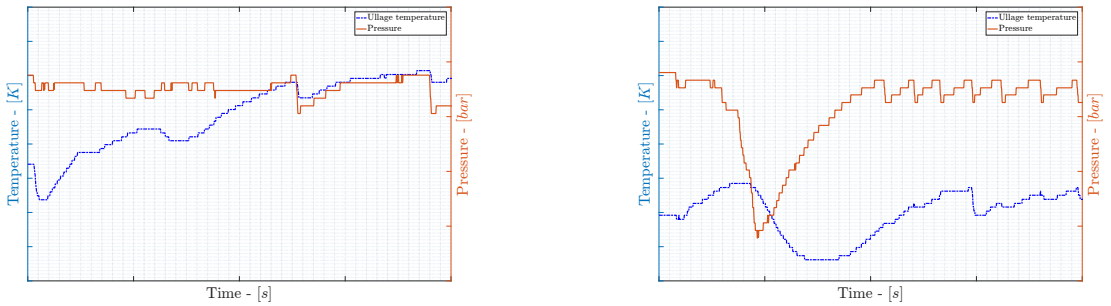

(a) Temperature and pressure of F053 - LH_2 tank.

(b) Temperature and pressure of F009 - LH_2 tank.

Figure 3.2.9: Typical pressure behavior of high/no pressure drop flights - LH_2 tank.

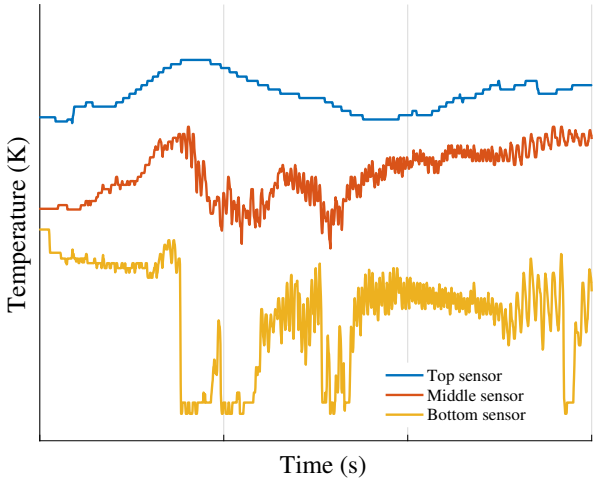

Figure 3.2.10: Temperature profile in 3 different locations during pressure drop of F001 - LH_2 tank. [Montsarrat, 2017]

It was shown that the temperature sensor can provide valuable information regarding the presence of liquid at the higher parts of the ullage. However, this can not be feasible for all the flights. As it was previously mentioned, there is only one temperature sensor in each tank which is located at a very specific location near the top region. This can not guarantee that the liquid presence will be captured at all times as there might be cases that the sloshing is not so intense, leading to smaller waves etc. To demonstrate this, flight F001 was equipped with 3 sensors spread inside the LH_2 tank. In Figure 3.2.10, it can be seen that the temperature

inside the tank depends on the sensor location and it is lower as we get closer to the liquid's surface. Additionally, at the moment of pressure drop where sloshing is expected to occur, the temperature at the top sensor remains unaffected while the one at the bottom records a sudden drop.

It can be now understood that the measurements of the existing temperature sensor can not be directly related to the pressure drop due to the above mentioned limitation. However, it is of great interest to study the initial and the maximum temperature that is recorded inside the tanks with respect to the pressure change magnitude.

Vibrations

As described in Section 2.3, the frequency and amplitude of the excitation can have an impact over the pressure change magnitude. This is maximized when the tank is excited near its natural frequency. Using Equation (2.3.1) one can approximate the natural frequency of the systems. For the LH_2 tank, however, the natural frequency is given by the designer. Near the time of the pressure drop the acceleration varies from $15m/s^2$ to $20m/s^2$, as a result an approximation of the natural frequency is taken as $f_n \approx 0.8Hz$. It should be mentioned that Equation (2.3.1) fits well to the designer values for $\sqrt{\lambda} = 2.07$.

A preliminary analysis of the frequency spectrum of the acceleration and the roll rates showed that no dominating frequencies near $0.8Hz$ exist. What is now left, is to investigate the measurement of the vibration sensors which are located in the tanks. This approach is only possible for the LH_2 tank as only there, there are vibration sensors measuring the vibrations of acceleration on -y and -z axis. Again the vibrations of -y and -z are combined into a single -yz vibration magnitude.In general, the time period near the pressure drop is examined using the MATLAB *fft()* function, but 2-dimensional spectrograms are also created to examine the frequency evolution over the whole ascent phase.

Vibrations are not included in the CFD simulation however they can be used as a supplementary source of information to explain the pressure change inside the tanks. The approach by Stofan et al. [1962] that was presented in Section 2.3 can provide evidence about possible sloshing occurrence. It should be mentioned that due to the fact the vibration sensors provide the vibration of acceleration, its magnitude should be converted to displacement by implementing Equation (3.2.1) and converted to inches in order to be in line with Stofan's approach.

$$x_A = \frac{a_A}{2(\pi f)^2} \tag{3.2.1}$$

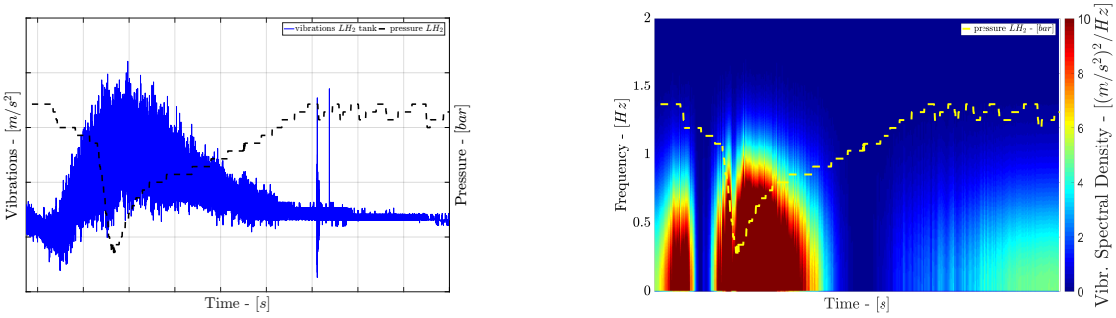

(a) Vibration signal (YZ magnitude) at the upper dome of the LH_2 tank and LH_2 ullage pressure vs Time.

(b) Vibration's spectrogram

Figure 3.2.11: Vibration profile and pressure drop of the LH_2 tank of F050.

An example of the vibration signal and the its corresponding spectrogram with the power spectral density estimate, is presented in Figure 3.2.11. It appears that the vibration profile

is of great interest as at first sight, the amplitude shows a notable increase near the pressure drop region. There are also dominating frequencies between $0\,Hz$ and $1\,Hz$, which could probably explain the pressure drop phenomenon.

Pressurization time

The pressurization time has been identified by several researchers as an important parameter that affects the pressure change during sloshing. The pressurization duration depends on the type of the liquid, as already described and showed in Figure 1.3.2 of Chapter 1. The ground pressurization phase is identical for most of flights showing only slight changes with respect to the exact pressurization duration.

By assuming that the pressurant's gas (GHe) mass flow is constant, and taking into account the ullage volume of each flight, then a rough estimation of the ullage helium concentration can be made and expressed via the ratio of Equation (3.2.2)

$$C_{GHe} \sim \frac{t_{press,tot}}{U_{ullage}} \tag{3.2.2}$$

It is understood that this is not the exact helium concentration, as the helium mass flow rate is unknown; it is however a metric that can be used instead, to investigate a possible correlation to the pressure change.

3.2.2. Statistical Model

The parameters mentioned above can be now used to create a statistical model for the prediction of the pressure change based on Section 2.4. The magnitude of pressure will now be the response variable and all the other identified variables will be the predictors. The predictors can be observed in Table 3.2.1

Table 3.2.1: The variables used as predictors for the linear model construction

Parameter	Explanation
$t_{P_{min}}$	The time after launch at which the pressure rise occurs - LO_x tank
$t_{P_{max}}$	The time after launch at which the pressure drop occurs - LH_2 tank
p_{init}	The initial tank pressure at H_o - both tanks
T_{max}	The maximum ullage temperature - both tanks.
T_{init}	The initial ullage temperature - both tanks.
ΔT_{drop}	The total ullage temperature drop recorded during flight - both tanks.
U_{ullage}	The ullage vollume - LO_x tank
C_{GHe}	The estimate of helium concentration in the ullage - LO_x tank
$Accel_{-x-y-z-yz}$	The total acceleration components magnitude change during the rise/drop - both tanks
$Roll_{-x-y-z}$	The total roll rates components magnitude change during the rise/drop - both tanks

A preliminary step is to examine the correlation of the predictors/response set, between each other. In this way the most crucial parameters, the ones that show the strongest correlation to the response are identified. This is also useful to obtain possible collinearities between the predictors. When colinearities exist, it is recommended to exclude the excess predictors from the set and only keep one of the colinear predictors. The correlation matrix for the LO_x is presented in Table 3.2.2.

What is of great importance, is the last row of Table 3.2.2 where the relationship of the various parameters with the pressure drop can be retrieved. The parameters with the strongest correlation are the roll change over -y axis, the acceleration change over -yz, the pressure rise time spot, the ullage volume, the maximum temperature and the temperature drop. It appears that the initial tank pressure as well as the initial temperature, does not affect the magnitude of the pressure change.

Table 3.2.2: Correlation matrix of the LO_x tank pressure rise

Parameters	p_{init}	$t_{P_{min}}$	U_{ullage}	$Accel_{-yz}$	$Roll_{-y}$	T_{init}	T_{max}	ΔT_{drop}	C_{GHe}	Δp
p_{init}	1	⋮	⋮	⋮	⋮	⋮	⋮	⋮	⋮	⋮
$t_{P_{min}}$	−0.182	1	⋮	⋮	⋮	⋮	⋮	⋮	⋮	⋮
U_{ullage}	−0.012	0.504	1	⋮	⋮	⋮	⋮	⋮	⋮	⋮
$Accel_{-yz}$	0.059	−0.896	−0.471	1	⋮	⋮	⋮	⋮	⋮	⋮
$Roll_{-y}$	0.004	−0.726	−0.653	0.770	1	⋮	⋮	⋮	⋮	⋮
T_{init}	0.162	0.388	0.780	−0.347	−0.366	1	⋮	⋮	⋮	⋮
T_{max}	0.060	0.447	0.855	−0.430	−0.520	0.618	1	⋮	⋮	⋮
ΔT_{drop}	−0.118	0.609	0.696	−0.576	−0.568	0.468	0.821	1	⋮	⋮
C_{GHe}	−0.045	−0.402	−0.844	0.378	0.616	−0.607	−0.762	−0.632	1	⋮
Δp	−0.056	−0.664	−0.552	0.735	0.813	−0.388	−0.509	−0.520	0.554	1

As already explained in the previous sections, the temperature change is in general not reliable due to the insufficient number and location of the temperature sensor. As a consequence it is better to be excluded from the model. Furthermore, the ullage volume and the maximum temperature appear to have an identical effect on the pressure drop. In addition to this, it appears that these two variables are collinear as their correlation coefficient is high (0.855). This implies that the higher the ullage volume the higher the maximum temperature of the ullage will be; it is indeed true, as a higher ullage volume would require more helium to achieve the same pressurization level, thus the temperature would reach higher levels (due to the already high temperature of helium). As collinearity exist, only one of the two parameters should be kept and this would be the ullage volume as it shows a slightly higher absolute correlation coefficient. The same hold for the helium concentration which is directly related to the ullage volume and should also be excluded.

The moment of pressure rise ($t_{P_{min}}$) should also be removed from the model. It is shown that the earlier the pressure rise occurs, the higher the pressure rise will be. However, it is believed that sloshing is the main reason of pressure change and it is the phenomenon that onsets the pressure change. In other words, the kinematic profile of the launcher, which is directly responsible for the sloshing, would dictate when the pressure rise will take place. This can be confirmed by the high collinearity that exists between the $t_{P_{min}}$ and the acceleration and roll change as well.

It can be concluded that the only appropriate parameters for the construction of the prediction model of the LO_x tank pressure rise are the $Accel_{-yz}$, $Roll_{-y}$ and the U_{ullage}. This will be a 3x1 MLR model. Before concluding to this model, it is important to investigate the other linear models that can be built through the combination of these 3 predictors.

When it comes to the LH_2 tank pressure drop, the situation is not encouraging. As it can be seen from Table 3.2.3 there are no clear signs of strong correlation between the predictors and the response.

Table 3.2.3: Correlation matrix of the LH_2 tank pressure drop

Parameters	p_{init}	$t_{P_{max}}$	$Accel_{-yz}$	$Roll_{-y}$	T_{init}	T_{max}	ΔT_{drop}	Δp
p_{init}	1	⋮	⋮	⋮	⋮	⋮	⋮	⋮
$t_{P_{max}}$	0.127	1	⋮	⋮	⋮	⋮	⋮	⋮
$Accel_{-yz}$	−0.119	−0.342	1	⋮	⋮	⋮	⋮	⋮
$Roll_{-y}$	0.027	−0.396	0.849	1	⋮	⋮	⋮	⋮
T_{init}	0.134	0.214	−0.214	−0.272	1	⋮	⋮	⋮
T_{max}	−0.112	0.041	0.332	0.320	0.488	1	⋮	⋮
ΔT_{drop}	0.218	0.033	−0.108	−0.077	−0.058	−0.522	1	⋮
Δp	0.031	−0.138	0.491	0.462	−0.223	−0.261	0.688	1

The kinematic profile is now less influential as the correlation coefficients of the acceleration and the roll are below 0.5. The initial tank pressure, the pressure drop time, the initial and the maximum temperature also show a rather weak correlation to the overall pressure change.

What is now left is the temperature drop ΔT_{drop} which shows the strongest correlation. However, due to the already known limitations of the temperature sensors, only 8 flights showed an actual temperature drop at the region before the pressure drop. Those are F001, F005, F009, F018, F024, F037, F038 and F050. Restricting the correlation analysis to these 8 flights leads to the new Table 3.2.4.

Table 3.2.4: Correlation matrix of the LH_2 tank pressure drop of the 8 temperature drop flights

Parameters	p_{init}	$t_{P_{max}}$	$Accel_{-yz}$	$Roll_{-y}$	T_{init}	T_{max}	ΔT_{drop}	Δp
p_{init}	1	⋮	⋮	⋮	⋮	⋮	⋮	⋮
$t_{P_{max}}$	0.686	1	⋮	⋮	⋮	⋮	⋮	⋮
$Accel_{-yz}$	−0.346	−0.388	1	⋮	⋮	⋮	⋮	⋮
$Roll_{-y}$	0.191	−0.110	0.707	1	⋮	⋮	⋮	⋮
T_{init}	−0.702	−0.682	0.103	−0.264	1	⋮	⋮	⋮
T_{max}	−0.819	−0.606	0.317	−0.245	0.765	1	⋮	⋮
ΔT_{drop}	0.738	0.294	−0.116	0.384	−0.293	−0.776	1	⋮
Δp	0.355	−0.097	0.305	0.652	−0.137	−0.567	0.831	1

The new correlation table, which is restricted to 8 flights only, shows different results. In this approach, the temperature drop shows a stronger correlation to the pressure drop. This is an indication that cold liquid has reached the higher parts of the ullage leading to condensation/evaporation effects. This is enhanced by the fact that for these 8 flights the correlation of the roll rate is now higher, reaching 0.652. It appears that for these 8 flights the pressure drop could be indeed caused by sloshing however the small amount of inputs does not allow us to use this approach in order to build a prediction model.

What is also interesting to point out, is the fact that 5 out of 8 temperature drop flights (the ones with the highest temperature drop) show a sudden and steep pressure drop while compared to the rest of the dataset (identical to F050 of Figure 1.3.3 (a)). These 5 flights also happen to be the outliers of the first correlation attempt of the kinematic profile based on the full dataset. Recall the low correlation coefficients of acceleration and roll rate magnitude change of Table 3.2.3. By removing these 5 flights from the original dataset, the correlation coefficient of acceleration and roll rate magnitude change to the pressure drop magnitude significantly rise to $R = 0.802$ and $R = 0.735$ respectively. This is a clear indication that the pressure drop of these 5 flights is not only driven from the sudden change of acceleration and roll but probably there is another parameter that affects it.

It can be concluded that for the LH_2 tank no safe approach can be made in order to build a reliable prediction model for the pressure drop magnitude. The investigation of correlation led to poor correlation coefficients, while restricting the dataset to the above mentioned 8 temperature drop flights does not provide a sufficient number of instances to rely a prediction model on. Finally, not taking into account the 5 outliers, increases the correlation coefficients in the first place however, it is these 5 flights that show the largest drop, thus it would make no benefit to build a prediction model for the pressure drop, excluding those. Hence, he linear statistical model prediction will only be applied to the LO_x tank.

The model can be easily built using MATLAB's statistical toolbox or other open-source software. The model was built using the open-source software WEKA [UniversityOfWaikato, 2017] which is developed and maintained by the Machine Learning Group of the University of Waikato, New Zealand. This software was prefered because it offers machine learning validation capabilities. The multiple linear regression (MLR) approach is based on the theory of Section 2.4.

This is an MLR model with 3 independent variables ($Accel_{-yz}$, $Roll_{-y}$ and the U_{ullage}) and the response (Δp). The resulting full linear model would be similar to Equation (2.4.1) and in this particular case will be as follows

$$\Delta p = \beta_0 + \beta_1 Accel_{-yz} + \beta_2 Roll_{-y} + \beta_3 U_{ullage} \tag{3.2.3}$$

However, as mentioned, it is important to investigate all the possible models resulting from the combination of the predictors. The models can be validated with the leave-one-out cross validation method and in this way conclude which one fits best. It is important to validate the model with ”fresh” data, that is, data that were not previously used for the model construction. The dataset consists of 61 instances and is split into 61 different groups in order to create the training and the test sets. In the leave-one-out method, 1 instance is left out in order to be used for testing the statistical model built by the training set consisting of the rest 60 instances. This process is repeated 61 times and then, the results are averaged in order to produce a single estimation. The same process is done for each of the 7 models that are tested. A summary of all the 7 tested models is presented in Table 3.2.5

Table 3.2.5: Statistical models comparison

Model	$\boldsymbol{Accel_{-yz}}$	$\boldsymbol{Roll_{-y}}$	$\boldsymbol{U_{ullage}}$	F-statistic	p-value	R^2	St.Error	CV R	CV MAE
Model 1	x	-	-	69.38	< 0.01	0.54	0.0358	0.711	0.0279
Model 2	-	x	-	108.11	< 0.01	0.65	0.0314	0.789	0.0245
Model 3	-	-	x	25.79	< 0.01	0.30	0.0441	0.505	0.0372
Model 4	x	x	-	61.55	< 0.01	0.68	0.0302	0.802	0.0228
Model 5	x	-	x	42.55	< 0.01	0.59	0.0340	0.740	0.0269
Model 6	-	x	x	53.43	< 0.01	0.65	0.0316	0.782	0.0248
Model 7	x	x	x	40.74	< 0.01	0.68	0.0303	0.797	0.0230

It can be seen that model 4 and 7 show the highest CV R and the lowest CV MAE. Despite model’s 4 metrics are slightly better, this model is not chosen as it only includes the effect of acceleration and roll rates in its prediction. Instead, model 7 includes all the variables. It is preferred to include the ullage volume as this is an important parameters that is always known beforehand (i.e. known before the launch). As a result, this model would be more practical in order to assist future predictions of the pressure rise.

The actual vs the predicted outcome of the cross-validation process is presented in Figure 3.2.12 along with the error measures of Weka in Table 3.2.6 as explained in Section 2.4

Table 3.2.6: Cross validation summary as explained in Section 2.4

Measure	**Value**
Correlation coefficient	0.7973
Mean absolute error (MAE)	0.023
Root mean squared error (RMSE)	0.0314
Relative absolute error (RAE)	51.06%
Root relative squared error (RRSE)	59.44%

The statistical model’s evaluation has a promising outcome as the error metrics are low and the correlation coefficient is approximately equal to 0.8. This means, as it can also be seen in Figure 3.2.12, that the predicted values lie close to the actual ones (except from some outliers). The model can now be used to estimate the minimum/maximum pressure rise inside the LO_x tank.

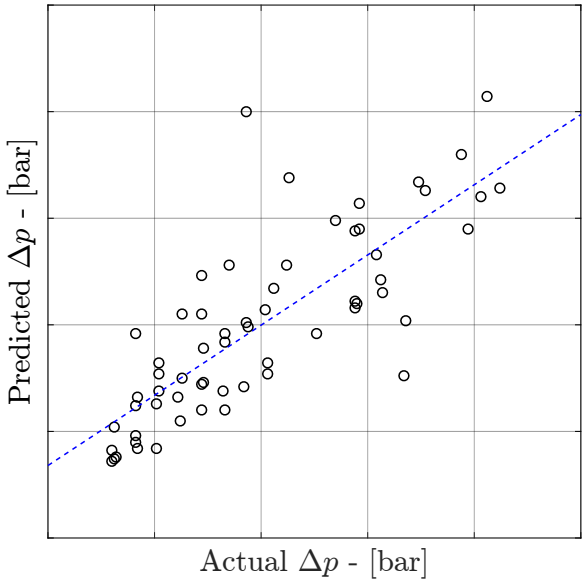

Figure 3.2.12: Actual vs Predicted LO_x tank pressure rise

"There is nothing permanent than change"

-Heraclitus, Philosopher, 535–475 BC

4

Results

In the present chapter a detailed presentation of the results is listed. The results are the outcome of the CFD simulations and the data analysis approach which were already described in the previous sections.

4.1. CFD Sloshing

The results of the CFD simulations are now presented. The presentation is split into two parts, the LO_x tank and the LH_2 tank respectively. The sloshing angle and the breaking waves that were observed are being related to the ullage pressure drop/rise of the tanks. There are 6 LO_x and 6 LH_2 cases in total. Recall Table 3.1.1 of the simulated flights presentation indicating the magnitude of pressure change of each flight. The results are supplemented by several data plots (i.e. temperature) that can help in explaining the pressure change.

The sloshing angle was calculated around the tank at 8 different locations, such that it can capture the liquid's behavior along $360\,deg$. A detailed summary of the CFD sloshing angle results is listed in the appendix Chapter A where the sloshing angle evolution over the whole ascent phase and at all the 8 locations per tank is presented. Here, only specific focus over the periods of pressure drop/rise is given.

At this point, it is important to highlight the transformation of the coordinate system. Due to Flow3D requirements, the original coordinate system of the launcher should be rotated such that the -z axis is now the vertical one i.e. in the direction of the launch.

It is also important to recall Figure 3.1.2 where the sloshing angle calculation locations are listed in order to have a better understanding of the results that follow.

4.1.1. Liquid Oxygen sloshing angle

The simulation of liquid oxygen's sloshing involved 6 flights. The simulated flights are F034, F042, F050, F052, F053 and F060.

Flight F034 - LO_x tank

This is a flight with a relatively high pressure rise (compared to others). Flight F034 is characterized by an early pressure rise as well as by a late (lower) one.

It can be seen in Figure 4.1.1 that the initial pressure rise is accompanied by a high sloshing angle at locations 5 and 6. The angle exceeds the margin of 15 deg and it is very likely that breaking waves exist near this region. The recorded temperature drop near the first pressure rise region can support the possibility of strong waves near the region (see Figure 4.1.2).

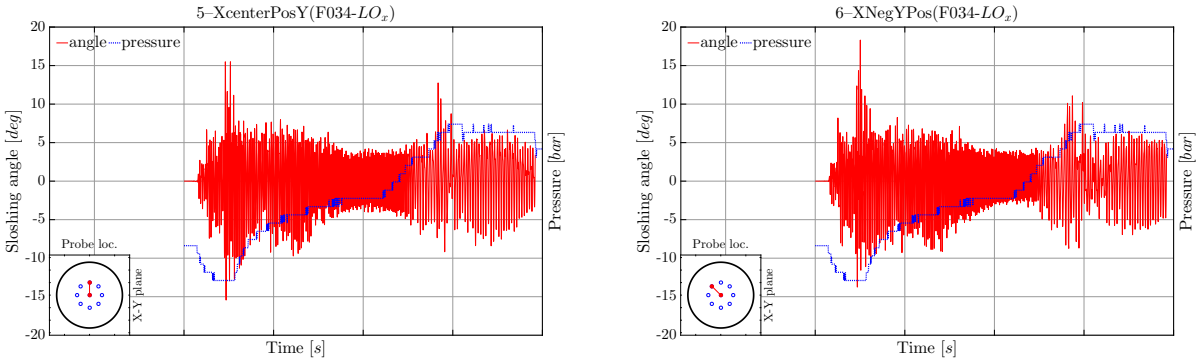

Figure 4.1.1: Sloshing angle of F034 LO_x tank at location index 5 and 6.

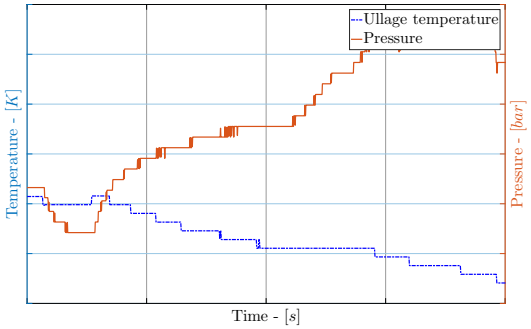

Figure 4.1.2: Temperature and Pressure evolution of F034 LO_x tank (flight sensors)

The second, smaller, pressure rise occurs right after the standard pressure rise due to the acceleration drop (see Section 4.2.1). Again, observing Figure 4.1.3 we can see relatively high angles taking place at the same time. A small temperature drop is also present near this region.

Near the first pressure rise period several strong waves were spotted, similar to the one of Figure 4.1.4 (a). Additionally, a small breaking wave exists Figure 4.1.4 (b). No splashing has been noticed.

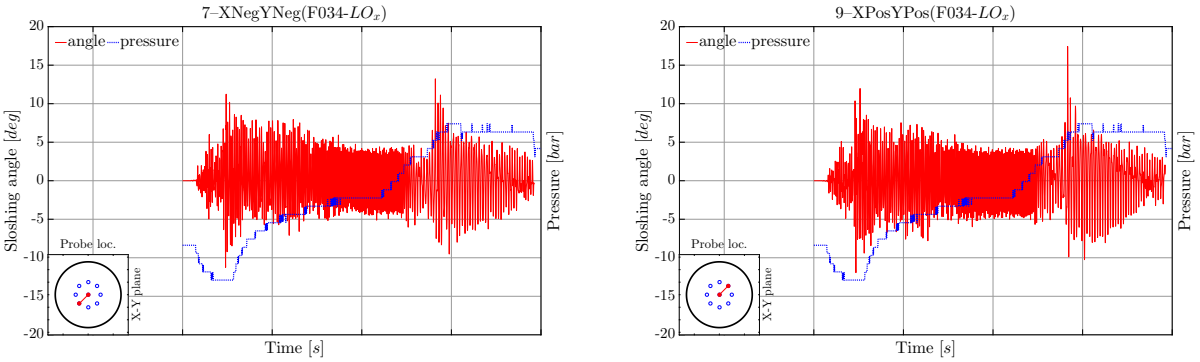

(a) (b)

Figure 4.1.3: Sloshing angle of F034 LO_x tank at location index 7 and 9.

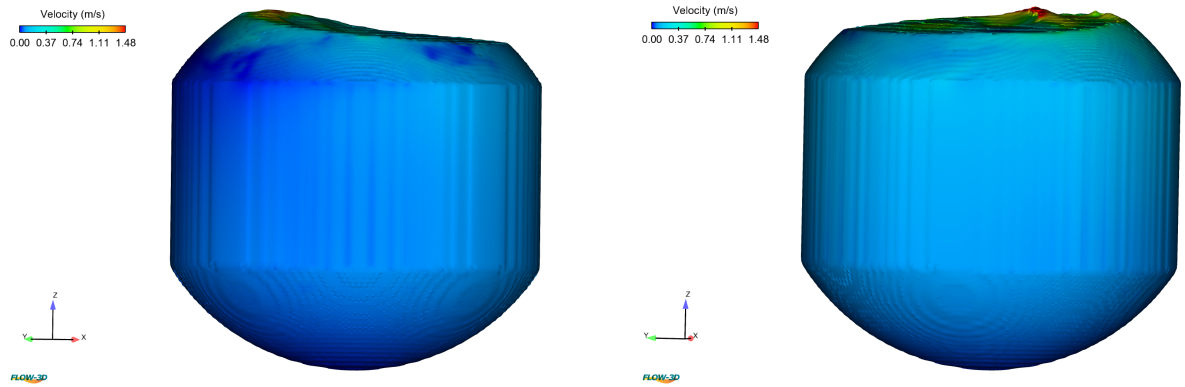

(a) High wave. (b) Small breaking wave.

Figure 4.1.4: Wave visualization near the first pressure rise of F034

Near the region of the second pressure rise only high amplitude planar waves were spotted. No breaking waves or splashing exists. However the amplitude of the oscillations is higher near this region which might explain the small pressure rise.

Flights F042 and F053 - LO_x tank

These two flights demonstrated a low pressure rise (below average - see Figure 3.2.1). The pressure rise time period is the same for both flights. Actually, this is a small pressure rise that occurs in all of the flights and is directly connected to the point of the maximum acceleration ($Accel_x$) magnitude (see Section 4.2.1).

Other than that, these flights show no other pressure rise. This can indeed be depicted in the sloshing angle evolution shown in Figure 4.1.5 and Figure 4.1.6, where the sloshing behavior in the two major axis (-x and -y) is shown. Both flights maintain a low sloshing amplitude which is at all times below $8\,deg$ for F042 and below $10\,deg$ for F053. Visual investigation of the liquid's behavior confirms the low sloshing amplitude, as no strong waves are formed during the ascent phase of these two flights.

The temperature profile of flight F042 (Figure 4.1.7 (a)) confirms that no evident extensive heat transfer between the ullage and the liquid takes place as only a small and gradual temperature drop is observed. For flight F053 in Figure 4.1.7 (b) there is no clear indication. The temperature reaches a relatively higher level due to the initial helium injection. After this point, there is a faster temperature decay but this is probably due to the higher temperature difference within the system and not due to sloshing.

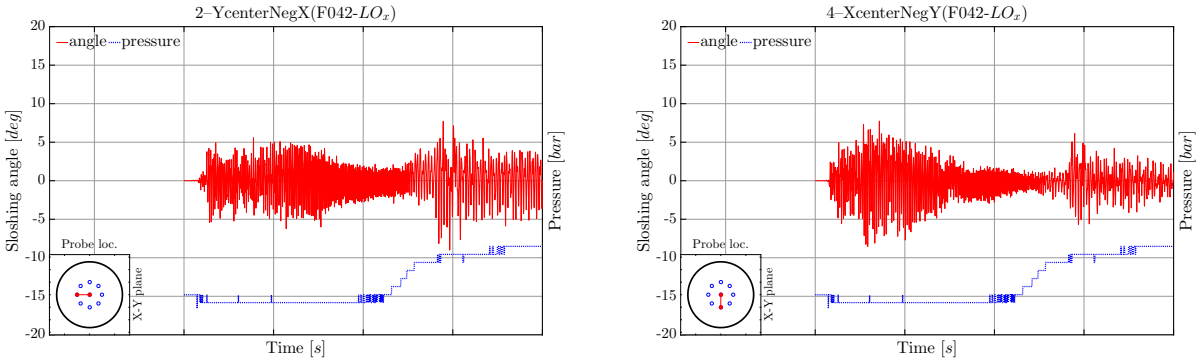

Figure 4.1.5: Sloshing angle of F042 LO_x tank at location index 2 and 4.

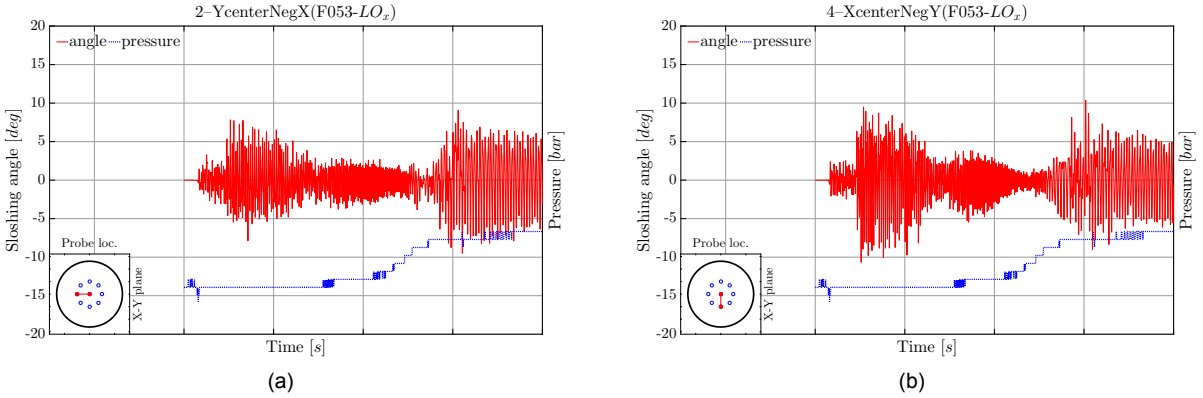

Figure 4.1.6: Sloshing angle of F053 LO_x tank at location index 2 and 4.

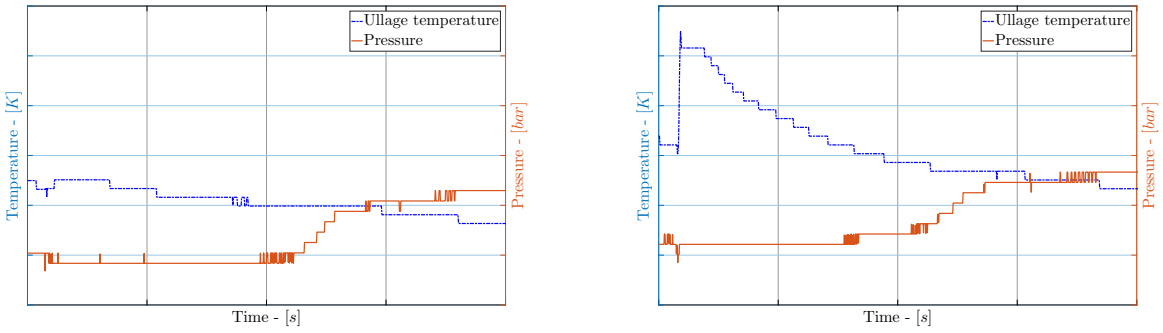

Figure 4.1.7: Ullage temperature and pressure of F042 and F053 LO_x tank.

Flights F050 and F052 - LO_x tank

Flights F050 and F052 show a high pressure rise during the ascent phase, 10 % and 8 % respectively.

The pressure of flight F050 rises in two steps; one initial step which happens early in flight and a later, smaller step, which occurs a bit after the standard pressure rise due to acceleration decay.

The sloshing angle is higher during the first pressure rise. It reaches above 20 deg which is an indication that strong waves might exist. By visually inspecting the CFD results, several

breaking waves are osberved during the first pressure rise period. One of those is shown in Figure 4.1.9. No liquid jettison in the ullage is visible however that could be due to the low mesh density.

During the second pressure rise period the amplitude is lower than the first but still higher than the rest of the flight. This might be a clue about the small pressure rise that occurs despite the non-existence of large waves.

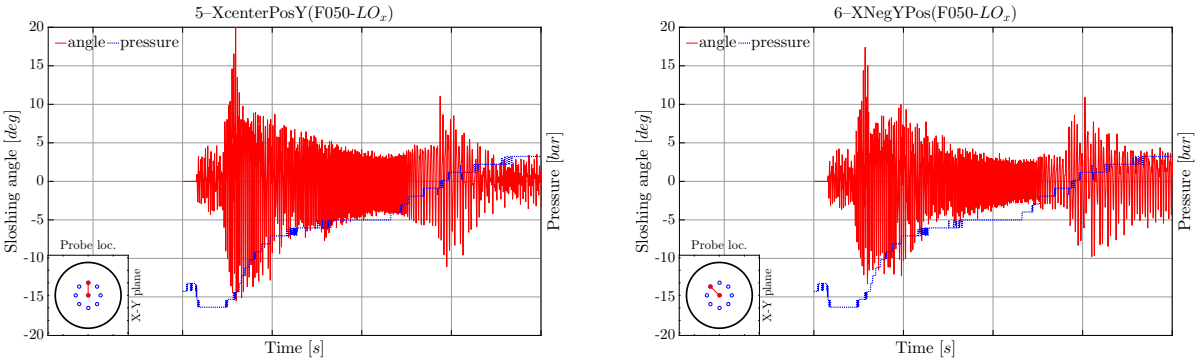

(a) (b)

Figure 4.1.8: Sloshing angle of F050 LO_x tank at location index 5 and 6.

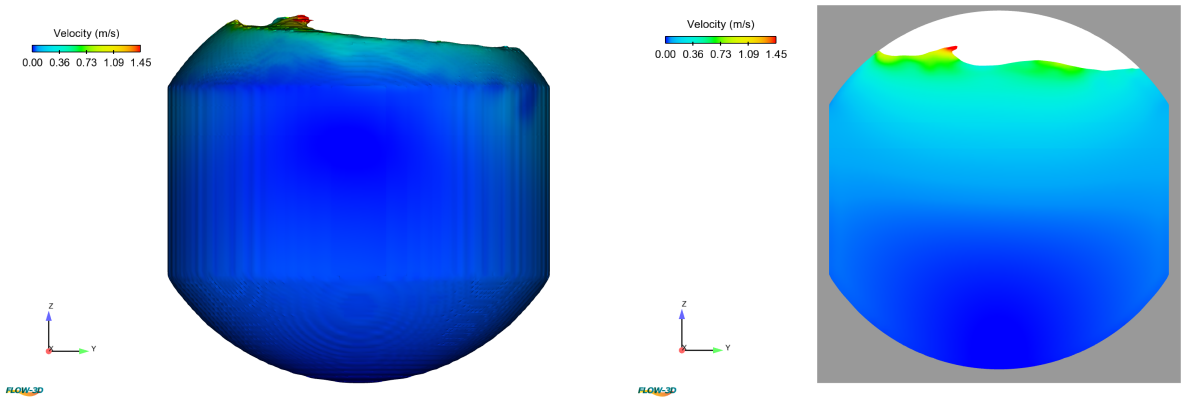

(a) 3D (b) 2D

Figure 4.1.9: Wave visualization near the first pressure rise of F050

Flight F052 shows a sudden pressure rise late in the ascent phase. The sloshing angle almost reaches $20\,deg$ as shown in Figure 4.1.10. This can be also visually confirmed by the liquid sloshing results. As it can be seen in Figure 4.1.11, a strong wave is formed near the tank walls which causes liquid splashing. During the early stages of the flight, the sloshing angle magnitude is relatively low ($< 5\,deg$). This can explain the almost flat pressure evolution.

The temperature evolution of both flights is demonstrated in Figure 4.1.12. During the first pressure rise of F050, a notable temperature drop is recorded in parallel with the sloshing period. This is not observed during the second pressure rise period, which has a lower sloshing magnitude after all.

Despite the non-existence of sloshing during the early stage of F052, a significant temperature drop is noted. However, this might be because of the higher starting point of temperature due to the initial helium injection. Later in flight, when the splashing wave occurs, no temperature drop is noticed. Again, the temperature sensor due to its location (top-center

position) is probably not affected by the observed circumferential wave.

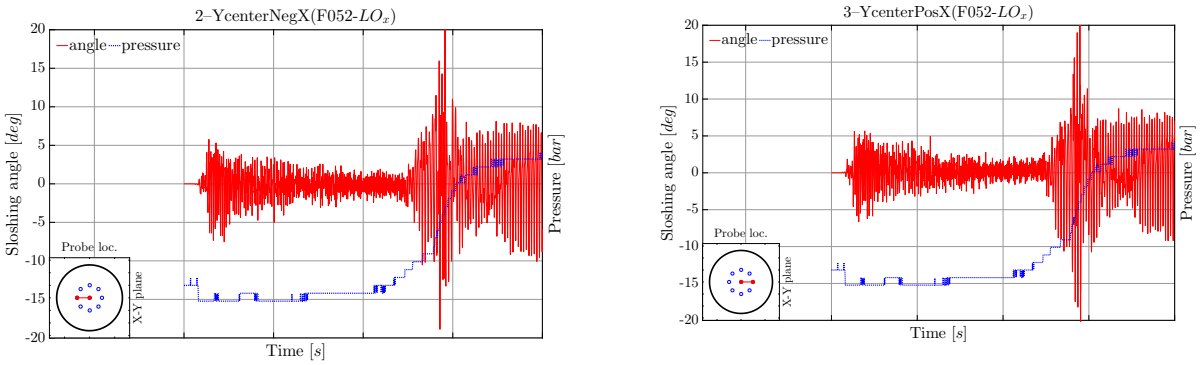

(a) (b)

Figure 4.1.10: Sloshing angle of F052 LO_x tank at location index 2 and 3.

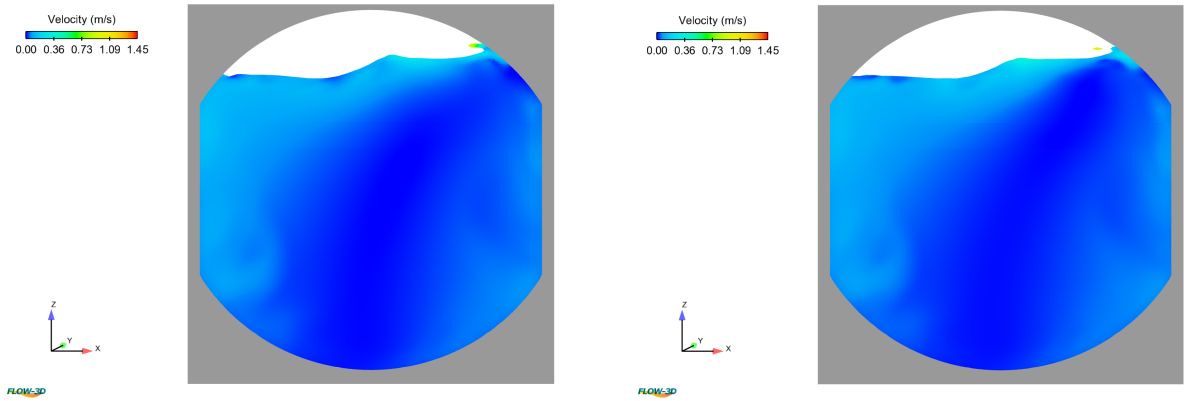

(a) Breaking wave - 2D (b) Splashing - 2D

Figure 4.1.11: Splashing wave F052 - Late occurrence.

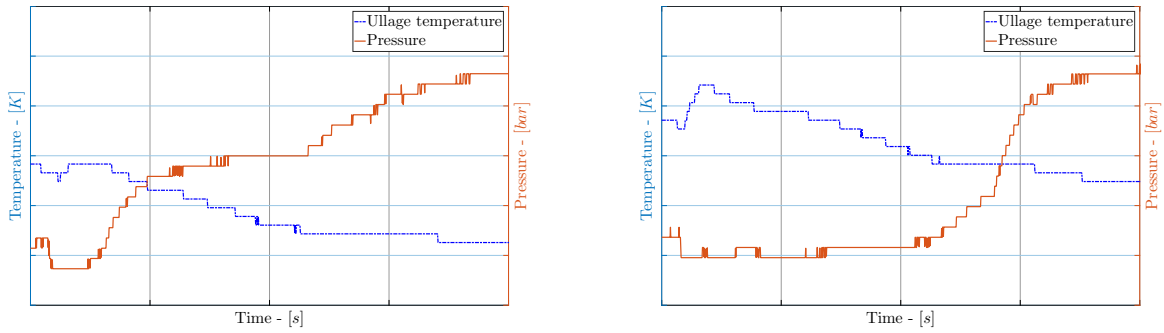

(a) F050 (b) F052

Figure 4.1.12: Ullage temperature and pressure of F050 and F052 LO_x tank.

Flight F060 - LO_x tank

This is a flight with an early pressure rise. It appears that a high sloshing angle occurs, however it is not completely aligned with the moment of pressure rise.

In this flight, the sloshing angle only reaches a peak instantaneously, without causing any breaking waves. This behavior is present in only one of the eight directions (see Appendix - Figure A.0.6). After that, the sloshing angle magnitude shows a gradual decrease during the period of the pressure rise.

Flight F060 is a flight with one of the lowest ullage volumes. The high sloshing angle occurs early were the condensation mechanism is still noticeable, thus low amplitude sloshing might just cause little evaporation to counterbalance the condensation effects. Due to the low ullage volume it is expected that little evaporation can result in higher effects in the pressure rise; this can explain the unavoidable pressure rise despite the low amplitude sloshing.

The fact that no intense temperature drop is noticed in the tank Figure 4.1.14 supports the claims that sloshing is not significant which is also confirmed by the postprocessing of the CFD results, as no strong waves are noticed inside the tank.

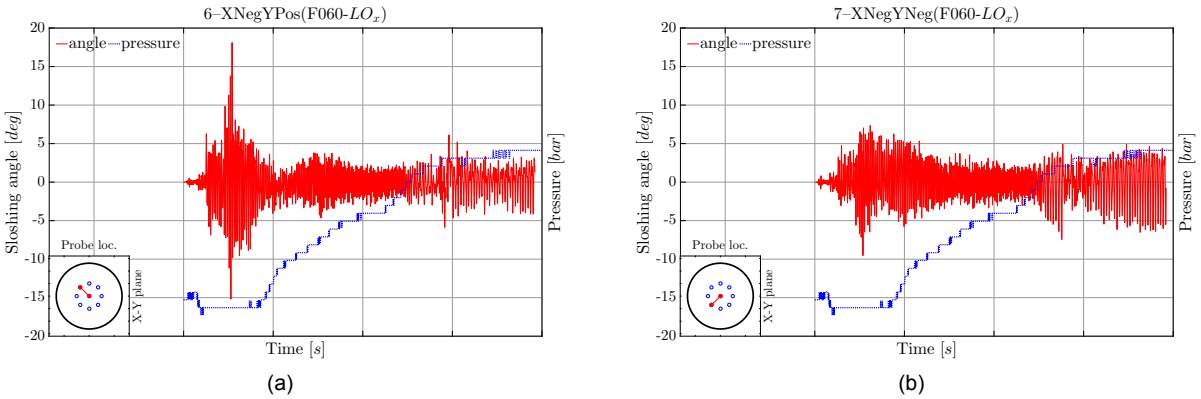

Figure 4.1.13: Sloshing angle of F060 LO_x tank at location index 6 and 7.

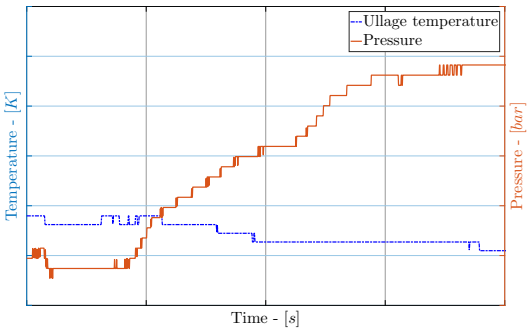

Figure 4.1.14: Ullage temperature and pressure of F060 LO_x tank.

4.1.2. Liquid Hydrogen sloshing angle

The simulation of liquid hydrogen's sloshing involved 6 flights. The simulated flights are F009, F034, F042, F050, F052 and F053.

Flight F009 - LH_2 tank

Flight F009 is one of the two flights with the highest pressure drop inside the LH_2 tank. It can be seen in the sloshing angle results, that high angles occur right before the sudden pressure drop. The angle in Figure 4.1.15 reaches almost 20 deg and this is a clear indication of large waves. Additionally, F009 is one of the few flights that a notable temperature drop has been recorded in the temperature sensor (Figure 4.1.16), which supports the fact of liquid reaching the higher region of the ullage.

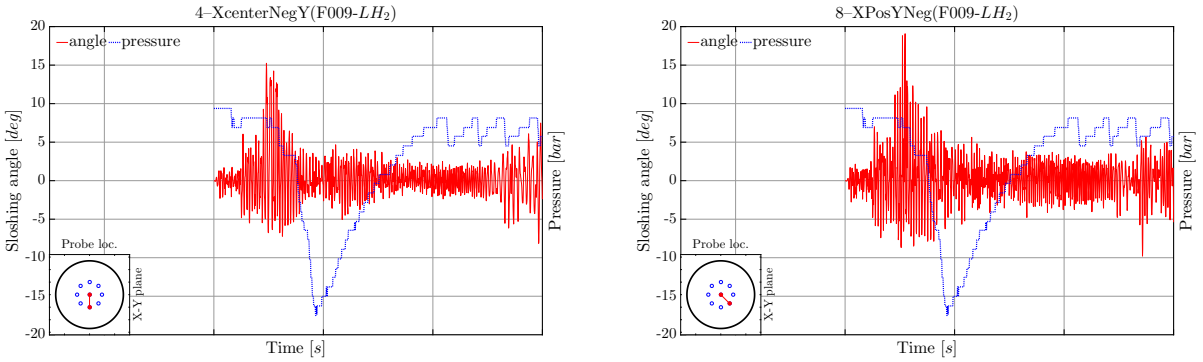

(a) (b)

Figure 4.1.15: Sloshing angle of F009 LH_2 tank at location index 4 and 8.

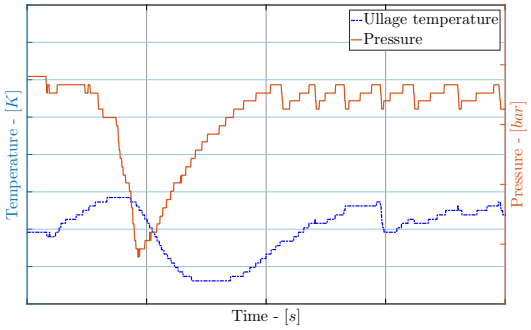

Figure 4.1.16: Temperature and Pressure evolution of F009 LH_2 tank (flight sensors)

During the pressure drop period, at least 10 breaking waves were spotted in the CFD postprocessing, 4 of which also caused splashing. A characteristic example of the formation and breaking of a splashing wave is shown in Figure 4.1.17. It can be seen that liquid is jettisoned onto the ullage and is likely to reach the upper dome region where the temperature sensor is located.

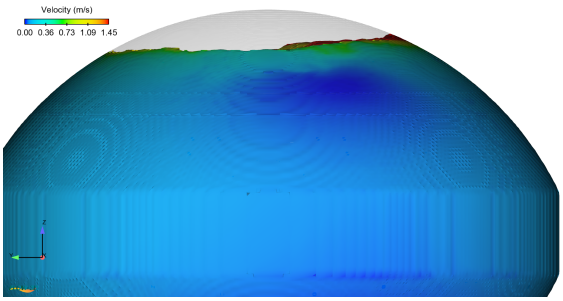

(a) $(0\,s)$.

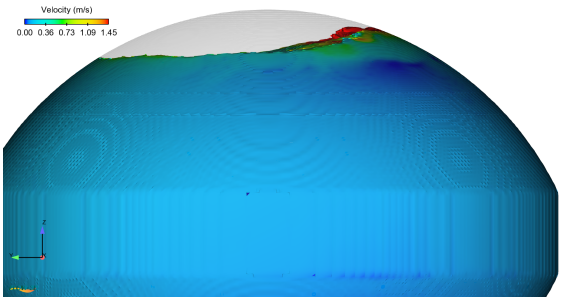

(b) $(0.1\,s)$.

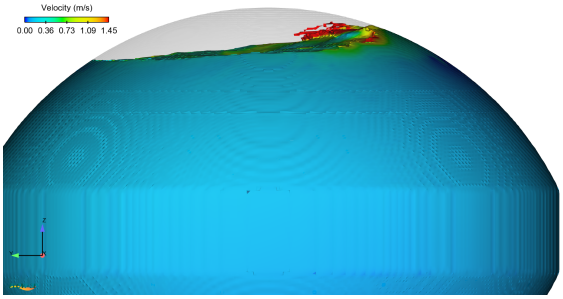

(c) $(0.2\,s)$.

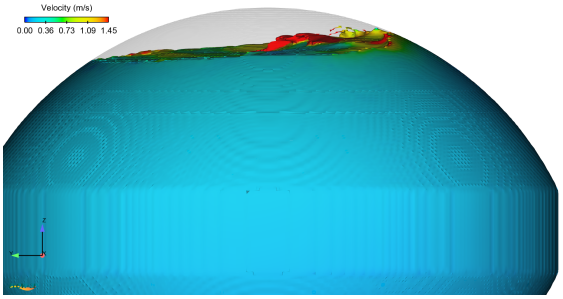

(d) $(0.3\,s)$.

Figure 4.1.17: Splashing wave formation/breaking of flight F009 LH_2 tank at location index 4 ($0.3\,s$ duration).

Flight F050 - LH_2 tank

This is also a high pressure drop flight demonstrating identical behavior with flight F009. Although there is clear indication of possible liquid jettison onto the ullage, due to the temperature drop recorded at the moment of pressure drop, this can not be confirmed by the sloshing simulation.

As it can be seen in the sloshing angle graphs of Figure 4.1.18, the situation is not similar to F009 which demonstrated an identical pressure drop. In this case, no high waves are noticed and wave breaking or splashing by no means takes place. However, it is remarkable that the sloshing magnitude is higher around the drop (location 4) when compared to the rest of the flight but it is still well below 10 deg.

The fact that a temperature drop is recorded after the pressure drop (Figure 4.1.19) indicates that a sloshing possibility might exist. Recall that only the kinematic profile of the launcher itself (linear acceleration and roll rates) were included in the simulation. Other effects, such as vibrations, could possibly help us understand why the pressure and temperature drop take place.

The CFD simulation led to no clear results regarding F050 sloshing. The kinematic profile of the launcher is not sufficient to create strong waves inside the tank, however the fact that there is an increasing sloshing magnitude around the drop can still be a sing of potential sloshing existence.

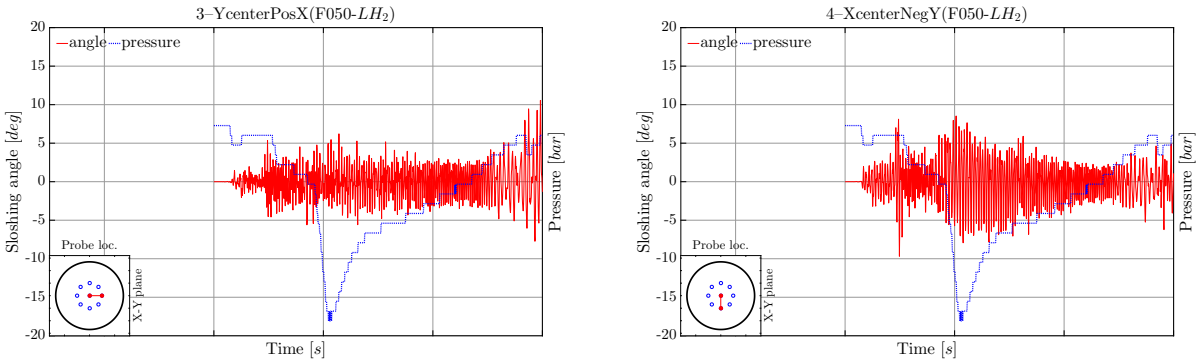

(a) (b)

Figure 4.1.18: Sloshing angle of F050 LH_2 tank at location index 3 and 4.

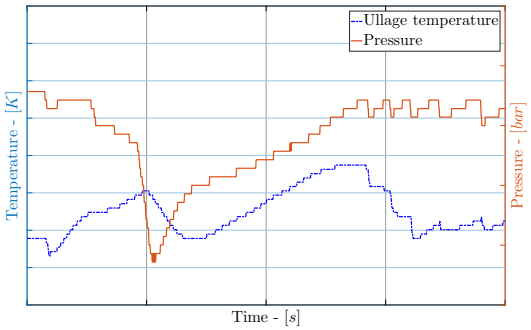

Figure 4.1.19: Temperature and Pressure evolution of F050 LH_2 tank (flight sensors)

Flight F034 - LH_2 tank

Flight F034 shows an average drop which however starts with a small sudden drop of the pressure. At the time of the first sudden drop, high sloshing angles between 15 deg and 20 deg were recorded as it can be seen in Figure 4.1.20.

The fact that the temperature profile of Figure 4.1.21 remains constant (i.e. not rising) during the drop is an indication that liquid has reached the upper region of the ullage. However, the liquid's quantity might not be sufficient to trigger a notable temperature drop as in the two previous flights (F009 and F050).

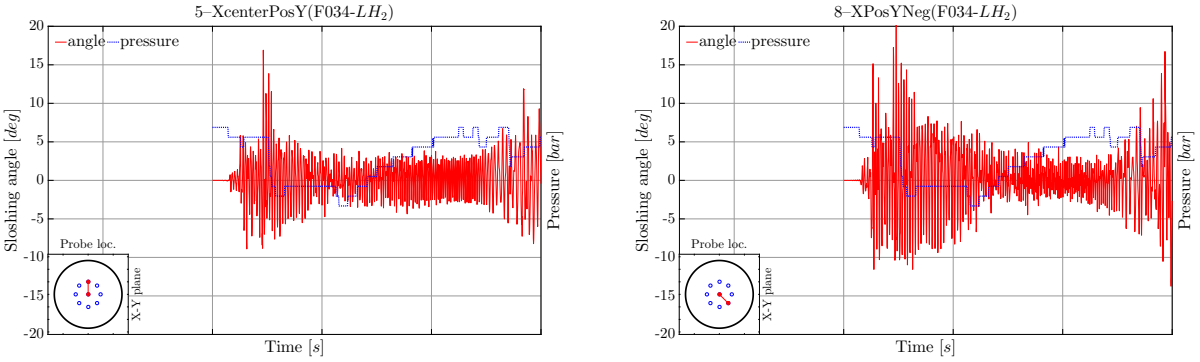

(a) (b)

Figure 4.1.20: Sloshing angle of F034 LH_2 tank at location index 5 and 8.

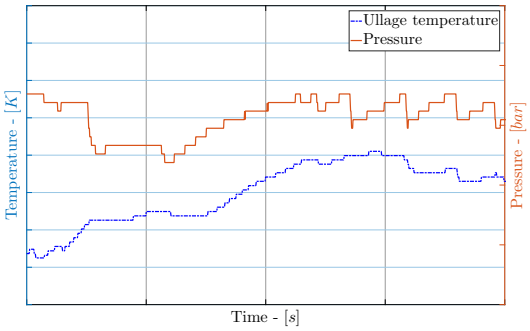

Figure 4.1.21: Temperature and Pressure evolution of F034 LH_2 tank (flight sensors)

The CFD results postprocessing showed several breaking waves to take place around the pressure drop period. One of the strongest, is shown in Figure 4.1.22. It is a splashing wave which probably led to liquid jettison near the temperature sensor area. This can explain the interruption of the temperature increase near the pressure drop time period.

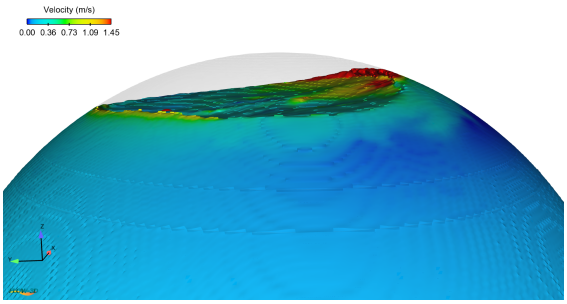

(a) $(0\,s)$.

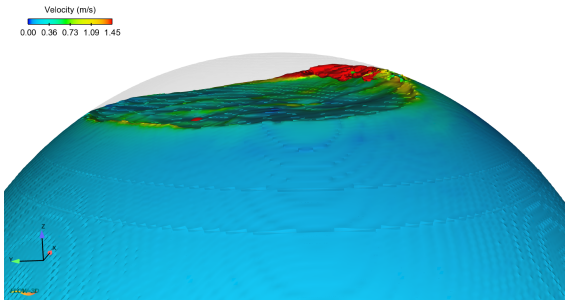

(b) $(0.1\,s)$.

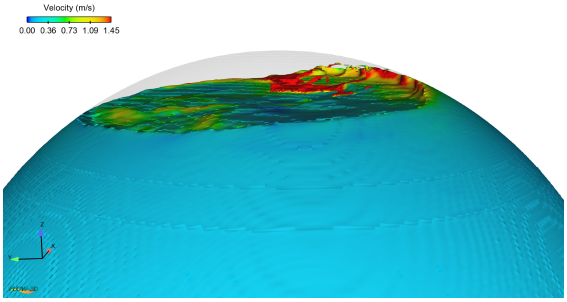

(c) $(0.2\,s)$.

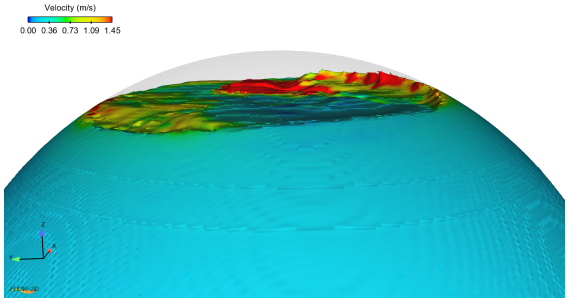

(d) $(0.3\,s)$.

Figure 4.1.22: Splashing wave formation/breaking of flight F034 LH_2 tank at location index 8 $(0.3\,s$ duration).

Flights F042 - F052 - F053 - LH_2 tank

These are two low pressure drop flights (F042, F052) and one flight (F053) where no significant pressure drop is recorded at all.

Flights F042 and F052 have identical pressure evolution profiles. Both show an approximately ~ 4% gradual pressure drop followed by the usual gradual pressure rise.

Flight's F042 sloshing magnitude remains below $5\,deg$, only showing a few peaks around $8\,deg$ near the pressure drop period (Figure 4.1.23). The ullage temperature (Figure 4.1.24) maintains a gradual rising behavior which is an indication of no or few liquid jettison onto the ullage.

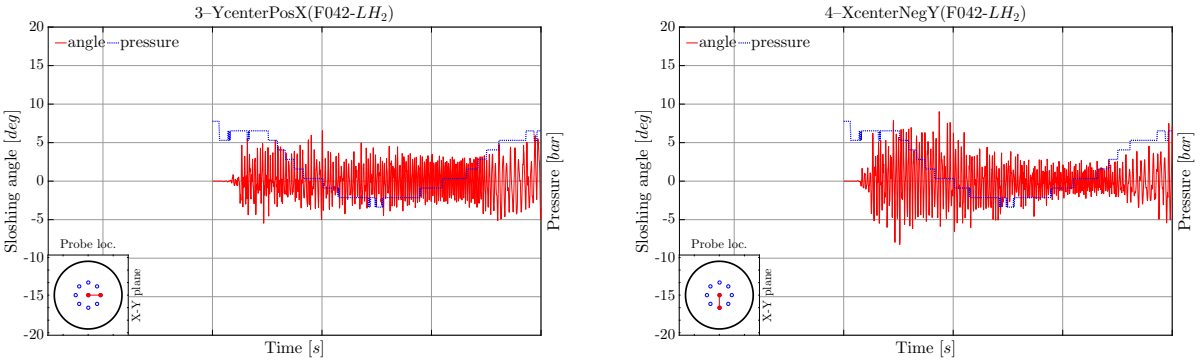

(a) (b)

Figure 4.1.23: Sloshing angle of F042 LH_2 tank at location index 3 and 4.

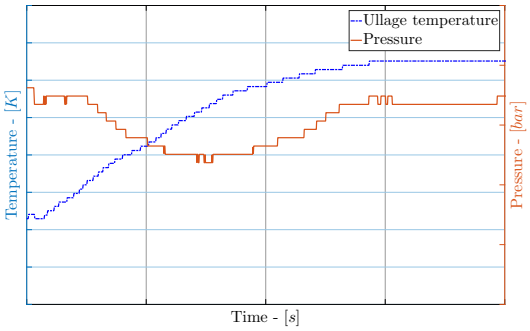

Figure 4.1.24: Temperature and Pressure evolution of F042 LH_2 tank (flight sensors)

The situation is similar for flight F052. This can be seen in Figure 4.1.25 and Figure 4.1.26. The sloshing angle and the temperature profile indicate that no high amplitude sloshing occurs during this flight as well.

Finally, flight F053 is a flight showing the lowest pressure drop that has been up to now noticed. The sloshing angle (Figure 4.1.27) confirms this, as no excessive sloshing occurs during this flight. There are only two small peaks reaching the amplitude of $10\,deg$ and could possibly be related to the tiny temperature drops that are shown in Figure 4.1.28. What is also different, is that for F053, the duration of sloshing (sloshing angle $> 5deg$) is half the time of the previous two flights. The smaller sloshing duration might also explain the fact that no pressure drop is recorded in this specific flight.

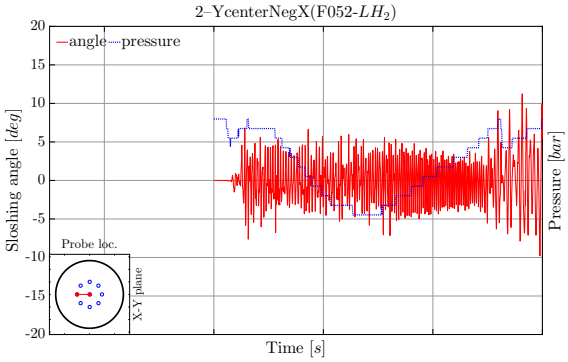

(a)

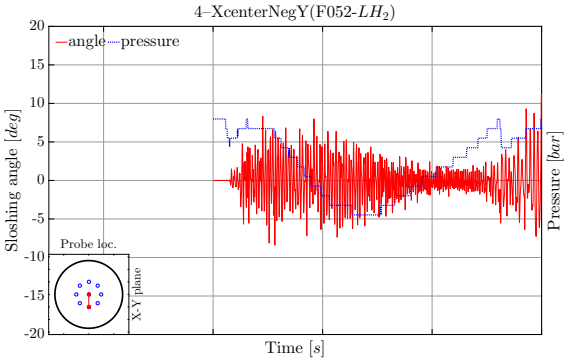

(b)

Figure 4.1.25: Sloshing angle of F052 LH_2 tank at location index 2 and 4.

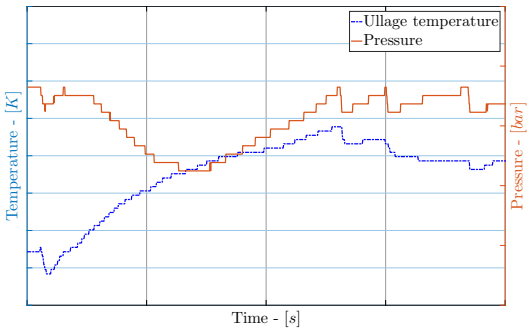

Figure 4.1.26: Temperature and Pressure evolution of F052 LH_2 tank (flight sensors)

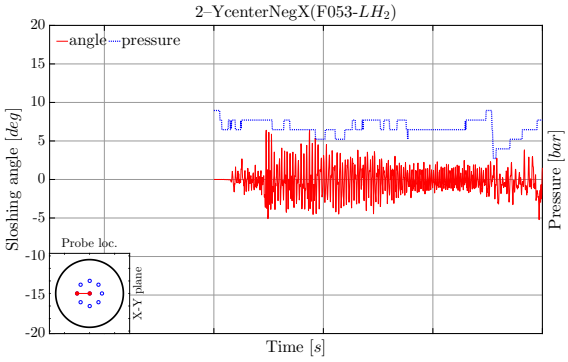

(a)

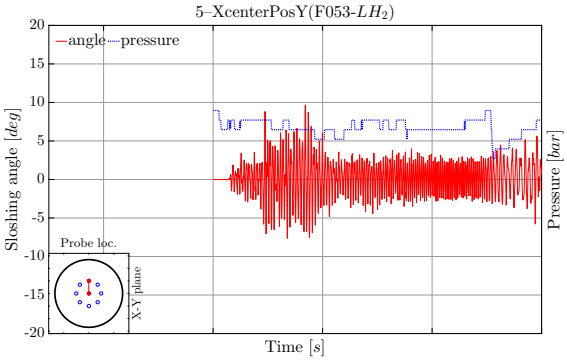

(b)

Figure 4.1.27: Sloshing angle of F053 LH_2 tank at location index 2 and 5.

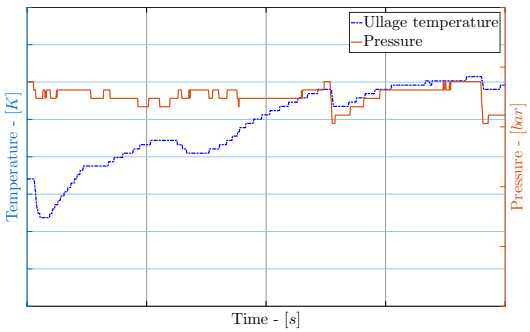

Figure 4.1.28: Temperature and Pressure evolution of F053 LH_2 tank (flight sensors)

4.2. Data Analysis

In this section, the results of data analysis are presented. Focus is given on the parameters of Section 3.2 and all the crucial observations are listed. The final form of the prediction model is presented along with the maximum prediction intervals for the LO_x tank pressure rise.

4.2.1. Acceleration and Roll rates

The acceleration and the roll rate profiles were used in the CFD simulation (as inputs) but were also used for the construction of the statistical model. As described in Section 3.2.1, the periods of interest for the acceleration and the roll rates were defined through the variables d_1, d_2 and d_3. The outcome of the variables is listed in Table 4.2.1. These time periods correspond to the maximum correlation coefficients, however, as it can be seen in Figures 3.2.6 and 3.2.7, the highly correlated regions extend beyond these specific time values.

For the LO_x tank, the period from $20\,s$ prior to the pressure rise up to $20\,s$ before the pressure stabilization is the one showing the highest correlation of acceleration. However, values of d_3 spanning from $10\,s$ to $50\,s$ also show strong correlation. On the other hand, the roll rates highest impact is limited to a period of $d_1 = 30$ and $d_3 = 25 - 55\,s$. It can be said that the effect of the roll rates on the pressure rise starts earlier. One should also keep in mind that despite the LO_x tank ullage pressure has a solely rising behavior, it initially drops due to the early condensation. However, this effect is lower than the LH_2 tank case, and it is not visible in the pressure plots because it is either insignificant or it is instantaneously compensated by helium injection, as already explained.

Table 4.2.1: Maximum correlated kinematic profiles for both tanks as defined in Figure 3.2.5

Kinematic Profile	d_1	d_2	d_3	R
$LO_x\ Accel_{-yz}$	$20\,s$	-	$20\,s$	0.74
$LO_x\ Roll_{-y}$	$30\,s$	-	$40\,s$	0.81
$LH_2\ Accel_{-yz}$	-	$5\,s$	$35\,s$	0.49
$LH_2\ Roll_{-y}$	-	$15\,s$	$45\,s$	0.47

The effect of the kinematic profile on the LH_2 tank is different. Now, the kinematic profile seems to impact the pressure drop earlier, having an average value of $d_2 = 10\,s$. This can be supported by the previous observation, as the pressure drop comes first in both tanks. However, in this case the kinematic profile is not so strongly correlated to the pressure drop and in turn, no safe conclusion can be made.

The correlation plots of the LO_x tank ullage pressure rise to the kinematic profile can be seen in Figure 4.2.1.

As already stated, the correlation of the kinematic profile of the launcher to the LH_2 tank pressure drop, is poor. Observing the relevant correlation plots (Figure 4.2.2 (a) and Figure 4.2.3 (a)) it is evident that several outliers exists. Focusing on these outliers, we see that they are mainly flights with a steep and sudden pressure drop, similar to flights F009 and F050 of the CFD analysis, while the majority of flights show a more gradual pressure drop, like F042 and F052. It is also clear that a drop of the temperature is recorded during the sudden pressure drop. This can be observed in Figure 4.2.4 for flights F001, F009, F018, F024 and F050. Additionally, those happen to be 5 out of the solely 8 flights where a temperature drop is recorded. Recall that the location of the temperature sensor (top of the tank) inhibits the proper recording of the temperature evolution, as it may only be reached in case of extremely strong splashing waves.

By removing these 5 outliers from the correlation approach, the correlation coefficients

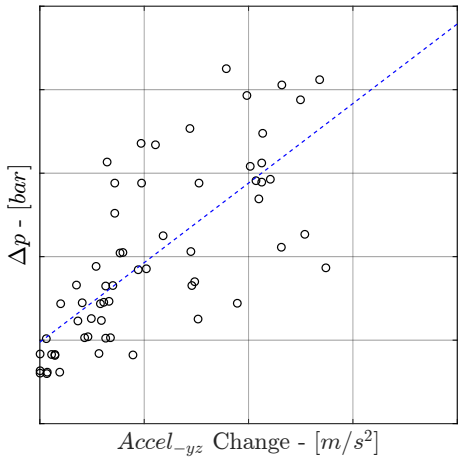

(a) Pressure rise vs Acceleration magnitude change - $R = 0.74$

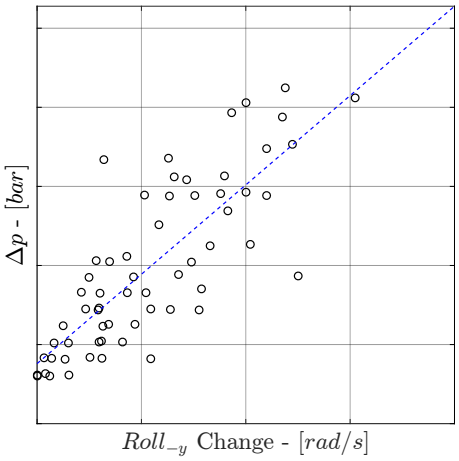

(b) Pressure rise vs Roll rate change - $R = 0.81$

Figure 4.2.1: Launcher kinematic profile correlation to the LO_x ullage pressure rise.

change dramatically to a higher level. This can be observed in Figure 4.2.2 (b) and Figure 4.2.3 (b) for both the acceleration and the roll rate change. The new correlation plots show that the magnitude of the LH_2 tank ullage pressure drop is now proportional to the change of the kinematic profile. Accepting that the observed steep pressure drop (accompanied by a temperature drop) is the outcome of strong sloshing waves, it can be said that the formation of waves can not be estimated through a simple kinematic magnitude analysis and it is in a way uncertain or it is also connected to another parameter (e.g. vibrations) which was not included in this approach. This can be also supported by the outcome of the CFD study as strong breaking waves exist in F009 and not in F050, despite their identical recorded pressure/temperature evolution.

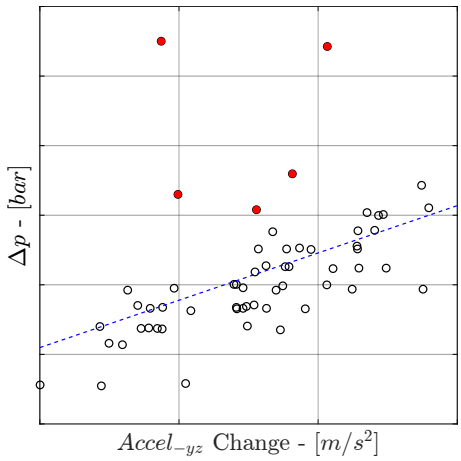

(a) Pressure drop vs Acceleration magnitude change (Full dataset - Outliers in red) - $R = 0.49$

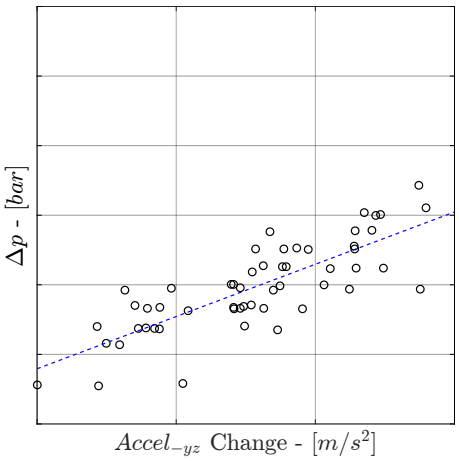

(b) Pressure drop vs Acceleration magnitude change (Removed outliers) - $R = 0.802$

Figure 4.2.2: Correlation of the acceleration change magnitude to the LH_2 tank ullage pressure drop.

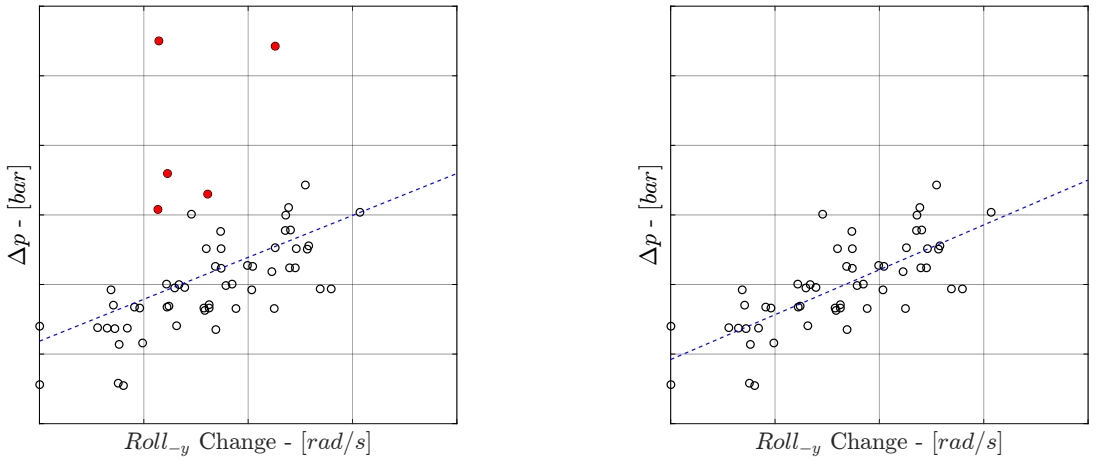

(a) Pressure drop vs Roll rate magnitude change (Full dataset - Outliers in red) - $R = 0.47$

(b) Pressure drop vs Roll rate magnitude change (Removed outliers) - $R = 0.735$

Figure 4.2.3: Correlation of the roll rate change magnitude to the LH_2 tank ullage pressure drop.

One other important outcome that can be extracted from the acceleration profile is the cause of the small pressure rise that occurs in the LO_x tank ullage during the linear acceleration -x drop. The CFD analysis showed that no intense sloshing occurs during this period. By studying the fill level behavior during the acceleration drop phase it can be seen that in most of the flights a notable fill level rise occurs simultaneously.

This can be clearly seen in flights F034, F042, F050 and F060. These are flights which have a low sloshing profile during the period of interest and the acceleration induced pressure rise is distinct. As shown in Figure 4.2.5, during the acceleration drop period a notable level rise is noted. In these specific flights, this level rise can be from $2\,mm$ to $3\,mm$. This level rise coincides with the small pressure rise during the same period as shown in the figures.

The ullage volume varies from flight to flight so the effect would not be identical to every one of them. However, for those specific flights the outcome was estimated and validated by the simple Equation (4.2.1) (ideal gas law assumption), where subscript 1 refers to the conditions prior to the acceleration drop and subscript 2, to the conditions after. It should be understood that during this period possible evaporation/condensation might take place as well, a fact that can affect the observed fill level indication.

$$p_1 U_1 = p_2 U_2 \tag{4.2.1}$$

The fill level of the LH_2 is not examined, as extensive evaporation and de-pressurization occurs during this phase and it is not possible to have a clear view of the actual fill level conditions.

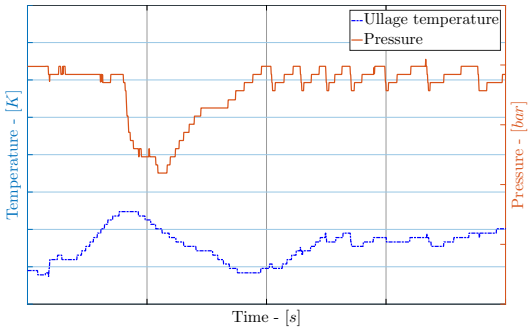

(a) Flight F001 LH_2 tank ullage pressure and temperature.

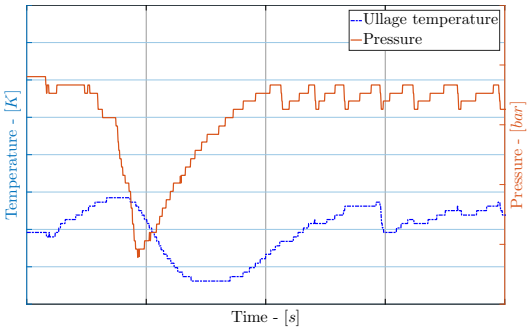

(b) Flight F009 LH_2 tank ullage pressure and temperature.

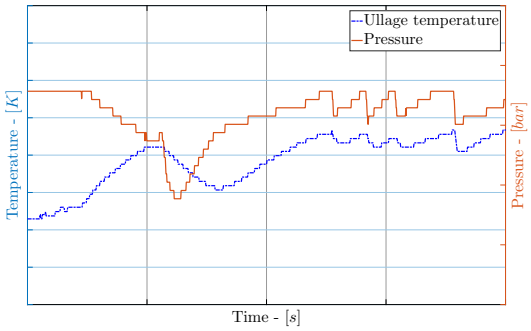

(c) Flight F018 LH_2 tank ullage pressure and temperature.

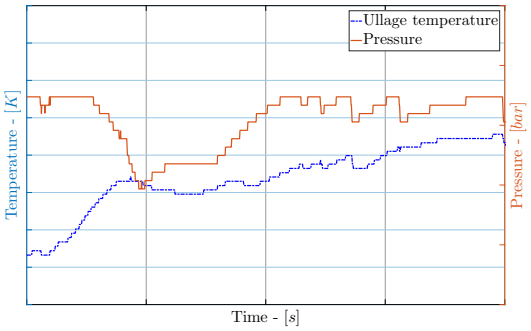

(d) Flight F024 LH_2 tank ullage pressure and temperature.

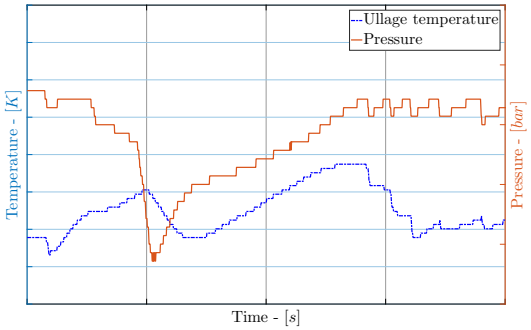

(e) Flight F050 LH_2 tank ullage pressure and temperature.

Figure 4.2.4: LH_2 tank sudden ullage pressure drop flights along with the ullage temperature evolution.

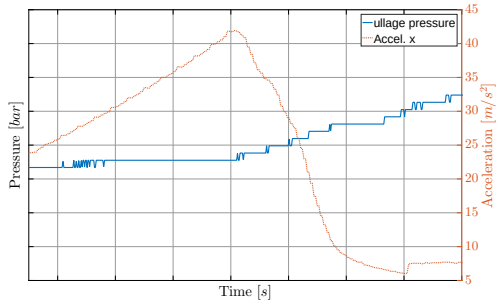

(a) Pressure/Accel -x vs Time - F034

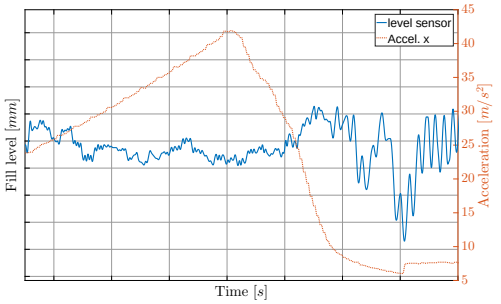

(b) Fill Level/Accel -x vs Time - F034

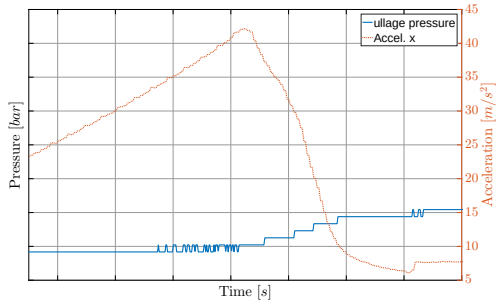

(c) Pressure/Accel -x vs Time - F042

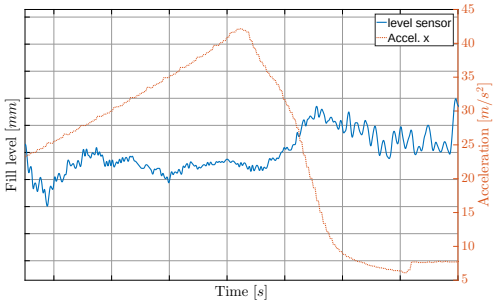

(d) Fill Level/Accel -x vs Time - F042

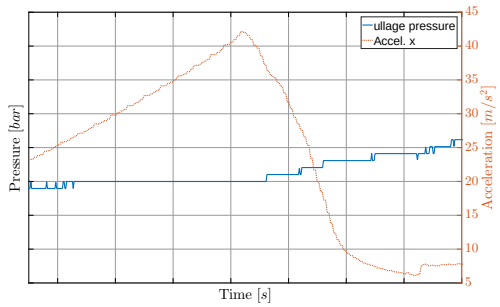

(e) Pressure/Accel -x vs Time - F050

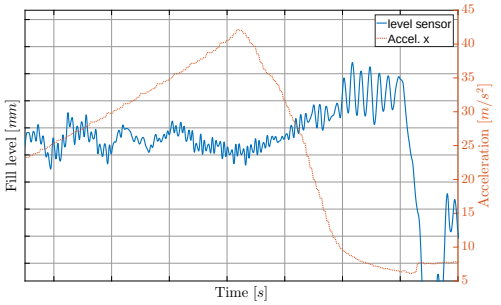

(f) Fill Level/Accel -x vs Time - F050

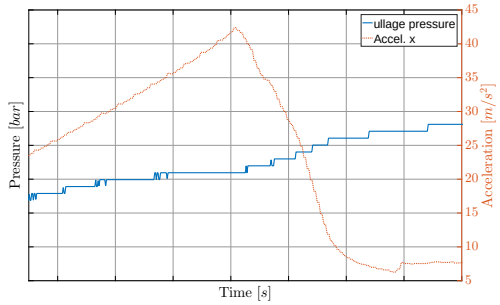

(g) Pressure/Accel -x vs Time - F060

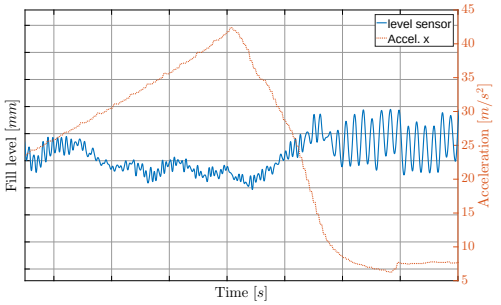

(h) Fill Level/Accel -x vs Time - F060

Figure 4.2.5: Acceleration drop induced pressure rise of flights F034, F042, F050 and F060.

4.2.2. Vibrations

No clear outcome could be reached by investigating the oscillating profile of the acceleration and the roll rates. The frequencies of these quantities were by far off the estimated natural frequencies of the tank systems as they were calculated in Section 3.2.1. This is something that can also be observed visually by seeing the evolution of the kinematic profile in Figure 3.2.3 and Figure 3.2.4.

As already explained when the excitation frequency of a liquid tank system reaches the natural frequency, it is possible that unstable sloshing is formed. The excitation's maximum magnitude also affects this outcome as described in Section 2.3. This approach was applied to the LH_2 tank and the results are shown below.

Recall that the outcome of the CFD of sloshing was not so clear for the LH_2 tank as not all of the flights with a strong pressure drop showed high sloshing magnitude. A high pressure drop/high sloshing magnitude flight is F009 where high waves were spotted exactly at the time of the drop. By looking at the vibration analysis of the LH_2 of this flight (Figure 4.2.6) we see that there are dominating frequencies between $0\,Hz$, and $0.7\,Hz$, right before the drop.

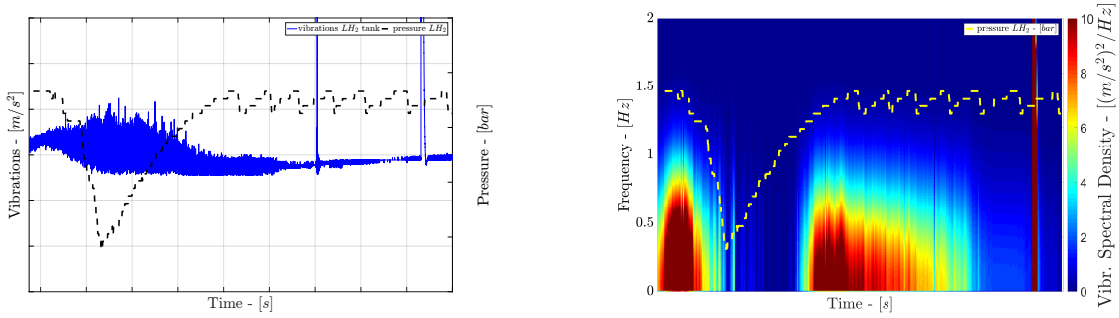

(a) Vibration signal during ascent phase.

(b) Vibration spectrogram

Figure 4.2.6: Vibration analysis of flight F009

The vibration signal is trimmed and only the period around the pressure drop is kept ($\sim 35\,s$). The phase diagram of dimensionless forcing amplitude (Figure 4.2.7) of the reduced signal shows that around the drop, one frequency/amplitude combination exists withing the chaotic sloshing region. As already mentioned, the CFD results showed high breaking waves and splashing for this flight, however recall that the CFD simulation did not include the effect of vibration and was only based on the kinematic profile.

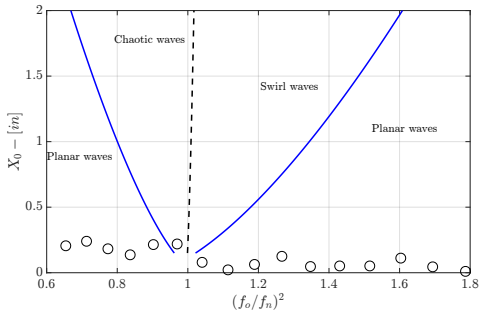

Figure 4.2.7: Phase diagram of dimensionless forcing amplitude as a function of frequency ratio of vibration signal around drop - F009.

Investigating the results of the other high pressure drop flight we again see dominating frequencies between $0\,Hz$, and $0.8\,Hz$. This time, the CFD results of flight F050 did not show

any intense sloshing (at least if compared to F009). However, the pressure behavior of the two flights is identical.

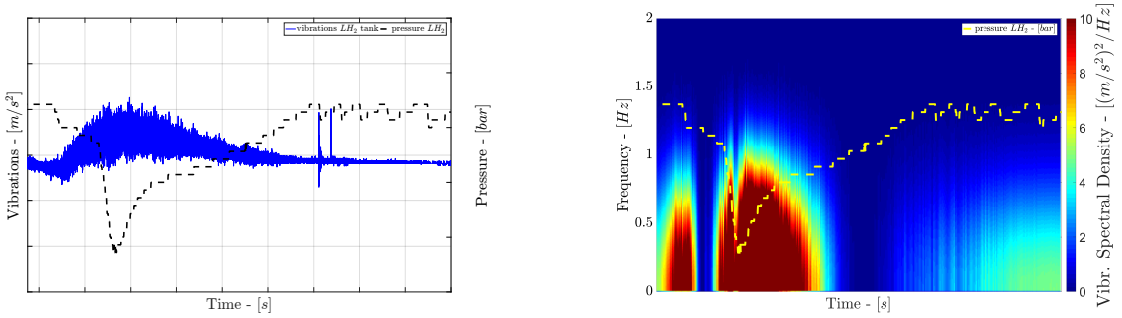

(a) Vibration signal during ascent phase.

(b) Vibration spectrogram

Figure 4.2.8: Vibration analysis of flight F050

Flight's F050 phase diagram of dimensionless forcing as shown in Figure 4.2.9, shows that there are at least two combinations of frequency/amplitude that lie within the chaotic sloshing region. Recall the fact that the kinematic profile of the launcher (acceleration and roll) did not play a dominating role regarding the pressure drop in the LH_2 tank, as described in the previous subsection (4.2.1). The vibrations frequency analysis highlights the possibility that the chaotic sloshing might be caused by these and not solely by the kinematic profile of the launcher.

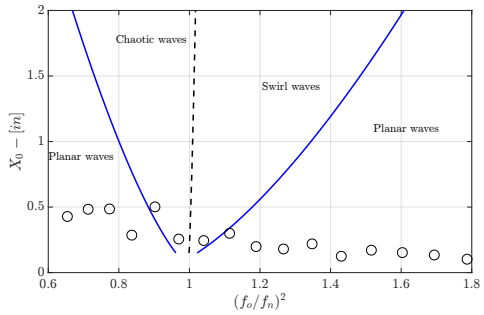

Figure 4.2.9: Phase diagram of dimensionless forcing amplitude as a function of frequency ratio of vibration signal around drop - F050.

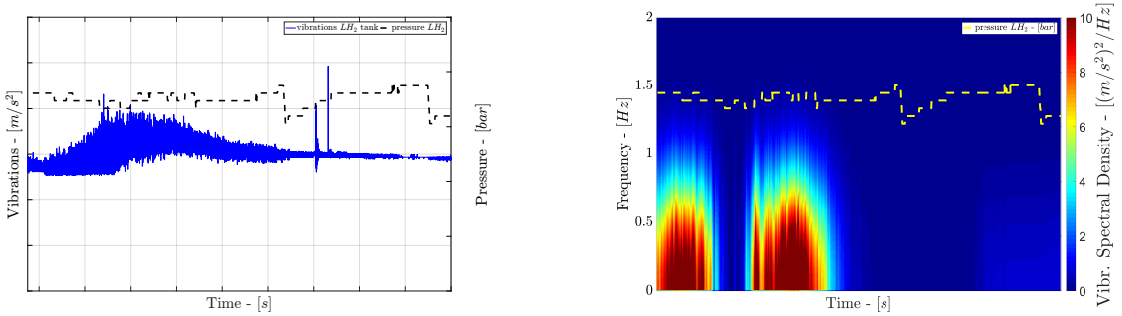

(a) Vibration signal during ascent phase.

(b) Vibration spectrogram

Figure 4.2.10: Vibration analysis of flight F053

Finally, investigating a no pressure drop flight which additionally demonstrated low sloshing magnitude in the CFD results, shows that despite frequencies near the natural frequency exist, no sufficient combination of frequency/magnitude lies inside the chaotic waves region. No pressure drop is observed in flight F053 and this is in agreement with the CFD and the vibrations frequency analysis.

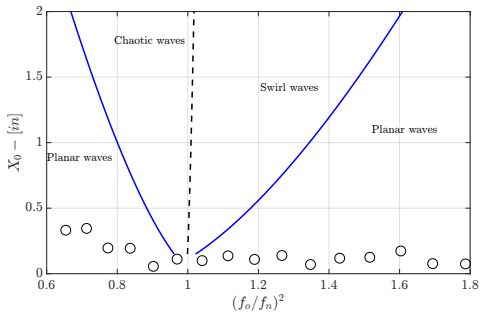

Figure 4.2.11: Phase diagram of dimensionless forcing amplitude as a function of frequency ratio of vibration signal around drop - F053.

It is interesting to see that in F050 where no intense sloshing resulted through the CFD simulation, there is a chance that the vibration profile could have affected the creation of high waves. However, this approach is only a rough approximation to investigate whether the measured vibrations can affect the sloshing behavior. It was developed through analytical calculations and experiments for spherical tanks at normal gravity. It is a fact, that the LH_2 is not fully spherical thus possible deviations might exists. What is however interesting is that in F050 indeed exist frequencies closer to the natural frequency of the tank (near the drop) as it was given by the designer, which under appropriate conditions can result in chaotic waves.

As already mentioned, no vibration frequency analysis is feasible for the LO_x tank as there are no adequate vibration sensors placed in this tank.

4.2.3. Ullage volume and temperature

The ullage of the LO_x tank is one of the parameters used in the statistical model due to its strong correlation to the pressure rise in the tank. The maximum ullage temperature also showed a strong correlation with the pressure rise magnitude. The correlation plots of the two variables are demonstrated in Figure 4.2.12.

It can be observed that both variables have a negative correlation to the pressure rise. It is understood that the higher the ullage volume is, the lower the pressure drop will be. This can be explained by considering the following. Having a larger ullage, the same evaporation at the free surface will have a lower impact on the overall ullage pressure rise. Additionaly, a larger ullage implies that less liquid is loaded in the tank, thus the tank walls wetted area is smaller. This can have an effect on the heat flux that reaches the liquid. Lower wetted area means less heat transfer between the tank walls and the liquid propellant, thus less evaporation might occur. Finally, with a larger ullage, the distance of the free surface from the helium inlet, which is located on top of the tank, is larger. This means that the heat transfer from the ullage to the liquid is in a way delayed and that in case of sloshing, the liquid is less likely to reach the top of the tank.

The maximum ullage temperature also shows a negative correlation to the pressure rise. One would expect that the higher the temperature the more evaporation will occur and thus there should have been an inverse outcome (i.e. positive correlation). However there can be an alternative explanation if one considers the location of the temperature sensor.

The sensor is located on top of the tank right next to the helium inlet. This is a region were liquid is hard to reach and this can only be achieved if there is intense sloshing taking place (i.e. high breaking waves/splashing). During unstable sloshing the chance of liquid reaching the top of the tank is higher, thus higher is the chance of affecting the region adjacent the temperature sensor. Considering the above, high magnitude sloshing will lead to a lower maximum ullage temperature and in the same time to a higher pressure drop. This can be supported by the fact that the acceleration and the roll rates have a negative correlation to the maximum temperature as well (see Table 3.2.2).

Another explanation can be also the fact that the maximum temperature is connected to the ullage volume. A high ullage volume will require more helium to achieve the same pressurization level. Due to the higher amount of helium inserted into the tank, the ullage temperature can be sufficiently higher. This can be also supported by the fact that these two parameters are highly collinear as shown in Figure 4.2.13.

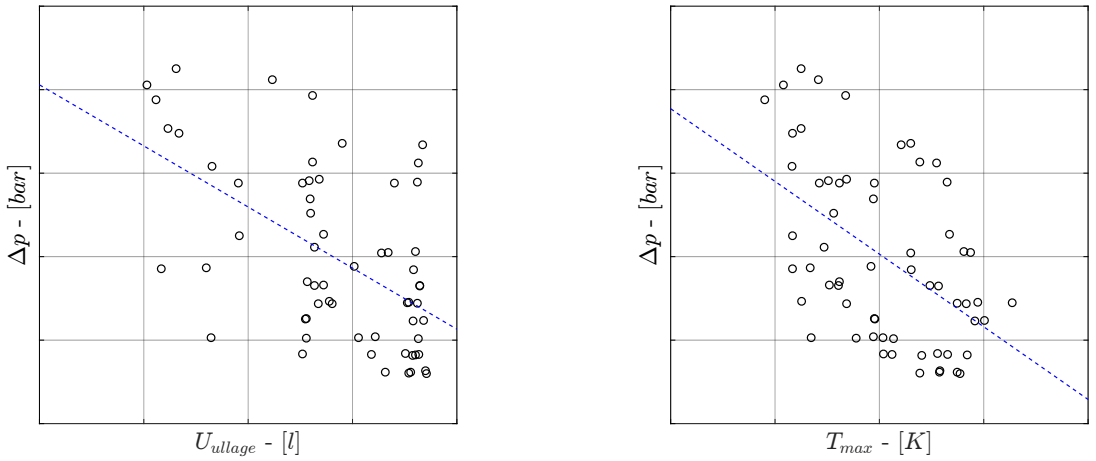

(a) Ullage volume vs Pressure rise - $R = -0.552$

(b) Maximum ullage temperature vs Pressure rise - $R = -0.509$

Figure 4.2.12: Correlation of ullage volume and maximum ullage temperature to the pressure rise of the LO_x tank.

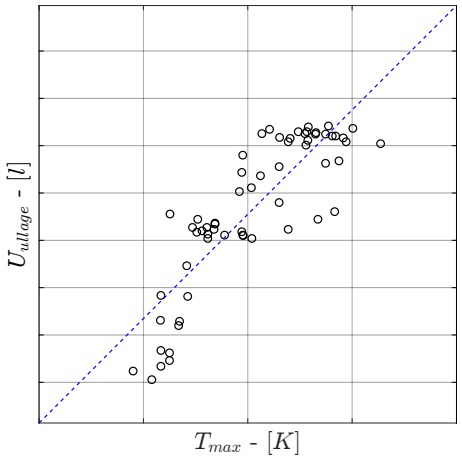

Figure 4.2.13: Collinearity of ullage volume and maximum ullage temperature of the LO_x tank - $R = 0.855$

Regarding the conditions in the LH_2 tank, the ullage volume did not show any correlation to the pressure drop. The mass of the liquid hydrogen that is loaded into the tank is similar for all of the flights, thus it can be concluded that in this case, the ullage volume does not play any role in the magnitude of the pressure drop.

The maximum ullage temperature of the whole dataset (61 flights) also showed a weak negative correlation ($R = -0.261$). The correlation is stronger ($R = 0.688$) when it comes to the ullage temperature drop, however the fact that only 8 out of the 61 flights show a temperature drop makes this approach insufficient. These are the flights F001, F005, F009, F018, F024, F037, F038 and F050.

By studying only those 8 flights, the correlation of the temperature drop becomes stronger ($R = 0.831$) as shown in Figure 4.2.14. It is also the correlation coefficient of the roll rate that increases. This can be a clue that on those 8 flights high magnitude sloshing occurs however, the number of instances and predictors is not sufficient to build a reliable statistical model.

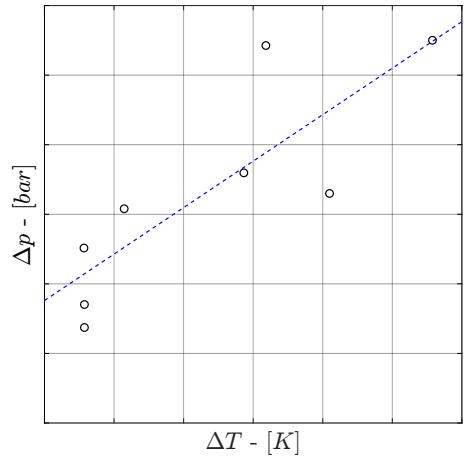

Figure 4.2.14: Temperature drop correlation to the LH_2 tank pressure drop for the group of the 8 flights - $R = 0.831$

Finally, as shown in Section 4.2.1, the flights with a recorded high temperature drop constitute the outliers of the kinematic correlation approach. It is clear that the temperature drop is caused by the formation of high magnitude chaotic waves which reach the top of the ullage. The effect on pressure of such high magnitude waves, could not be depicted in the kinematic magnitude analysis approach.

4.2.4. Statistical prediction

The statistical model that is chosen is Model 7 of Table 3.2.5. This model includes 3 predictors which are the acceleration profile, the roll rate profile and the ullage volume. The reason that this model is preferred over model 4 which showed slightly better performance, is that it includes the ullage volume as a predictor and subsequently offers the possibility to predict the pressure rise based on the actual tank loading. The response, Δp, is expressed through Equation (4.2.2)

$$\Delta p = \beta_0 + \beta_1 Accel_{-yz} + \beta_2 Roll_{-y} + \beta_3 U_{ullage} \tag{4.2.2}$$

The outcome of the multiple linear regression is presented in Table 4.2.2. The model agrees with the individual positive correlations of the acceleration and the roll rate profiles, and the negative correlation of the ullage volume. The ANOVA table is presented in Table 4.2.3.

Table 4.2.2: Multiple linear regression results of LO_x tank.

Param.	Coeff.	Std. Error	t-stat	p-value
$Accel_{-yz}$ (β_1)	0.037470	0.015218	2.462148	0.016858
$Roll_{-y}$ (β_2)	0.379858	0.096012	3.956344	0.000213
U_{ullage} (β_3)	-0.000041	0.000066	-0.632783	0.529406
Intercept (β_0)	0.066491	0.050086	1.327525	0.189627

Table 4.2.3: ANOVA table for ΔP prediction model

ANOVA	deg. of freedom	SS	MS	F	p-value
Regression	3	0.1125	0.0375	40.749	$<< 0.01$
Residual	57	0.0524	0.0009		
Total	60	0.1649			

The idea now is to calculate the the ”worst” and the ”best” case scenarios with 99% confidence level. That would be a prediction using extreme values for the independent variables. For the worst case approach it will be required to use the maximum calculated magnitude change for acceleration and roll, and the minimum observed ullage volume. The best case scenario will be the one with the highest up to now ullage volume and the lowest kinematic profile change. Finally, it is worth investigating the case were the maximum kinematic profile change is present and the theoretically minimum ullage volume (i.e. maximum loading) exists.

The prediction intervals (lower and upper) for the case of a multiple linear regression for 99% confidence level are calculated through Equation (4.2.3)

$$\hat{y}_p \pm t_{(0.01,df)} \sqrt{\hat{\sigma^2}(1 + x_p^{'}(X^{'}X)^{-1}x_p)} \tag{4.2.3}$$

where $df = 57$ are the degrees of freedom, $t_{(0.01,df)} = 2.6649$ is the t-test coefficient corresponding to the confidence level and the degrees of freedom (taken from statistical tables), $\sigma^2 = 0.0009$ is the error mean square (obtained from the ANOVA table), x_p is a 4x1 table containing the predictor values for the worst or the best case scenario. Equations (4.2.4) and (4.2.5) are based on the up to date observed conditions while Equation (4.2.6) refers to the theoretically minimum ullage volume case.

$$x_{p,worst} = \begin{bmatrix} 1 \\ max(Accel_{-yz}) \\ max(Roll_{-y}) \\ min(U_{ullage}) \end{bmatrix} \tag{4.2.4}$$

$$x_{p,best} = \begin{bmatrix} 1 \\ min(Accel_{-yz}) \\ min(Roll_{-y}) \\ max(U_{ullage}) \end{bmatrix} \tag{4.2.5}$$

$$x_{p,worst,theor.} = \begin{bmatrix} 1 \\ max(Accel_{-yz}) \\ max(Roll_{-y}) \\ min(U_{ullage})_{theor} \end{bmatrix} \tag{4.2.6}$$

Finally, the X is a 61x4 table (also called design table). The first column is a ”ones” column while the rest three correspond to the three predictors and the observations.

Table 4.2.4: Upper prediction limits of the percentile pressure rise, for 99% confidence level

	Best case	**Worst case**	**Worst case (theor.)**
$\hat{y}_p$	1.67%	10.28%	10.44%
$\hat{y}_{p,upper}$	5.68%	14.45%	14.73%

As already known, pressure always shows a rising behavior inside the LO_x tank, thus we are only interested in the upper prediction limits. The results for the worst/best case scenarios (for 99% confidence level) are listed in Table 4.2.4 According to the statistical model, there is 99% chance that the pressure rise will not exceed 5.68% for the best case (highest ullage volume - zero acceleration/roll sudden change), 14.45% for the worst case (lowest ullage volume - maximum acceleration/roll sudden change) and 14.73% for the worst theoretical case. The corresponding analysis refers to the LO_x tank during the ascent phase of the Ariane 5 launcher.

"We must free ourselves of the hope that the sea will ever rest. We must learn to sail in high winds."

-Aristotle Onassis, Shipping Magnate, 1906-1975 AD

5

Conclusion

There was an effort to explain the cause and predict the magnitude of the pressure fluctuations that take place inside the upper stage cryogenic tanks of Ariane 5 launcher during the ascent phase. A literature study was initially conducted in order to review the state of the art and gain understanding on the pressure change phenomenon as well as on the parameters that affect its evolution. A series of CFD simulations were then conducted based on 7 launcher past flights (high/low pressure change flights), aiming to estimate the sloshing angle evolution inside the cryogenic LO_x and LH_2 tanks and attempting to find possible connection to the periods of the pressure change. Finally, parameters like the acceleration and the roll rates of the launcher, tank temperature and pressure, tank ullage volume and vibrations, of 61 past flights of Ariane 5 were also analyzed and an attempt to predict the final tank pressure was made.

CFD discussion

The outcome of the CFD simulations showed that breaking waves exists in most of the cases where the sloshing angle exceeds $15\,deg$.

For the LO_x tank there is clear evidence that the high pressure rise periods are accompanied by high sloshing angles (over $15\,deg$). In the low pressure rise LO_x cases the sloshing angle magnitude hardly exceeds $5\,deg$.

The sloshing angle magnitude for most cases can be positively correlated to the pressure rise inside the tanks. Flight F060 is an exception, as despite the high pressure rise that is recorded, relatively low sloshing angle magnitude is present and no strong waves creation is noticed. This deviating behavior can be attributed to the significantly lower ullage volume of this specific flight (one of the lowest so far) which despite the low sloshing amplitude leads to a noticeable pressure rise inside the LO_x tank.

Finally, regarding the LO_x tank simulations, there is no clear indication of high sloshing amplitude near the so called acceleration-induced pressure rise which is more likely to happen due to the longitudinal acceleration decay after the solid boosters' burnout.

The CFD simulations of the sloshing angle of the LH_2 tank did not show so clear correlation of the angle to the pressure drop. The most characteristic examples are those of flights F009 and F050. These are two flights showing identical recorded pressure behavior during the ascent phase. However, the simulation showed, that high sloshing angles and breaking/splashing waves exist only in flight F009. Despite the increased sloshing magnitude that flight F050 shows during the pressure drop period, no intense waves are formed and thus, the sloshing magnitude resulting from the CFD simulation, can not relate to the

recorded pressure change. This is a first indication that there could be another parameter (other than acceleration or roll) that additionally effects the kinematics of the LH_2.

Furthermore, in the LH_2 case, increased sloshing duration was also noticed for flights with a recorded pressure drop when compared to no pressure drop flights.

The CFD post-processing showed that the LH_2 tank appeared to be more prone to the formation of breaking/splashing waves than the LO_x one. More specifically, the breaking waves that are formed in the LH_2 tank cause more excessive splashing and their duration is longer.

Summing up, it is evident that in general, increased sloshing magnitude is noticed near the regions of pressure change. This is more evident in the case of LH_2 tank, where most of the times high breaking waves exists. It can be therefore concluded that liquid sloshing has a strong impact on the pressure evolution inside the cryogenic tanks.

Flight data analysis discussion

The analysis of the acceleration and the roll rates profiles shows that there is strong correlation of the kinematics magnitude change to the pressure rise in the LO_x tank. The acceleration change at individual -x, -y, -z axes showed a weak correlation coefficient (correlation to the pressure rise). The same holds for the roll rates around individual -x and -z axes. The strongest correlation is obtained for the combined -yz acceleration change magnitude and for the roll rate change magnitude around -y axis.

The optimization process showed that the period of strongest correlation starts and ends slightly earlier for the case of the roll rate change when compared to the acceleration. This indicates that the effect of the launcher roll on the pressure change onsets earlier. Both cases show high correlation coefficients, 0.74 for the acceleration and 0.81 for the roll.

The small pressure rise (< 5%) which is recorded right at the time of solid boosters' burnout (i.e. acceleration decay) is accompanied by a recorded fill level rise of $2-3\,mm$. This is evident at low sloshing magnitudes and while no other significant pressure change takes place. This level rise can be probably attributed to the liquid oxygen's compressibility. This small level rise will in turn lead to the small pressure rise which is mentioned above.

The ullage volume (U_{ullage}) of the LO_x tank shows a quite strong negative correlation to the recorded pressure rise (R = -0.552). The maximum ullage temperature follows an identical behavior (R = - 0.509). It is more likely that higher ullage volumes will lead to lower pressure rise inside the LO_x tank. This can also be supported by the fact that the impact of evaporation to the pressure, is more significant in smaller ullage volumes. The existing collinearity between the ullage volume and the maximum temperature can be attributed to the fact that larger volumes require more helium to achieve the same pressurization, thus higher temperatures will be present.

There is no clear indication of correlation of the initial tank pressure (p_{init}) and temperature (T_{init}) to the magnitude of the pressure rise. Both parameters demonstrated a low correlation coefficient, $R = -0.056$ and $R = -0.388$ respectively. The estimation of the helium concentration despite leading to a high correlation it is considered unreliable as there was no sufficient information about the exact helium mass flow per flight.

The prediction model that was built for the LO_x tank pressure rise, incorporating the acceleration change, the roll rate change and the ullage volume, showed a 99% chance that the percentile pressure rise will not exceed 14.73% for the theoretical worst case scenario. The maximum predicted pressure rise lies within the threshold of the relief valve, which is expected to be activated in this case. Encouragingly, the predicted value is below the sizing pressure limit of the tank, in the case of a relief-valve failure.

Regarding the LH_2 tank, the initial ullage pressure (p_{init}) and temperature (T_{init}) , the

pressure drop start-time ($t_{P_{init}}$) and the maximum ullage temperature (T_{max}) showed extremely weak correlation to the ullage pressure drop magnitude. It can be concluded that these parameters do not affect the ullage pressure evolution of the LH_2 tank.

The correlation of the kinematic profile of the launcher to the pressure drop magnitude of the LH_2 tank is also not sufficient. The correlation coefficient lies below 0.5 for both the acceleration and the roll rate magnitude change. There is no clear indication of the connection of the kinematics of the launcher to the pressure drop magnitude.

By not including the 5 steep pressure drop outliers in the approach, sufficiently stronger correlation is achieved. The coefficients increase to $R = 0.802$ for the acceleration and $R = 0.735$ for the roll.

The steep pressure drop (accompanied by temperature drop recorded by the top sensor) can be attributed to the creation of strong breaking/splashing waves (as shown in F009 LH_2 tank). It can be concluded that the creation of those strong waves can not be depicted in the kinematic profile of the launcher and is in a way uncertain. In other words, the acceleration/roll rate change magnitude is capable to describe the gradual/smooth LH_2 tank ullage pressure drop (high correlation) however it is insufficient for the prediction of the steep pressure drop which is probably caused by strong chaotic waves.

The data analysis and the CFD simulations, showed that the formation of strong waves can not be solely described by the sudden change of the acceleration and the roll rate magnitude (data analysis) nor by the combined effect of the two components (CFD). It should be attributed to a different factor.

This factor could be the tank vibrations. Tank vibrations near the natural frequency region of the LH_2 tank ($f_n = 0.8\,Hz$) have been observed for flight F050 where no breaking waves were shown through the CFD simulation. Although this approach was based on approximations, vibrations may ultimately be the influential factor for the explanation of the steep pressure drop and the formation of breaking waves inside the LH_2 tank.

It can be concluded that there is not sufficient data for the creation of a prediction model of the LH_2 tank ullage pressure drop magnitude.

Future work

The behavior of pressure in the two tanks is not identical. For the LH_2 tank pressure an evident pressure drop (condensation) precedes the pressure rise (evaporation). In the case of the LO_x tank, the pressure drop is slightly or not noticeable at all, instead, a pressure rise is in most of the cases only recorded. Initial conditions (pressure,temperature) should play an important role in this deviating behavior however it is believed that this is also caused by the different mixing (with Helium) of the gaseous components inside the ullage (due to different densities), affecting that way the partial pressures of the gaseous oxygen and hydrogen. This is already obvious from the ground-pressurization process where the evolution of pressure already differs for the two tanks.

One suggested approach to investigate the effect of tank pressurization and mixing is to attempt to simulate the pressurization of both tanks in order to have a clear view on how they mix with GHe. At the end of the pressurization, it is also possible to apply the acceleration of the launcher in order to see how the different density components behave under such conditions.

Despite that for the LO_x there is an agreement of the CFD outcome to the pressure behavior (i.e. recorded pressure rise is always accompanied by high sloshing angles) this is not the case for the LH_2. It is believed that sudden pressure drops in this tank are mainly caused by breaking/splashing waves, however this could not be shown for F050. An estimation of the effect of vibration frequencies showed that they could potentially favor the creation of breaking waves inside the tank. Therefore, the incorporation of the vibrations inside the

CFD model could possibly provide more insight regarding their effect.

Finally, the incorporation of a cluster computer will allow to further decrease the cell size and tighten the convergence criteria. In this way, accuracy could be higher and the small volume errors could be avoided. Although the use of a cluster will probably not change much in the simulation accuracy of the purely kinematic approach, it will enable the use of a full thermodynamic model for both ground pressurization and sloshing, including the effects of heat transfer and phase change.

Bibliography

3D CAD Browser. Ariane 5 3D CAD model, 2018. URL https://www.3dcadbrowser.com/download.aspx?3dmodel=41802. accessed 18-01-2018.

Arianespace. Ariane 5 user's manual. (Issue 5 Revision 2), 2016.

Arianespace. Arianespace orbits four more Galileo satellites as Ariane 5 logs 82nd successful launch in a row., 2017. URL https://goo.gl/dZ6gBF. accessed 18-01-2018.

Arndt, T. *Sloshing of cryogenic liquids in a cylindrical tank under normal gravity conditions*. PhD thesis, University of Bremen, 2011.

Arndt, T., Dreyer, M., Behruzi, P., and Winter, M. Laterally excited sloshing tests with liquid nitrogen LN2. In *44th AIAA/ASME/SAE/ASEE Joint Propulsion Conference & Exhibit*. American Institute of Aeronautics and Astronautics, 7 2008. doi: 10.2514/6.2008-4551. URL dx.doi.org/10.2514/6.2008-4551.

Arndt, T., Dreyer, M., Behruzi, P., Winter, M., and Van Foreest, A. Cryogenic sloshing tests in a pressurized cylindrical reservoir. In *45th AIAA/ASME/SAE/ASEE Joint Propulsion Conference & Exhibit*, 8 2009. doi: 10.2514/6.2009-4860. URL dx.doi.org/10.2514/6.2009-4860.

Arndt, T. O. and Dreyer, M. E. Damping behavior of sloshing liquid in laterally excited cylindrical propellant vessels. *Journal of Spacecraft and Rockets*, 45(5):1085–1088, 9 2008. ISSN 0022-4650. doi: 10.2514/1.35019. URL dx.doi.org/10.2514/1.35019.

Aydelott, J. C. Normal gravity self-pressurization of 9-inch- (23 CM) diameter spherical liquid hydrogen tankage. NASA TN-D-4171. Technical report, NASA Lewis Research Center, Cleveland, Ohio, 1967.

Aydelott, J. C. Effect of size on normal gravity self-pressurization of spherical liquid hyrdogen tankage. NASA TN D-5196. Technical report, NASA Lewis Research Center, Cleveland, Ohio, 1969.

Cariou, A. and Casella, G. Liquid sloshing in ship tanks: A comparative study of numerical simulation. *Marine Structures*, 12(3):183–198, 1999. ISSN 0951-8339. doi: 10.1016/S0951-8339(99)00026-X. URL dx.doi.org/10.1016/S0951-8339(99)00026-X.

Das, S. P. and Hopfinger, E. J. Mass transfer enhancement by gravity waves at a liquid-vapour interface. *International Journal of Heat and Mass Transfer*, 52(5–6):1400–1411, 2009. ISSN 00179310. doi: 10.1016/j.ijheatmasstransfer.2008.08.016. URL dx.doi.org/10.1016/j.ijheatmasstransfer.2008.08.016.

ESA. Ariane 6, 2017. URL https://www.esa.int/Our_Activities/Space_Transportation/Launch_vehicles/Ariane_6.

Etkin, B. *Dynamics of Flight - Stability and Control*. WILEY, 2nd edition, 1982. ISBN 0-471-08936-2.

Godderidge, B., Tan, M., Turnock, S., and Earl, C. A verification and validation study of the application of computational fluid dynamics to the modelling of lateral sloshing. Project report, University of Southampton, 2006. URL https://eprints.soton.ac.uk/42931/.

Godderidge, B., Turnock, S., Tan, M., and Earl, C. An investigation of multiphase CFD modelling of a lateral sloshing tank. *Computers and Fluids*, 38(2):183–193, 2009. ISSN 0045-7930. doi: 10.1016/j.compfluid.2007.11.007. URL dx.doi.org/10.1016/j.compfluid.2007.11.007.

Hanley, H., McCarty, R., and Haynes, W. The viscosity and thermal conductivity coefficients for dense gaseous and liquid argon, krypton, xenon, nitrogen, and oxygen. *Journal of Physical and Chemical Reference Data*, 3(4):979–1017, 1974. ISSN 00472689. doi: 10.1063/1.3253152. URL dx.doi.org/10.1063/1.3253152.

Hasan, M. M., Lin, C. S., and Van Dresar, N. Self-pressurization of a flightweight liquid hydrogen storage tank subjected to low heat flux. NASA TM 103804. Technical report, 1991.

Hirt, C. W. and Barkhudarov, M. R. Void regions and bubble models in FLOW-3D. Technical report, Flow Science, Inc., 2013.

Hirt, C. W. and Nichols, B. D. Volume of fluid (VOF) method for the dynamics of free boundaries. *Journal of Computational Physics*, 39(1):201–225, 1981. ISSN 10902716. doi: 10.1016/0021-9991(81)90145-5.

Hoge, H. J. Vapor pressure and fixed points of oxygen and heat capacity in the critical region. *Journal of Research of the National Bureau of Standards*, 44:321–345, 1950. URL archive.org/details/jresv44n3p321.

Hoge, H. J. and Arnold, R. D. Vapor pressures of hydrogen, deuterium, and hydrogen deuteride and dew-point pressures of their mixtures. *Journal of Research of the National Bureau of Standards*, 47(2):63–74, 1951. ISSN 0091-0635. doi: 10.6028/jres.047.009. URL dx.doi.org/10.6028/jres.047.009.

J.Hord, R. and H.M.Roder. *Selected properties of Hydrogen*. Center of Chemical Engineering, National Engineering Laboratory, National Bureau of Standards, Boulder,CO, 1981.

Joseph, J., Agrawal, G., Agarwal, D. K., and Kumar, S. S. Analytical study on the effect of ullage temperature and helium concentration on cryogenic tank pressure during sloshing. In *25th National Symposium on Cryogenics*, 2014.

Joshi, A. Y., Bansal, A., and Rakshit, D. Effects of Baffles on Sloshing Impact Pressure of a Chamfered Tank. *Procedia Engineering*, 173:940–947, 2017. ISSN 18777058. doi: 10.1016/j.proeng.2016.12.150. URL dx.doi.org/10.1016/j.proeng.2016.12.150.

Kim, K. H., Ko, H. J., Kim, K., Jung, Y. S., Oh, S. H., and Cho, K. J. Transient thermal analysis of a cryogenic oxidizer tank in the liquid rocket propulsion system during the prelaunch helium gas pressurization. *Journal of Engineering Thermophysics*, 21(1):1–15, 2012. ISSN 1990-5432. doi: 10.1134/S1810232812010018. URL dx.doi.org/10.1134/S1810232812010018.

Kumar, S. P., Prasad, B. V. S. S. S., Venkatarathnam, G., Ramamurthi, K., and Murthy, S. S. Influence of surface evaporation on stratification in liquid hydrogen tanks of different aspect ratios. *International Journal of Hydrogen Energy*, 32(12):1954–1960, 2007. ISSN 03603199. doi: 10.1016/j.ijhydene.2006.08.052. URL dx.doi.org/10.1016/j.ijhydene.2006.08.052.

Lacovic, R. F. Comparison of experimental and calculated helium requirements for pressurization of a Centaur liquid oxygen tank. NASA TM X-2013. Technical report, Lewis Research Center, Cleveland, Ohio, 1970.

Lin, C. and Hasan, M. Self-pressurization of a spherical liquid hydrogen storage tank in a microgravity environment. In *30th Aerospace Sciences Meeting and Exhibit*, Reno, Nevada, 1 1992. American Institute of Aeronautics and Astronautics. doi: 10.2514/6.1992-363. URL dx.doi.org/10.2514/6.1992-363.

Liu, Z., Li, Y., and Jin, Y. Pressurization performance and temperature stratification in cryogenic final stage propellant tank. *Applied Thermal Engineering*, 106:211–220, 2016. ISSN 13594311. doi: 10.1016/j.applthermaleng.2016.05.195. URL dx.doi.org/10.1016/j.applthermaleng.2016.05.195.

Liu, Z., Li, Y., Jin, Y., and Li, C. Thermodynamic performance of pre-pressurization in a cryogenic tank. *Applied Thermal Engineering*, 112:801–810, 2017. ISSN 13594311. doi: 10.1016/j.applthermaleng.2016.10.124. URL dx.doi.org/10.1016/j.applthermaleng.2016.10.124.

Ludwig, C. and Dreyer, M. E. Analyses of cryogenic propellant tank pressurization based upon ground experiments. In *AIAA SPACE 2012 Conference & Exposition*, Pasadena, California, 2012. doi: 10.2514/6.2012-5199. URL dx.doi.org/10.2514/6.2012-5199.

Ludwig, C. and Dreyer, M. E. Investigations on thermodynamic phenomena of the active-pressurization process of a cryogenic propellant tank. *Cryogenics*, 63:1–16, 2014. ISSN 00112275. doi: 10.1016/j.cryogenics.2014.05.005. URL dx.doi.org/10.1016/j.cryogenics.2014.05.005.

Ludwig, C., Dreyer, M. E., and Hopfinger, E. J. Pressure variations in a cryogenic liquid storage tank subjected to periodic excitations. *International Journal of Heat and Mass Transfer*, 66:223–234, 2013. ISSN 00179310. doi: 10.1016/j.ijheatmasstransfer.2013.06.072. URL dx.doi.org/10.1016/j.ijheatmasstransfer.2013.06.072.

Miles, J. W. Resonantly forced surface waves in a circular cylinder. *Journal of Fluid Mechanics*, 149:15–31, 1984. ISSN 0022-1120. doi: DOI:10.1017/S0022112084002512. URL dx.doi.org/10.1017/S0022112084002512.

Montsarrat, C. Fluid motion analysis of the cryogenic tanks of the upper stage of Ariane 5 during the ascent phase. Master's thesis, KTH Royal Institute of Technology, 2017.

Moran, M. E., Mcnelis, N. B., Kudlac, M. T., Haberbusch, M. S., Satomino, G. A., and Satornino, G. A. Experimental results of hydrogen slosh in a 62 cubic foot (1750 liter) tank. In *30th AIAA/ASME/SAE/ASEE Joint Propulsion Conference*, Indianapolis, Indiana, 1994. doi: 10.2514/6.1994-3259. URL dx.doi.org/10.2514/6.1994-3259.

Moses, J. L. and Nein, M. Evaluation of propellant sloshing on pressurant requirement for large scale cryogenic containers. In *Cryogenic Engineering Conference*, Los Angeles, CA, 1962.

Nein, M. and Thompson, J. Experimental and analytical studies of cryogenic propellant tank pressurant requirements: NASA TN D-3177. Technical report, George C. Marshall Space Flight Center, Huntsville, AL, USA, 1966.

Nein, M. E. and Head, R. R. Experiences with pressurized discharge of liquid oxygen from large flight vehicle propellant tanks. In Timmerhaus, K. D., editor, *Advances in Cryogenic Engineering*, volume 7, pages 244–250. Springer US, Boston, MA, 1962. ISBN 978-1-4757-0531-7. doi: 10.1007/978-1-4757-0531-7_30. URL dx.doi.org/10.1007/978-1-4757-0531-7_30.

Seo, M. and Jeong, S. Analysis of self-pressurization phenomenon of cryogenic fluid storage tank with thermal diffusion model. 50(9):549 – 555, 2010. ISSN 0011-2275. doi: 10.1016/j.cryogenics.2010.02.021. URL dx.doi.org/10.1016/j.cryogenics.2010.02.021.

Singal, V., Bajaj, J., Awalgaonkar, N., and Tibdewal, S. CFD analysis of a kerosene fuel tank to reduce liquid sloshing. *Procedia Engineering*, 69:1365–1371, 2014. ISSN 1877-7058. doi: dx.doi.org/10.1016/j.proeng.2014.03.130. URL http://dx.doi.org/10.1016/j.proeng.2014.03.130.

Stofan, A. J., Armstead, A. L., and States., U. Analytical and experimental investigation of forces and frequencies resulting from liquid sloshing in a spherical tank. NASA TN D-1281. Technical report, NASA Lewis Research Center, Cleveland, Ohio, 1962.

Sumner, I. E. Experimental investigation of stability boundaries for planar and nonplanar sloshing in spherical tanks. NASA-TN-D-3210. Technical report, 1966.

UniversityOfWaikato. WEKA software, 2017. URL https://www.cs.waikato.ac.nz/ml/weka/.

Van Dresar, N. and Stochl, R. Pressurization and expulsion of a flightweight liquid hydrogen tank. In *29th Joint Propulsion Conference and Exhibit*, Joint Propulsion Conferences. American Institute of Aeronautics and Astronautics, 6 1993. doi: 10.2514/6.1993-1966. URL dx.doi.org/10.2514/6.1993-1966.

Van Dresar, N., Lin, C., and Hasan, M. Self-pressurization of a flightweight liquid hydrogen tank - Effectsof fill level at low wall heat flux. In *30th Aerospace Sciences Meeting & Exhibit*, Reno, Nevada, 1 1992. American Institute of Aeronautics and Astronautics. doi: 10.2514/6.1992-818. URL dx.doi.org/10.2514/6.1992-818.

Van Foreest, A. Modeling of cryogenic sloshing including heat and mass transfer. In *46th AIAA/ASME/SAE/ASEE Joint Propulsion Conference & Exhibit*. American Institute of Aeronautics and Astronautics, 7 2010. doi: 10.2514/6.2010-6891. URL dx.doi.org/10.2514/6.2010-6891.

Van Foreest, A. *Modeling of cryogenic sloshing including heat and mass transfer*. PhD thesis, University of Bremen, 2014.

Van Foreest, A., Dreyer, M., and Arndt, T. Moving two-fluid systems using the volume-of-fluid method and single-temperature approximation. *AIAA Journal*, 49(12):2805–2813, 2011. ISSN 0001-1452. doi: 10.2514/1.J050482. URL dx.doi.org/10.2514/1.J050482.

Van Itterbeek, A. and Verbeke, O. Density of liquid Nitrogen and Argon as a Function of Pressure and Temperature. *Physica*, 26(11):931–938, 1960. ISSN 0031-8914. doi: 0.1016/0031-8914(60)90042-2. URL dx.doi.org/10.1016/0031-8914(60)90042-2.

Wang, L., Li, Y., Liu, Z., and Zhu, K. Numerical investigation of thermal distribution and pressurization behavior in helium pressurized cryogenic tank by introducing a multi-component model. *Physics Procedia*, 67:392–397, 2015. ISSN 18753892. doi: 10.1016/j.phpro.2015.06.047. URL dx.doi.org/10.1016/j.phpro.2015.06.047.

Witten, I. H., Frank, E., and Hall, M. a. *Data Mining: Practical Machine Learning Tools and Techniques*. Elsevier, 2005. ISBN 0-12-088407-0.

A

Summary of CFD results

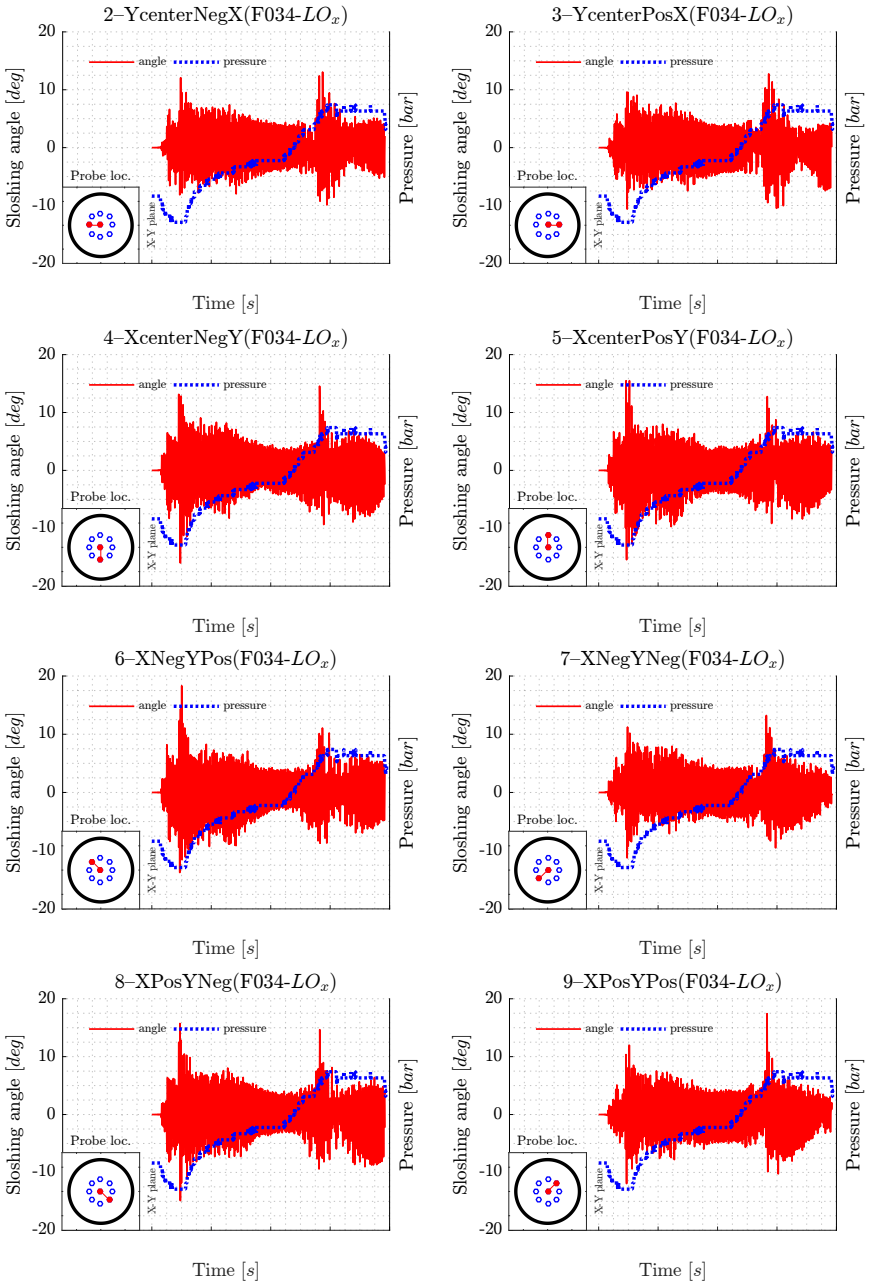

Figure A.0.1: Flight F034 LO_x sloshing angle (CFD)/pressure evolution vs Time at several tank locations

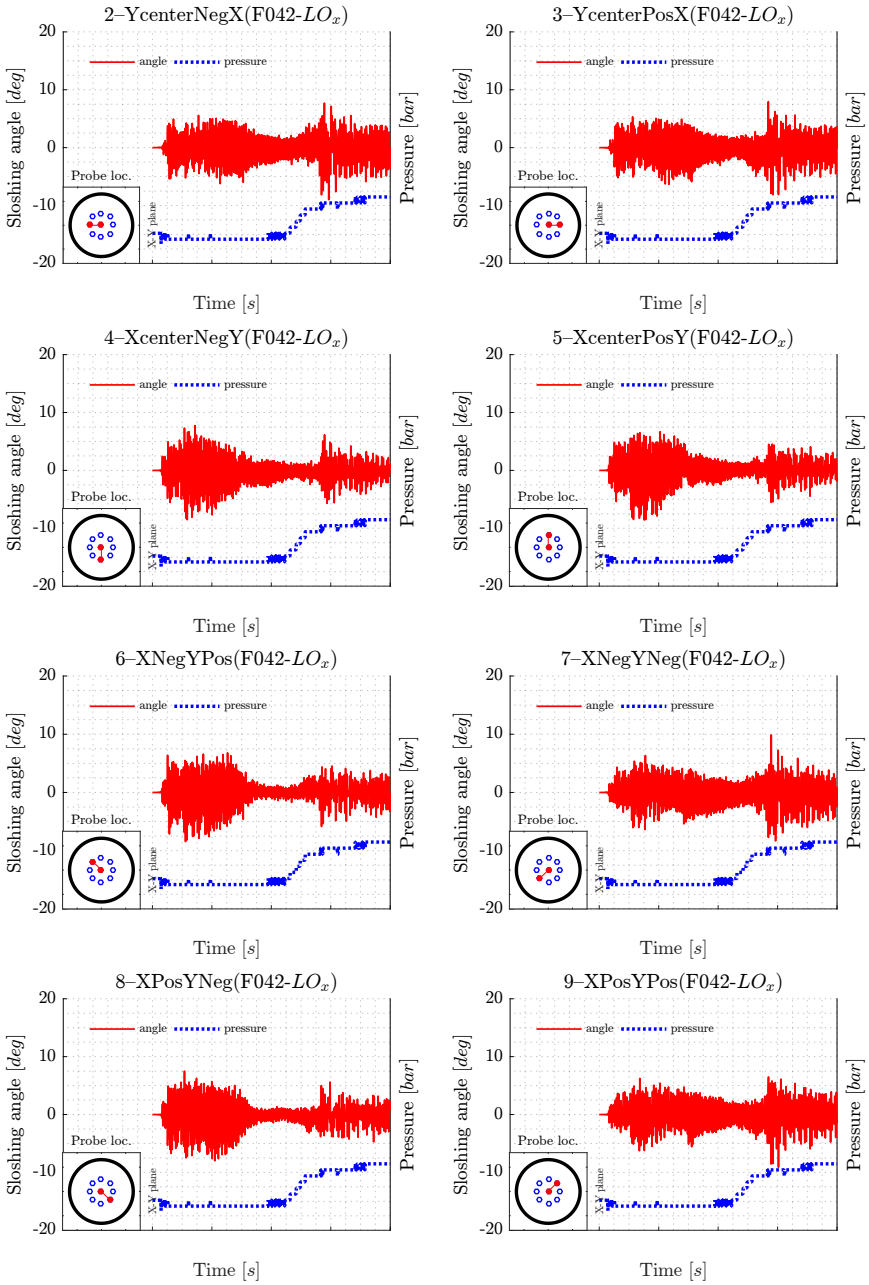

Figure A.0.2: Flight F042 LO_x sloshing angle (CFD)/pressure evolution vs Time at several tank locations

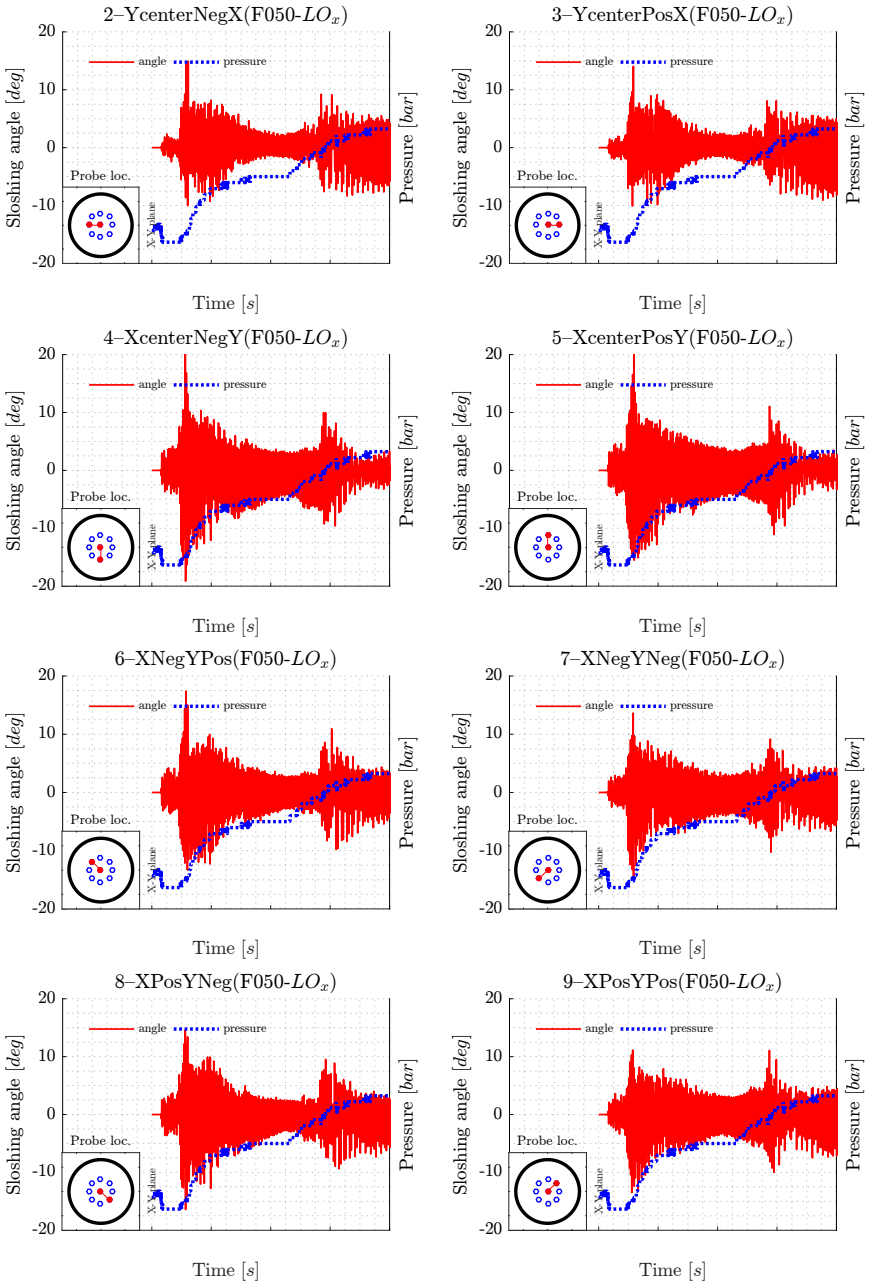

Figure A.0.3: Flight F050 LO_x sloshing angle (CFD)/pressure evolution vs Time at several tank locations

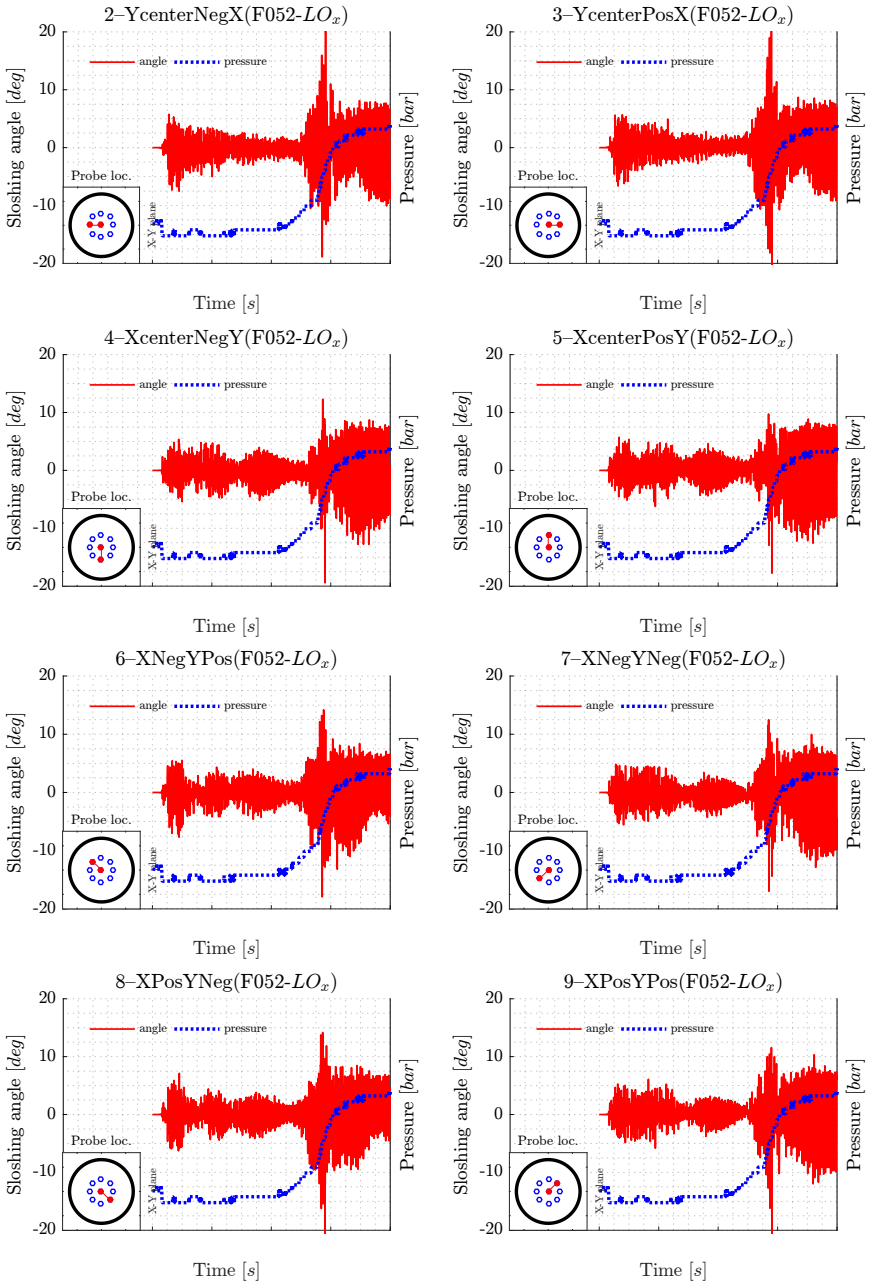

Figure A.0.4: Flight F052 LO_x sloshing angle (CFD)/pressure evolution vs Time at several tank locations

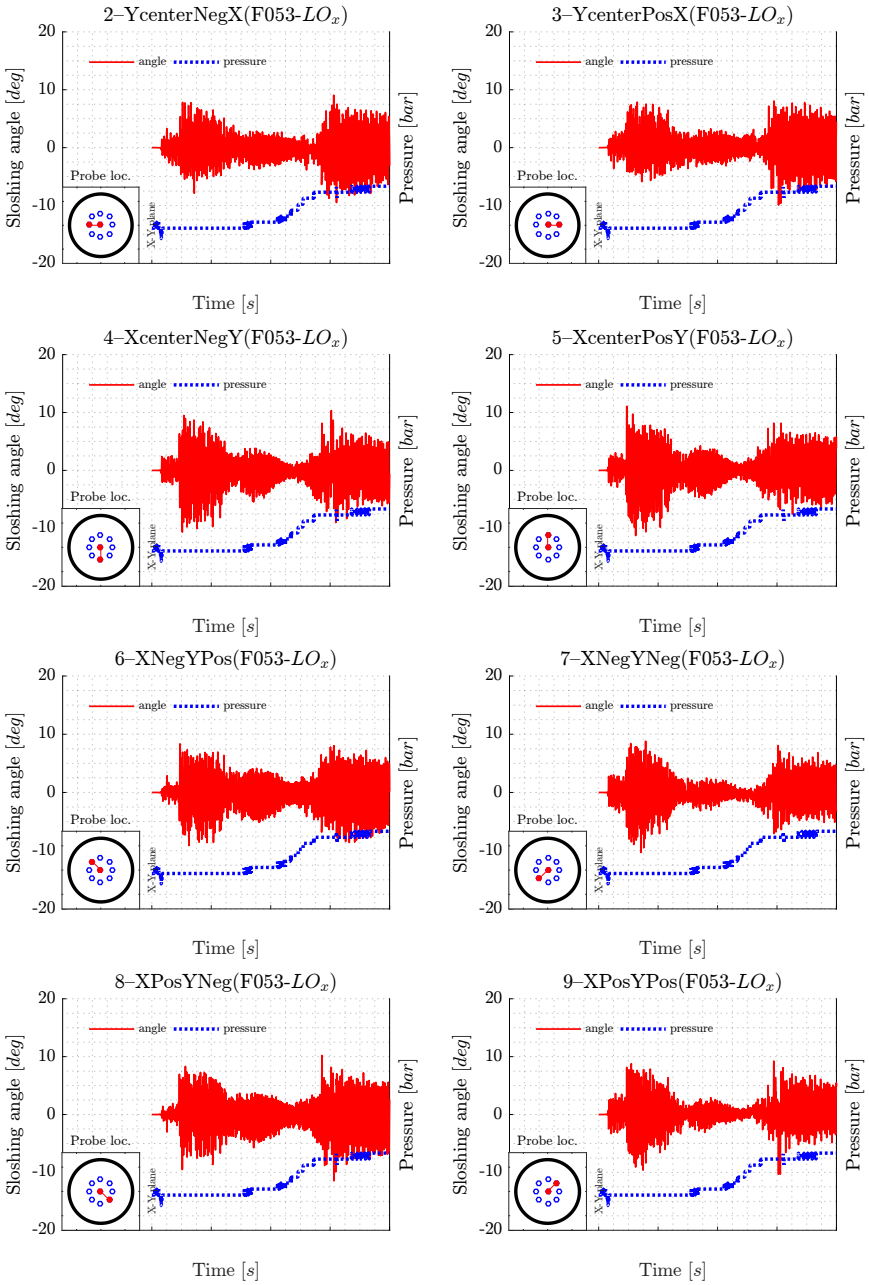

Figure A.0.5: Flight F053 LO_x sloshing angle (CFD)/pressure evolution vs Time at several tank locations

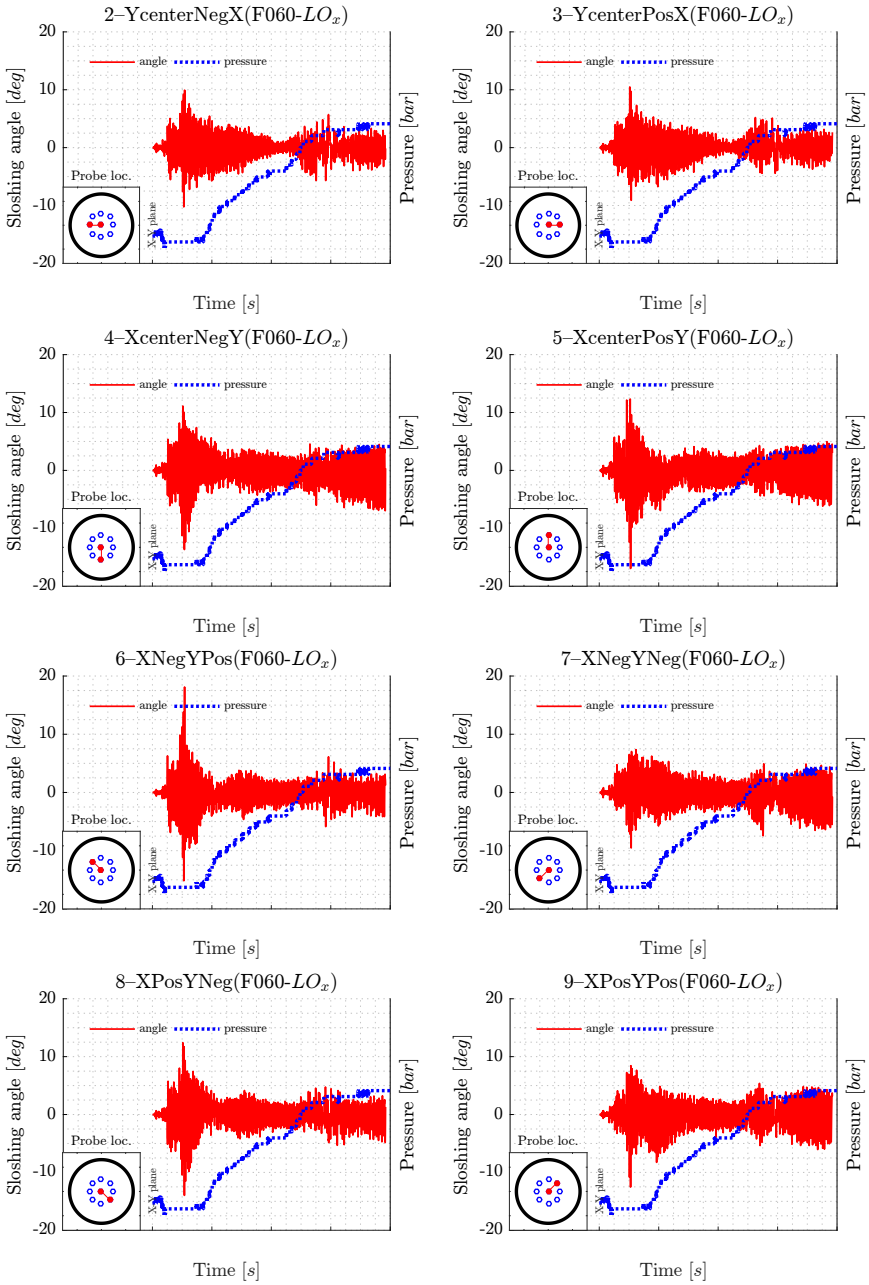

Figure A.0.6: Flight F060 LO_x sloshing angle (CFD)/pressure evolution vs Time at several tank locations

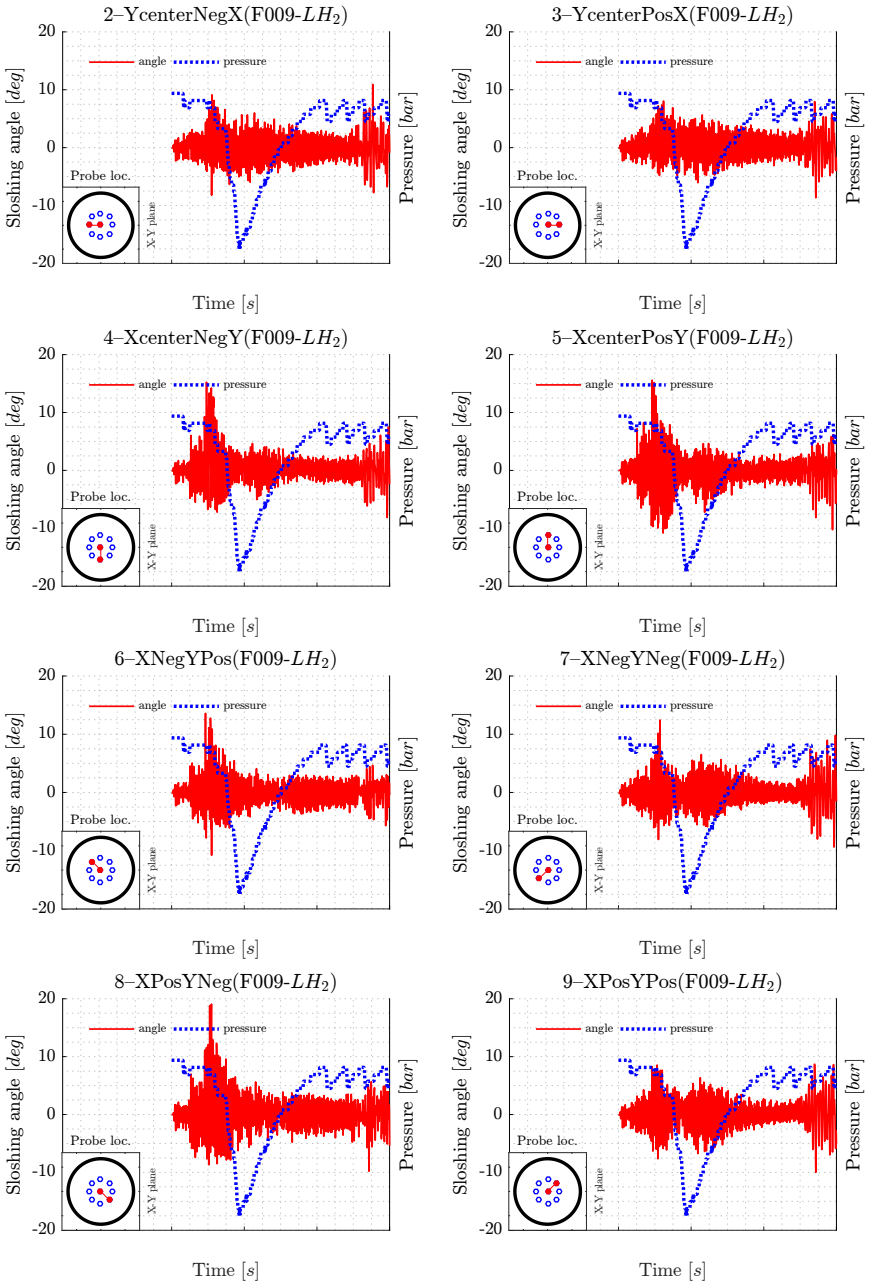

Figure A.0.7: Flight F009 LH_2 sloshing angle (CFD)/pressure evolution vs Time at several tank locations

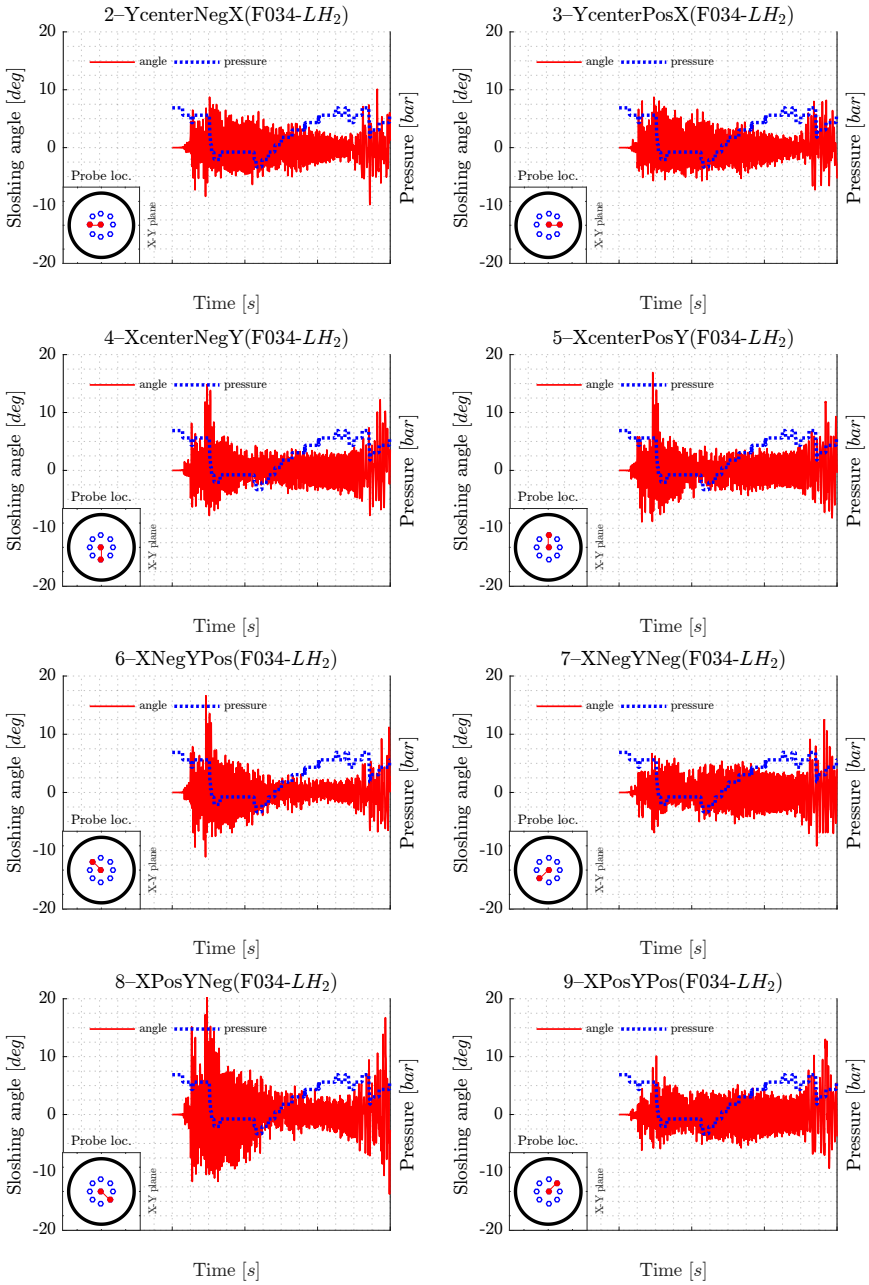

Figure A.0.8: Flight F034 LH_2 sloshing angle (CFD)/pressure evolution vs Time at several tank locations

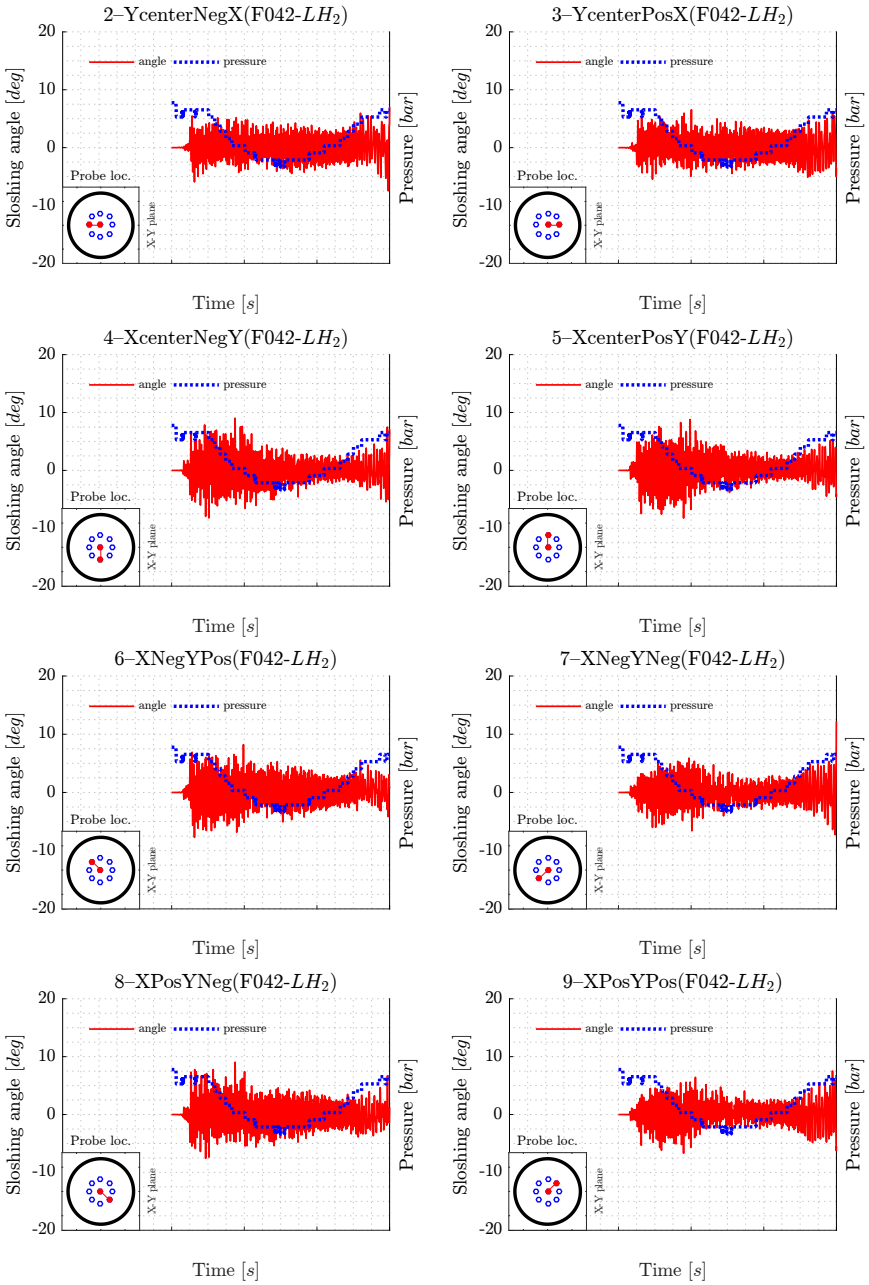

Figure A.0.9: Flight F042 LH_2 sloshing angle (CFD)/pressure evolution vs Time at several tank locations

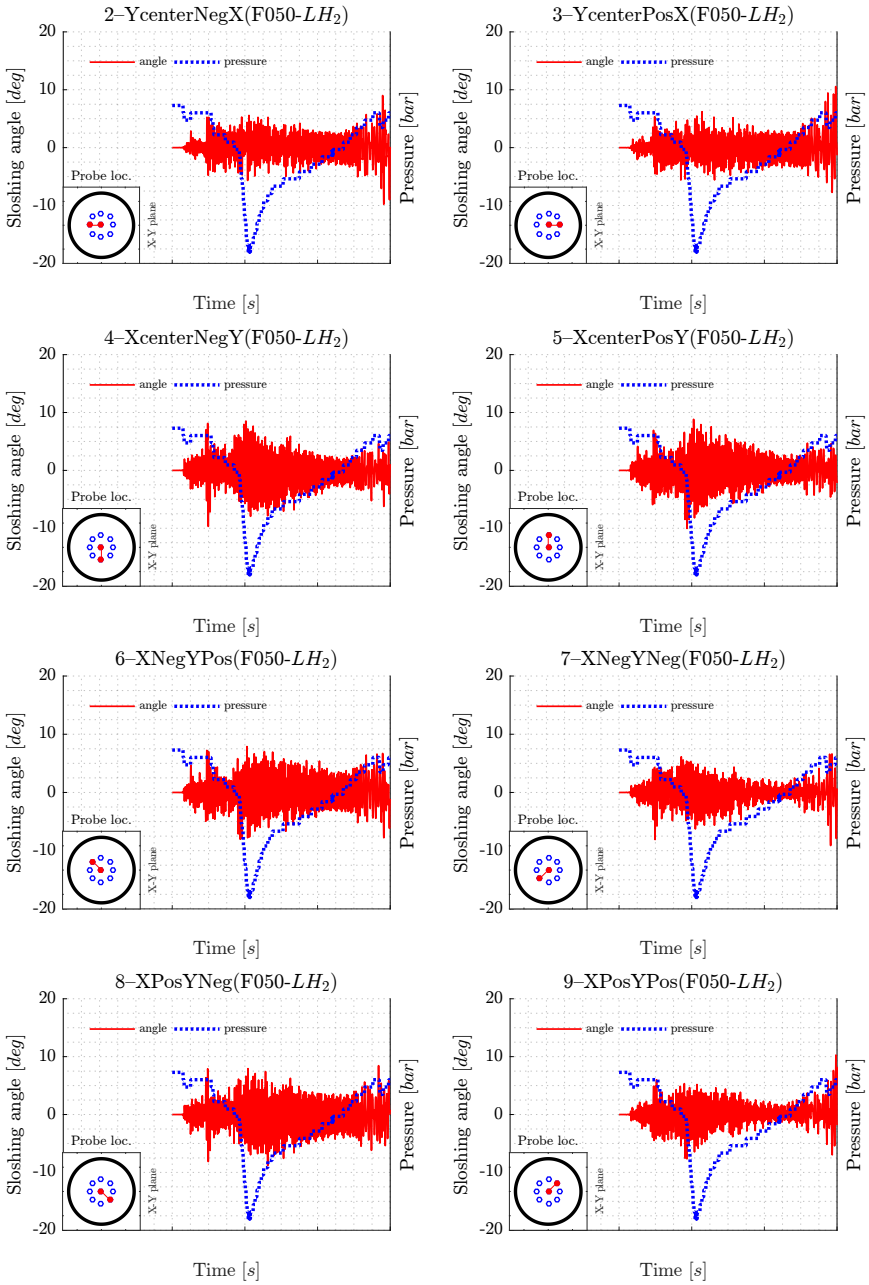

Figure A.0.10: Flight F050 LH_2 sloshing angle (CFD)/pressure evolution vs Time at several tank locations

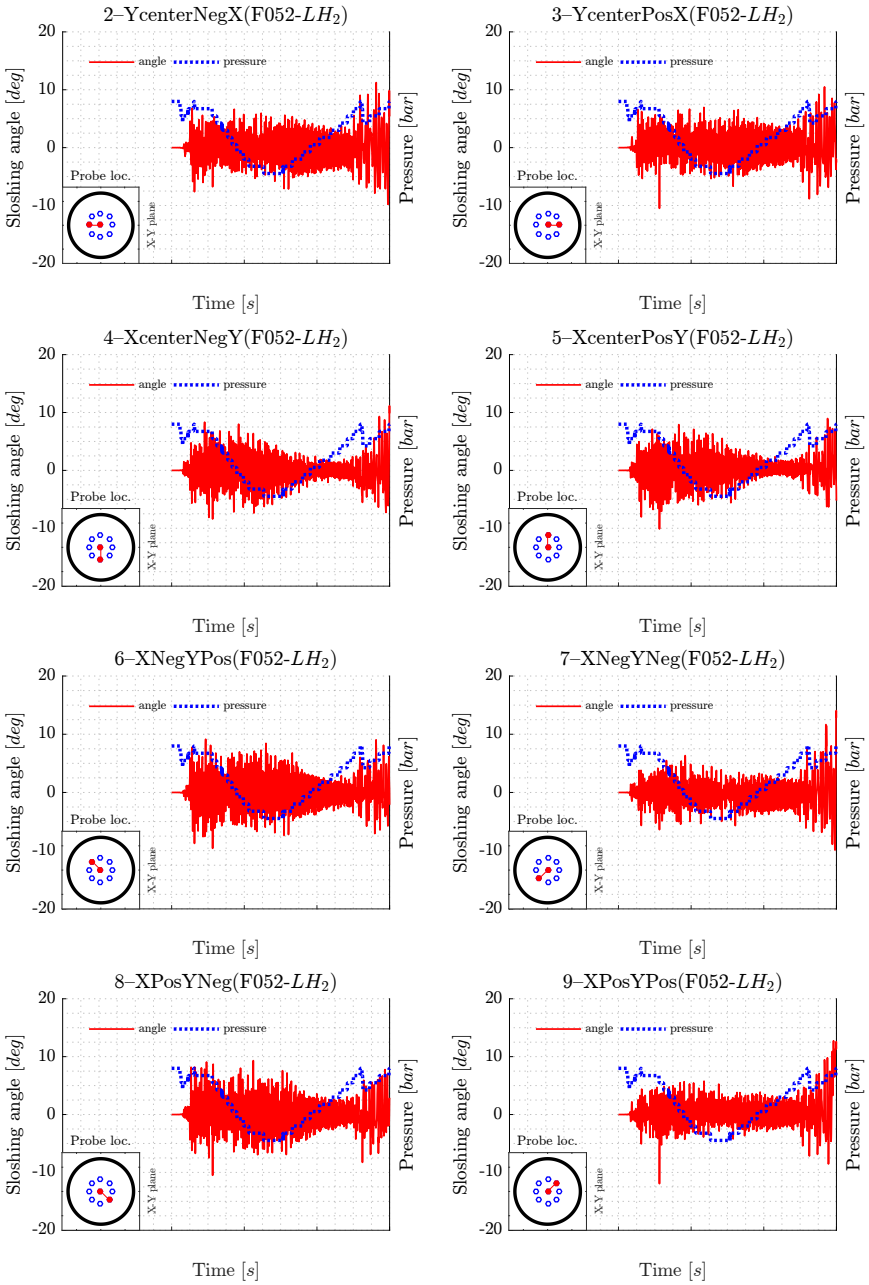

Figure A.0.11: Flight F052 LH_2 sloshing angle (CFD)/pressure evolution vs Time at several tank locations

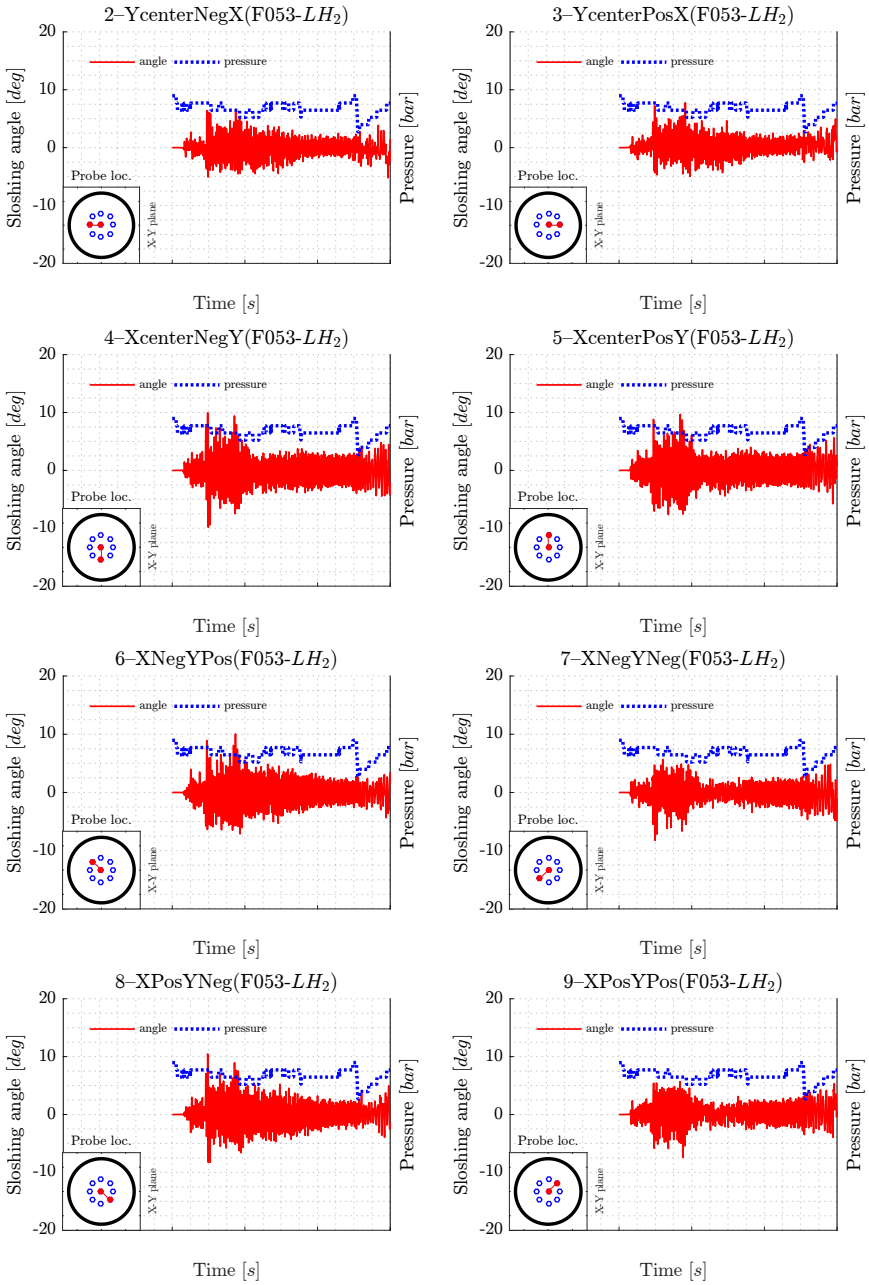

Figure A.0.12: Flight F053 LH_2 sloshing angle (CFD)/pressure evolution vs Time at several tank locations